ISET Journal of Earthquake Technology, Paper No. 569, Vol. 59, No. 1, March 2022, pp. 1–26

ON CONTRIBUTION OF AFTERSHOCKS TO CUMULATIVE SEISMIC DAMAGE IN RC FRAMES

Sandip Das
Department of Civil Engineering, Indian Institute of Technology Guwahati
Guwahati 781039, E mail id: *sandip.das@iitg.ac.in*

Vinay K. Gupta (Corresponding Author)
Department of Civil Engineering, Indian Institute of Technology Kanpur
Kanpur 208016, E mail id: *vinaykg@iitk.ac.in*

ABSTRACT

Aftershocks have the potential to cause collapse of a structure damaged by the preceding main shock and thus the conventional single event-based seismic design may not guarantee the desired safety against earthquake ground motions. A systematic investigation is carried out in this study on the relative contribution of aftershock ground motions to cumulative structural damage in the case of three Indian code-designed reinforced concrete bare frames having different fundamental periods. Assuming that the response spectrum and time-frequency characteristics of the aftershock motions may be related to these characteristics of the main shock motion, a variety of seismic scenarios (in terms of earthquake magnitude, representative distance, focal depth and soil type), and response spectrum and time-frequency characteristics of the anticipated main shock motion are considered, and corresponding main shock and aftershock ground motions are generated. The damage analysis shows that short-period structures are more vulnerable to the aftershock-induced damage compared to the long-period structures, unless the main shock motion has a significant long period component or is associated with relatively shallower aftershocks. Further, the severity of aftershock events (in comparison with that of the main shock event) increases significantly for the longer main shock and shallower aftershock events, and for the high-frequency main shock motions in the case of short-period structures. It is also found that the relative aftershock severity can be estimated in terms of the relative ground motion parameters like the ratios of duration and spectral ordinates for the aftershock to those for the main shock.

KEYWORDS: Damage Index; Aftershock Sequence; Conditional Simulation; Seismic Scenario; Time-History Analysis; RC Frames

INTRODUCTION

The existing earthquake design philosophy does not include any perceptible role of aftershocks, because those are smaller in size than the main shock, and therefore the seismic demands due to even the largest aftershock are not considered to be as critical as those due to the main shock. Aftershocks may however become important because smaller events have the potential to contribute significantly to the cumulative damage of a structure (Das et al. [1]). Sunasaka and Kiremidjian [2] showed for an idealized single-degree-of-freedom (SDOF) system that the cumulative damage from the main shock-aftershock sequences is significantly higher than the damage obtained if only the main shocks are considered. Further, a strong aftershock can cause significant additional energy dissipation and increase in displacement ductility demand, especially for the structures that exhibit deformation softening (Mahin [3]). There have been examples when the structures collapsed during one of the aftershocks even when those had survived the main shock. Of the 11 people killed due to the 1997 Umbria-Marche earthquake, four were in the Basilica of St. Francis in Assisi at the time of the first aftershock, as they had gone to inspect the damage caused by the main shock (Spence and D'Ayala [4]). In another example, one aftershock of 1999 Turkey Kocaeli earthquake killed seven people, injured at least 239 people, and caused several buildings to collapse in three cities near its epicenter (USGS [5]).

As discussed above, aftershocks may be crucial for the safety of a structure, which has already been damaged during the main shock, particularly when the main shock causes significant degradation in the stiffness and/or strength of the structure and the aftershocks are strong enough for the weakened structure to undergo further damage (Jalayer et al. [6]). Since the effects of aftershock motions are not accounted for in the existing design practice, it is important to assess whether a damaged structure is safe at the end of the main shock motion against the threat from the impending aftershocks. Some of the past studies (Amadio et al. [7]; Fragiacomo et al. [8]; Li and Ellingwood [9]; Hatzigeorgiou and Beskos [10]; Hatzigeorgiou and Liolios [11]; Hatzigeorgiou [12–14]; Moustafa and Takewaki [15]) have considered the effects of aftershocks in structural damage or inelastic response. However, in all these cases the aftershock motions were simulated to maximize the structural response considered, and later as shown in a past study (Ruiz-Garcia and Negrete-Manriquez [16]), the artificial sequences that ignore site-specific correlations between the features like frequency content and duration of the main shock and aftershock motions are likely to produce much more inelastic demands than those produced by the recorded main shock-aftershock sequences. Goda and co-workers have therefore considered the artificial main shock-aftershock sequences with the variability of as-recorded main shock-aftershock sequences preserved (Goda and Taylor [17]; Goda [18]), in their study of the effect of aftershocks on the maximum ductility demand of structures having a variety of hysteretic behaviours. Yeo and Cornell [19] proposed a building tagging methodology (indicating whether a building is safe to occupy after the main shock) based on the quantification of the performance of damaged building due to the potential aftershock ground motions (Luco et al. [20]) and time-dependent seismic hazard due to the aftershocks at the site. It is not always practical to repair the damaged structure before the occurrence of the aftershocks, and therefore the yield design levels typically provided in the existing design philosophy may have to be raised to avoid collapses during the aftershocks (Gupta et al. [21]). Hence, it will be useful to know apriori whether additional damage due to the anticipated aftershock motions is likely to be critical, particularly when the design main shock motion is made compatible with a specified design spectrum (Hancock et al. [22]) and the recorded main-shock-aftershock sequences that meet this requirement for a variety of seismological scenarios (characterized by the location and size of earthquake event, representative source-to-site distance, and the local site condition) are not readily available.

It has been clearly established that aftershock motion characteristics are conditional to those of the preceding main shock (Ruiz-García [23]; Das and Gupta [24]; Yingnan et al. [25]; Nithin et al. [26]) and that time-frequency characteristics arising from the pattern of arrivals of different seismic waves, not just spectral representation, of the aftershock motion are critical for the structural response (Goda and Taylor [17]; Goda [18]). Despite this, it is common to consider either spectrally matched aftershocks or randomized/back-to-back sequencing techniques ignoring such conditionality between the main shock and aftershock motions, whenever the recorded sequences are not adequate (Zhai et al. [27]; Song et al. [28]; Tesfamariam et al. [29]; Jalayer and Ebrahimian [30]; Shin and Kim [31]; Rinaldin et al. [32]; Omranian et al. [33]; Wen et al. [34]; Shokrabadi et al. [35]; Trapani and Malavisi [36]; Shafaei and Naderpour [37]; Wen et al. [38]; Iervolino et al. [39]). This has made it possible to carry out methodologically novel studies for damage or vulnerability assessment under sequence-type motions without focusing on the sequence formation technique. However, this has resulted in the situation that no study till date shows how the preceding main shock and its time-frequency characteristics can possibly affect the response/damage due to the aftershocks for a given seismological scenario via a controlled variation of seismological disparities between the main shock and aftershock. This gap in the literature needs to be filled. This can be done conveniently with the help of conditionally simulated aftershock motions along with the acceptable structural models and global damage measure. Such a study will be able to quantify the effects of an aftershock on cumulative structural damage and thus provide useful insights into the severity of the aftershock (or lack of it) vis-à-vis the main shock motion under various combinations of seismological scenarios for the main shock and aftershock. It may also be mentioned that while it is possible to consider the most suitable sequence of main shock and aftershock ground motion records for any specific need (Qiao et al. [40]; Abdelnaby [41]), any ground motion or response parameter for such a sequence will most likely not conform to its expected value for the seismic scenarios of the main shock and aftershock events of those records. This is so because any ground motion record is a random sample of the underlying random process, and a set of seismological parameters, like magnitude, distance, and site condition, can be associated with several such underlying processes. Even when several recorded sequences are used, those would likely correspond to different combinations of main shock and aftershock seismic scenarios, and thus the so-obtained variation in the chosen ground motion or response parameter will not truly reflect the uncertainty associated with a given combination of main shock and aftershock seismic scenarios.

There have been some developments in the direction of simulating aftershock accelerograms for a given seismic scenario. Das and Gupta [42] proposed a wavelet-based method to simulate a spectrum-compatible aftershock motion when the response spectrum of the anticipated main shock motion and a seed accelerogram having the desired time-frequency characteristics of the anticipated main shock motion, are available along with the pseudo spectral acceleration (PSA) spectrum and strong-motion duration (SMD) (as defined in Trifunac and Brady [43]) of the anticipated aftershock motion. Das and Gupta [24] proposed conditional scaling models to obtain pseudo spectral velocity (PSV) spectrum and SMD of the anticipated aftershock motion if these two functionals for the main shock motion are known along with the seismological and site parameters for both main shock and aftershock motions. Papadopoulos et al. [44, 45] recently proposed the selection of a main shock-aftershock sequence based on the correlation of spectral residues, where the underlying assumptions are consistent with the philosophy of the conditional scaling model. Hu et al. [46] devised a methodology for the simulation of aftershock motions from the observed seismicity, the main shock magnitude and fault mechanism, relative location of the site to the main shock epicentre, and the local site condition. However, the simulated aftershock motions are not governed by the features of the main shock motion. Hence, this method may not be useful, when a recorded or anticipated main shock motion is to be considered to generate the corresponding aftershock motions. Aftershock motions are simulated in this study by using the methodologies suggested by Das and Gupta [24, 42], such that those are consistent with the anticipated main shock motions for a variety of hypothetical seismic scenarios and time-frequency characteristics of the main shock motion. Those are then used for a systematic investigation of the additional damage due to aftershocks in an already damaged reinforced concrete structure (due to the preceding main shock) and to identify situations in the framework of damage-based seismic design where the additional damage due to aftershocks cannot be ignored.

GENERATING MAIN SHOCK-AFTERSHOCK SEQUENCES

We consider the generation of aftershock ground motions corresponding to the given main shock ground motion at a site by using the methodology of Das and Gupta [42], wherein the temporal features of the main shock ground motion are used to generate the aftershock ground motions at the same site. This methodology has been shown to give realistic aftershock motions with similar damage-causing ability as the recorded aftershock motions, provided reliable estimates of PSA and SMD are available for such motions (Das and Gupta [42]). Figure 1 shows the flowcharts describing this methodology. While the part (a) gives the flowchart in terms of the conceptual steps of this methodology, the part (b) gives the flowchart in terms of the details of those steps. While the main shock motion needs to be generated for a given seismic scenario, we consider here five recorded accelerograms having different durations and time-frequency characteristics (due to different patterns of wave arrivals), and also having different shapes of response spectra, for generating various choices of the main shock ground motion. These seed accelerograms are (i) S00E component recorded at El Centro site, Imperial Valley Irrigation District during the 1940 Imperial Valley earthquake, (ii) N21E component recorded at Taft Lincoln School Tunnel, California during the 1952 Kern County earthquake, (iii) N05W component recorded at Array No. 5, Cholame, Shandon, California during the 1966 Parkfield earthquake, (iv) N90E component recorded at Utilities Building, 215 West Broadway, Long Beach, California during the 1971 San Fernando earthquake, and (v) S04E component recorded at Engineering Building, Santa Ana, Orange County, California during the 1968 Borrego Mountain earthquake. Figure 2 shows the 5% damping PSA spectra of these accelerograms in the units of g . These accelerograms are used to generate two sets of five main shock motions each: (a) the set in which all the five main shock motions have identical response spectrum but different durations and temporal features, and (b) the set in which all the five main shock motions have identical duration and temporal features but different response spectra. The synthetic motion with the Borrego Mountain record as seed accelerogram and compatible with the San Fernando motion spectrum is common in the two sets. The first set will be used to study the effects of temporal characteristics of the main shock motion on the severity of aftershocks, while the second set will be used to study the effects of energy distribution in the main shock motion. A set of compatible motions is chosen because it is difficult to find the recorded motions having the prescribed strong-motion duration as well as the prescribed frequency content. It may be mentioned that such motions may sometimes suffer from a low-period mismatch (with respect to the target spectrum), despite having realistic time-frequency characteristics, as discussed by Mukhopadhyay et al. [47]. However, this mismatch may not significantly affect the response of structures.

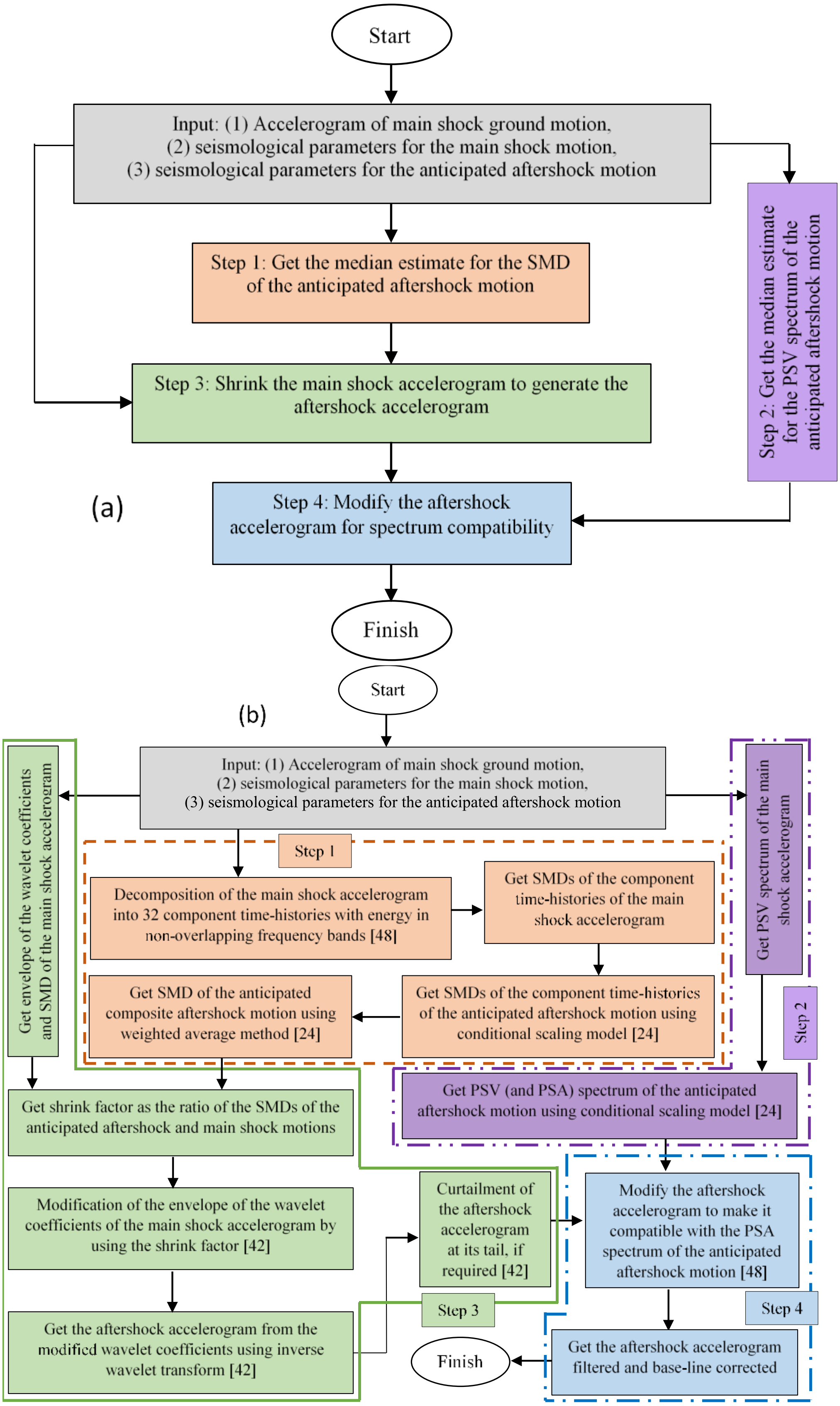

Fig. 1 Flowcharts for the generation of main shock-consistent aftershock motion in terms of (a) conceptual steps and (b) details of conceptual steps

The first set of main shock motions is generated by making the seed accelerograms corresponding to the Imperial Valley, Kern County, Parkfield and Borrego Mountain motions compatible with the 5% damping PSA spectrum of the San Fernando motion as in Mukherjee and Gupta [48]. The modified motions, together with the (recorded) San Fernando motion, are shown in Figure 3 and the 5% damping PSA spectra of these motions are shown in Figure 4. The PSA spectrum for the San Fernando motion is chosen because it has the widest peak region amongst all five response spectra and this will help in exciting a wider range of fundamental modes of different structural systems.

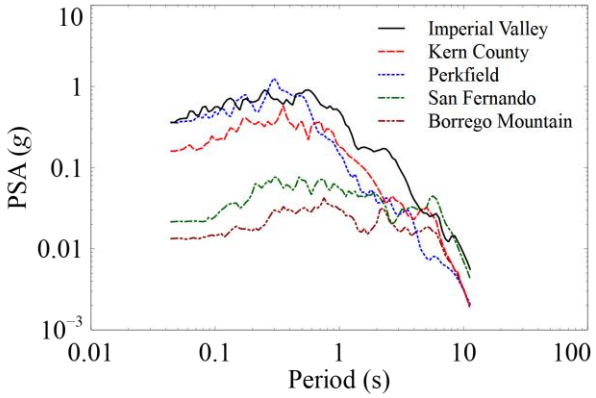

Fig. 2 5% Damping PSA spectra for different seed accelerograms

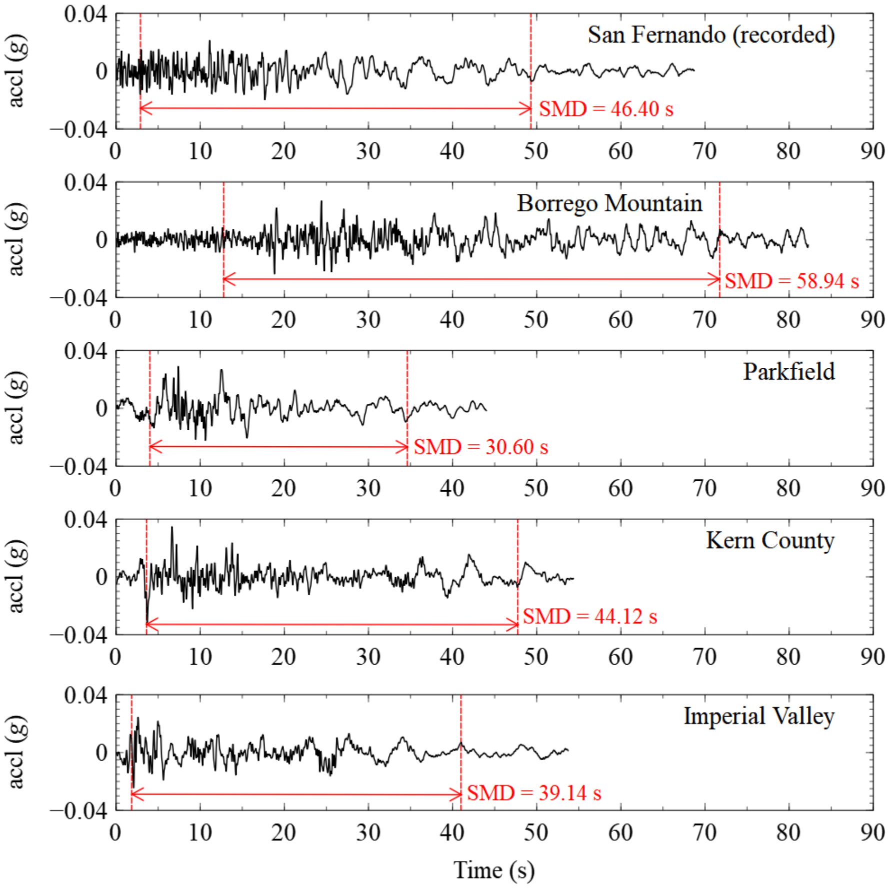

Fig. 3 Recorded San Fernando motion, and synthetic motions compatible with the 5% damping PSA spectrum of this motion in the cases of Borrego Mountain, Parkfield, Kern County, and Imperial Valley motions as seed accelerograms

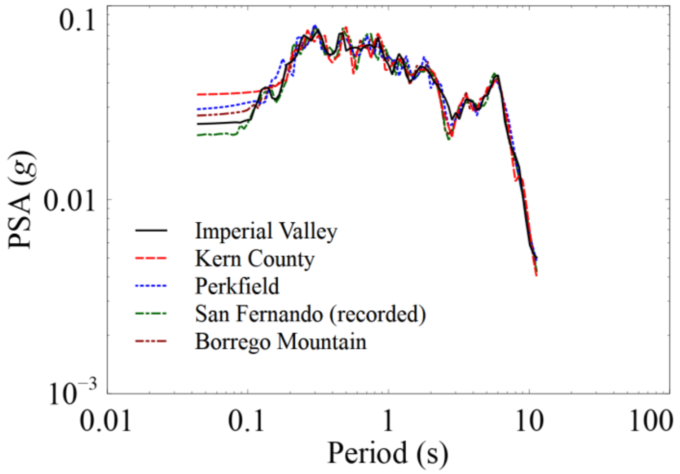

Fig. 4 5% damping PSA spectra of recorded San Fernando motion and synthetic motions compatible with the 5% damping PSA spectrum of this motion for different seed accelerograms

The second set of main shock motions is generated by modifying the Borrego Mountain motion to match the 5% damping PSA spectra of the Imperial Valley, Kern County, Parkfield and San Fernando motions (Mukherjee and Gupta [48]). The recorded Borrego Mountain motion and the modified motions are shown in Figure 5 and the 5% damping PSA spectra of these motions are shown in Figure 6.

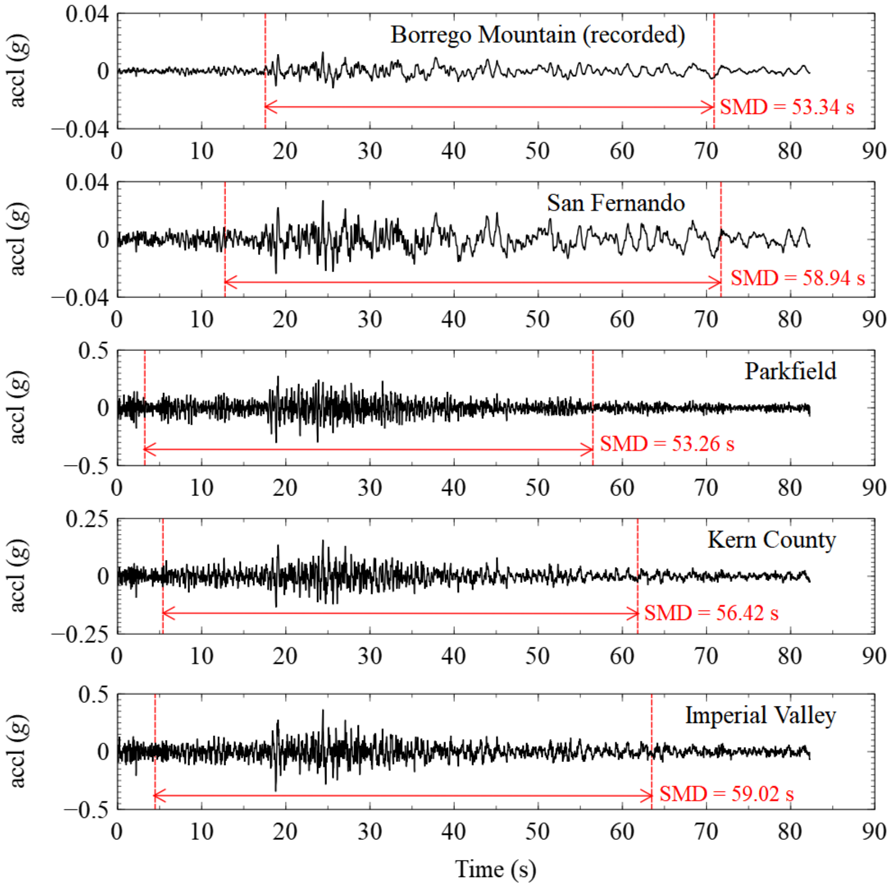

Fig. 5 Recorded Borrego Mountain motion, and synthetic motions with this motion modified to be compatible with the 5% damping PSA spectra of San Fernando, Parkfield, Kern County, and Imperial Valley motions

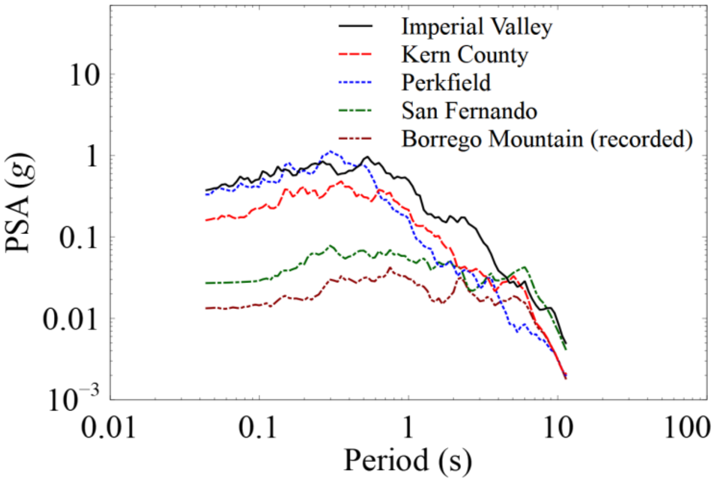

Fig. 6 5% damping PSA spectra of recorded Borrego Mountain motion and synthetic motions for this motion modified to be compatible with the 5% damping PSA spectra of different recorded motions

In order to generate an aftershock motion consistent with a main shock motion (Das and Gupta [42]), the conditional scaling models for PSV spectrum and SMD are used to estimate the expected PSA spectrum and SMD for the aftershock motion (Das and Gupta [24]). For this purpose, it is assumed that the local and moment magnitudes of the main event are 6.1 and 6.2, respectively, and that the local and moment magnitudes of the aftershock are 5.8 (with the magnitude difference ΔM = 0.3 between the main shock and the aftershock). This scenario of main shock and aftershock magnitudes is adopted from the 2004 Firouzabad-Kojour earthquake (BHRC [49]) arbitrarily. Further, it is assumed that the closest distance R_{rup} from the site to the fault rupture is 15 km, focal depth difference Δh between the main shock and the aftershock is zero, and that the site has soft soil conditions (i.e., s = 0). Aftershock ground motions are simulated for all nine different main shock motions shown in Figures 3 and 5 for the scenario mentioned above. The 5% damping PSA spectra of the simulated aftershock motions corresponding to the main shock motions in these figures are shown in Figures 7 and 8 respectively.

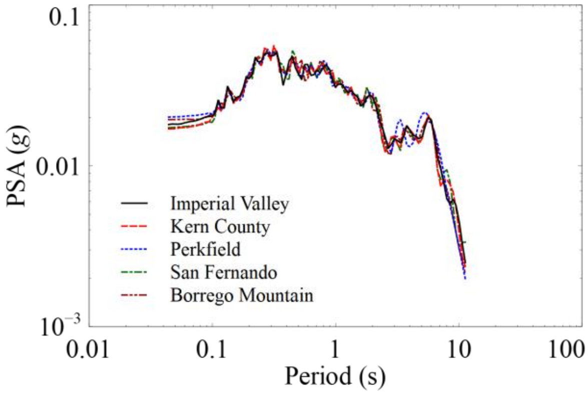

Fig. 7 5% damping PSA spectra of aftershock accelerograms corresponding to the main shock motions in Figure 3

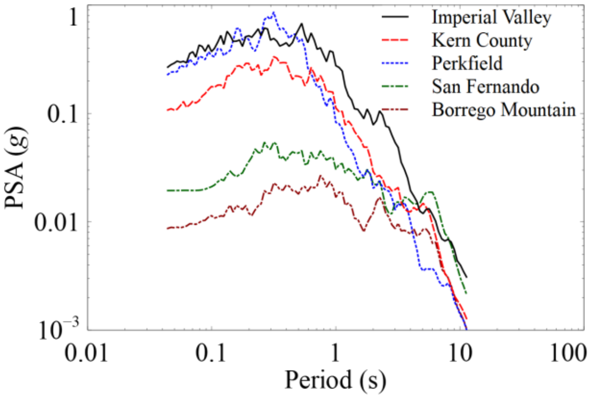

Fig. 8 5% damping PSA spectra of aftershock accelerograms corresponding to the main shock motions in Figure 5

Whereas the spectra shown in Figure 7 correspond to the aftershock accelerograms to be used to study the effects of temporal characteristics of the main shock on the damage causing potential of aftershocks, those shown in Figure 8 correspond to the aftershock accelerograms to be used to study the effects of energy distribution in the main shock. It may be noted that only one aftershock motion is considered here for each of the nine main shock-aftershock sequences. This is done in order to emphasize the relative contribution of each aftershock motion to the cumulative damage.

A second set of 40 aftershock motions is also simulated to create an additional 31 sequences of main shocks and aftershocks. These aftershock motions are simulated for different seismic scenarios, and their details are provided at the appropriate places in the following sections. Thus, a total of 40 sequences are simulated to systematically investigate the aftershock-induced additional damage vis-à-vis seismological scenarios and time-frequency characteristics of the main shock motions. It should be mentioned here that the strength of any main shock motion is not relevant for its selection and subsequent aftershock motion generation because a uniform scaling of the sequence to achieve the required strength will not affect either its time-frequency characteristics or the interdependence between the main shock and its aftershocks.

NUMERICAL MODELLING OF FRAMES AND ANALYSIS

1. Modelling

Three 1-storey, 2-storey and 5-storey reinforced (RC) bare frames (designated as Frame-1, Frame-2 and Frame-3, respectively), each having three bays, have been designed following the provisions of IS 456 (BIS [50]), IS 1893 (BIS [51]) and IS 13920 (BIS [52]). The RC frames along with the section details of various members are shown in Figures 9 to 11. The frames are modelled in the software OpenSees (Open System for Earthquake Engineering Simulation, version 2.4.5) (Mazzoni et al. [53]) for performing dynamic analyses. It is assumed that concrete of the characteristic cube strength of 25 MPa and reinforcement steel of the grade 500 MPa are used in the frame. In order to obtain realistic moment-curvature relationships, the concrete is modelled separately as ‘confined concrete’ inside the core and as ‘unconfined concrete’ for the cover concrete via the material model Concrete07 available in OpenSees (Mazzoni et al. [53]). For steel, the material model ReinforcingSteel is used. Further, the hysteresis behaviour of a RC section is inherently governed by the pre-defined material-level hysteresis properties. As the formation of plastic hinges takes place near the ends of flexural members, the columns and beam are modelled by using the beamWithHinges element available in OpenSees (Mazzoni et al. [53]; Scott and Fenves [54]). The beamWithHinges element effectively localizes the plastic hinging at the element ends, while it accounts for the distributed plasticity over the plastic hinge length l_p (Scott and Fenves [54]). Here, l_p is calculated by using the following equation for reinforced concrete members (Paulay and Priestley [55])

$$l_p = 0.08L + 0.022 f_y d_b \tag{1}$$

where, l_p is in meters, L is the shear-span of the member in meters, f_y is the yield strength of reinforcement steel in MPa, and d_b is the diameter of the longitudinal reinforcement in meters. Based on the structural properties and the mass from gravity loads (including floor and wall), the fundamental periods of Frame-1, Frame-2 and Frame-3 are obtained as 0.391, 0.565 and 1.246 s, respectively. The moment-rotation relationships for different plastic-hinge locations of Frame-1, Frame-2 and Frame-3 are tabulated respectively in Tables 1–3. The ultimate rotations are obtained from the ultimate curvatures and the associated plastic hinge lengths, where the ultimate curvature corresponds to the rupture of tensile steel or crushing of concrete (whichever happens earlier). It may be mentioned here that the frames satisfy the capacity-based design, where only the ductile failure of flexural members takes place through plastic hinges. Such frames, in general, do not satisfy the more stringent requirement of strong column and weak beam (SCWB) collapse mechanism as recommended by the latest IS 13920 (BIS [56]) and other standards (NZS [57]; BSI [58]; ACI [59]). Further, most of the existing RC buildings in India (and possibly in other countries) do not conform to the SCWB philosophy. Hence, only the capacity-based design of frames is considered in the present study, which obviates the formation of a shear hinge in the flexural members. This approach may also help in highlighting those cases when the noncompliance of SCWB philosophy becomes critical in the context of additional damage due to aftershocks.

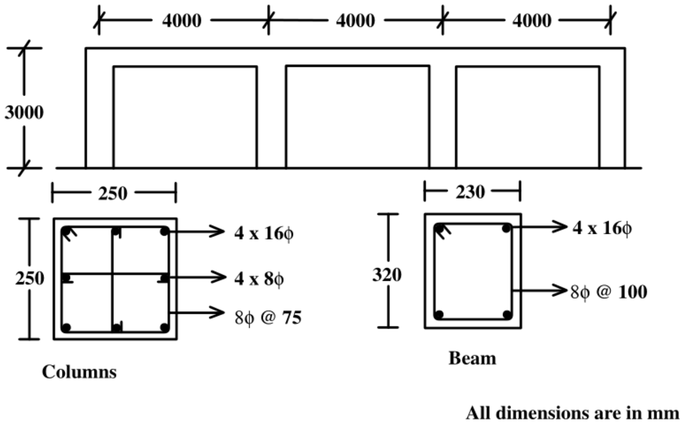

Fig. 9 Geometric and sectional details for Frame-1

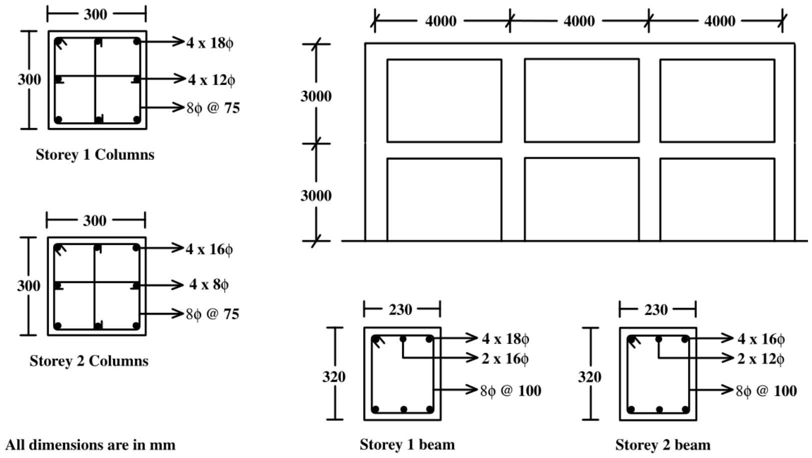

Fig. 10 Geometric and sectional details for Frame-2

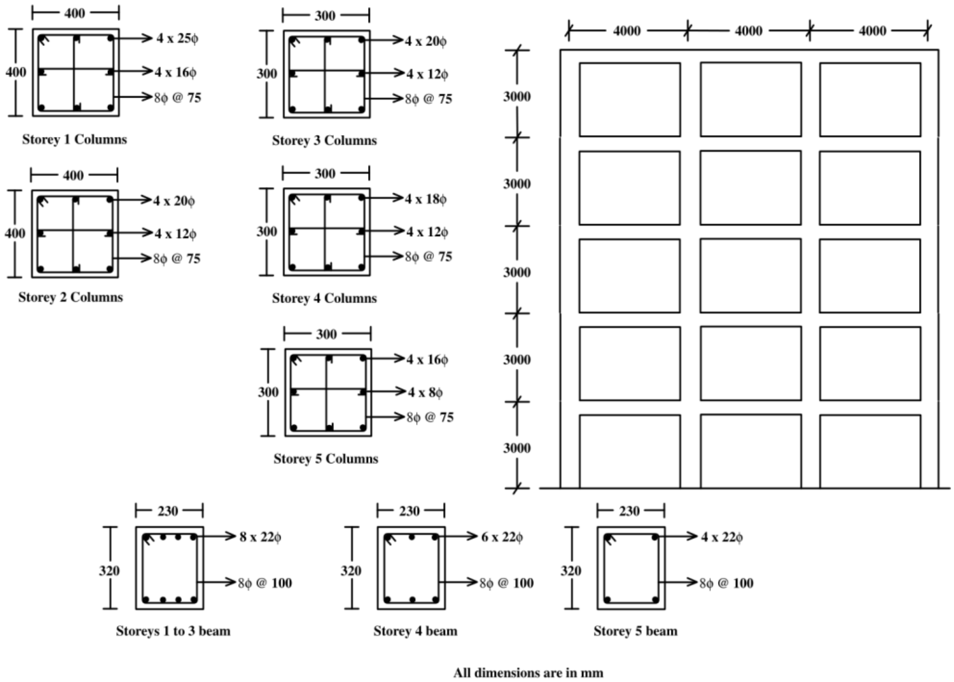

Fig. 11 Geometric and sectional details for Frame-3

Table 1: Moment-rotation relationships of plastic hinges at different locations in Frame-1

Location	Yield Moment (kN.m)	Yield Rotation (rad)	Ultimate Rotation (rad)	Moment Capacity (kN.m)
Beam	46.8	0.0043	0.1718	53.6
Exterior Column	44.2	0.0066	0.2663	48.4
Interior Column	47.5	0.0069	0.2494	51.4

Table 2: Moment-rotation relationships of plastic hinges at different locations in Frame-2

Location	Yield Moment (kN.m)	Yield Rotation (rad)	Ultimate Rotation (rad)	Moment Capacity (kN.m)
1-Storey Beam	79.1	0.0048	0.1796	91.1
2-Storey Beam	59.1	0.0041	0.1608	67.7
1-Storey Exterior Column	89.0	0.0053	0.1067	99.5
1-Storey Interior Column	96.5	0.0056	0.0983	107.2
2-Storey Exterior Column	58.7	0.0046	0.1875	65.2
2-Storey Interior Column	63.3	0.0048	0.2055	69.7

Table 3: Moment-rotation relationships of plastic hinges at different locations in Frame-3

Location	Yield Moment (kN.m)	Yield Rotation (rad)	Ultimate Rotation (rad)	Moment Capacity (kN.m)
1,2 & 3-Storey Beams	159.9	0.0065	0.2130	187.5
4-Storey Beam	121.7	0.0062	0.2126	141.5
5-Storey Beam	83.2	0.0057	0.2120	95.6
1-Storey Exterior Column	262.5	0.0049	0.0627	297.3
1-Storey Interior Column	286.3	0.0053	0.0583	314.8
2-Storey Exterior Column	189.6	0.0038	0.0577	210.6
2-Storey Interior Column	210.6	0.0040	0.0532	232.3
3-Storey Exterior Column	110.1	0.0062	0.0978	121.9
3-Storey Interior Column	119.9	0.0068	0.0929	129.1
4-Storey Exterior Column	89.1	0.0053	0.1064	99.6
4-Storey Interior Column	96.4	0.0056	0.0985	107.1
5-Storey Exterior Column	58.8	0.0040	0.1597	65.3
5-Storey Interior Column	63.2	0.0041	0.1807	69.6

2. Analysis

Each example frame is first analyzed for the self-weight and superimposed load by using OpenSees (Mazzoni et al. [53]). Then, with the deformed shape taken as the initial displaced shape, nonlinear time-history analysis is carried out for the base motion by direct time-integration technique available in OpenSees (Mazzoni et al. [53]). For this purpose, Rayleigh damping is considered corresponding to 5% of the critical damping of the first two eigenmodes. Both geometric and material nonlinearities are considered in the analysis, where the material nonlinearity is assumed to be accounted for only through the plastic hinges located near the beam and column ends. Thus, the overall structural damage state is governed by the individual damage sates of various plastic hinges. The individual damage state of the i th plastic hinge is quantified via the modified Park and Ang damage index as (Elenas [60])

$$DI_i = \frac{\theta_{m,i} - \theta_{y,i}}{\theta_{u,i} - \theta_{y,i}} + \beta \frac{EH_i}{M_{y,i}\theta_{u,i}} \tag{2}$$

where $\theta_{m,i}$ is the maximum rotation, $\theta_{y,i}$ is the yield rotation, EH_i is the total hysteretic energy dissipated during the load history, $M_{y,i}$ is the yield moment, and $\theta_{u,i}$ is the ultimate rotation capacity of the section. Further, β is a constant, which represents the effect of cyclic loading on structural damage. In the present study β is assumed to be 0.15, which is reasonable for reinforced concrete structures with ductile detailing (Cosenza et al. [61]). From the individual damage indices of all plastic hinges the overall damage index (ODI) is obtained as (Elenas [60])

$$ODI = \frac{\sum_{i=1}^{n} DI_i\, EH_i}{\sum_{i=1}^{n} EH_i} \tag{3}$$

where n is the total number of plastic hinge locations. ODI is an indicator of the damage state of the structure, where $ODI = 0$ means 'no damage' and $ODI \geq 1$ implies 'complete collapse' of the structure. The Park and Ang type damage index is chosen because this is a widely accepted damage index to account for low-cycle damage (van de Lindt and Goh [62]). Also, this is applicable for quantifying damage from the energy dissipation through several smaller inelastic loading cycles, as observed in the case of structural response to aftershock ground motions (Wen et al. [38]).

NUMERICAL RESULTS AND DISCUSSION

To estimate the additional damage due to an aftershock motion, the structure under consideration is assumed to be subjected to the sequence of main shock and aftershock motions, with sufficiently long gap (of silence or no excitation) introduced in between the two motions of the sequence in order for the free-vibration to completely decay. The ODI at the end of the main shock motion, called as initial ODI, is then compared with the ODI at the end of the aftershock motion, called as final ODI. Greater is the relative increase from initial ODI to the final ODI, more severe will be the effect of aftershock motion. Both main shock and aftershock motions are scaled by the same factor, so that the initial ODI becomes equal to a predetermined value. This value corresponds to the damage state expected to be achieved after the main shock motion in conventional design. For most structures, this value will be equal to 1.0, corresponding to 'complete collapse' (Williams and Sexsmith [63]). It may be mentioned that the main shock and aftershock motions are suitably scaled in this study to get the specified initial ODI in predesigned frames, in preference over designing the frames for the target initial ODI under the unscaled main shock and aftershock motions. This is done for simplicity, as designing a frame to match both initial ODI and fundamental period would be much more complicated than scaling of the ground motions for a predesigned frame with a fixed fundamental period.

Figure 12 shows the variations of the final ODI value with the fundamental period of the example frames for the five main shock motions of Figure 3 (and Figure 4) and the corresponding aftershock motions (see Figure 8), with the initial ODI taken as 0.6 (corresponding to 'severe' damage). Since all the main shock motions considered for these results are compatible with the same PSA spectrum (of the San Fernando motion), it is clear that for a frame, the Borrego Mountain motion having the maximum SMD (see Figure 3) causes the maximum aftershock damage, while the Parkfield motion with the minimum SMD causes the least aftershock damage. This is because for the longer motions, the contribution of the second term in Equation (2) is comparatively more, and an aftershock motion usually contributes to the additional damage only through the second term. Further, it may be observed in Figure 7 that the aftershock spectra are reasonably broad-banded, with the largest spectral ordinates in the 0.2–1 s period range, and that the fundamental periods of Frame-1 and Frame-2 fall in this range. However, the central frequencies of the main shock motions are well tuned with the fundamental frequency of Frame-2 alone. This results in an increase in the initial ODI, and thus the scaling factor for the main shock motion has to be reduced to keep the initial ODI unchanged at 0.6 (in comparison with Frame-1). This leads to a smaller contribution of the first term in Equation (2) (due to a smaller largest peak rotation at any plastic hinge) and thus to a higher contribution of the second term corresponding to a greater number of large response peaks. Since the aftershock motion is consistent with the main shock motion, hysteretic energy dissipation contributes more to the aftershock damage also, which results in a higher additional damage (beyond the initial ODI) in Frame-2 as compared to Frame-1. There is higher additional damage in Frame-2 also because the response of Frame-2 includes some contribution of the higher modes. It may be further noted that the main shock motions considered in Figure 12 are all broad-band motions and are thus capable to excite both first and second modes of Frame-3. Hence, plastic hinges are formed in the columns between the 2nd and 3rd floors of this frame due to larger curvatures (and the absence of SCWB philosophy), and higher inter-storey drifts are caused between these floors. There is greater damage in the frame during the consistent aftershocks due to this damaged part, especially in the case of the San Fernando main shock motion, as there is some increase even in the first term of Equation (2). On the other hand, the number of response cycles in Frame-3 is less (due to a longer fundamental period), thus resulting in a smaller contribution of the second term in Equation (2). Consequently, the additional contribution of the higher modes to the final *ODI* of Frame-3 gets compensated by this reduction in damage, and a saturation is observed in the increase or decrease of the *ODI* of this frame with respect to Frame-2. Further, a relatively higher final *ODI* for the San Fernando motion case (for Frame-3) emphasizes the need of SCWB philosophy in order to limit the aftershock-induced additional damage within the desired level in the flexible structures under the broad-band motions.

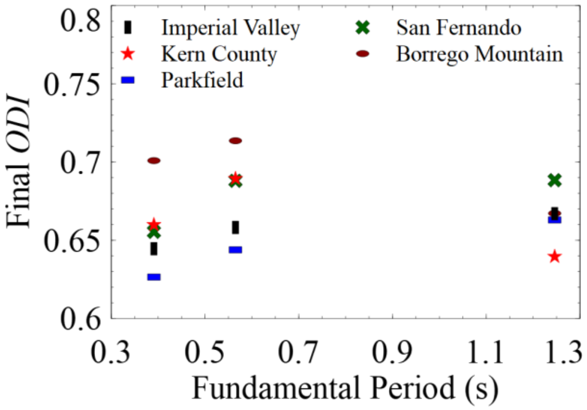

Fig. 12 Variations of final *ODI* with frame period for motions of different time-frequency characteristics (and same PSA spectrum as for the San Fernando motion) in the case of initial *ODI* = 0.6

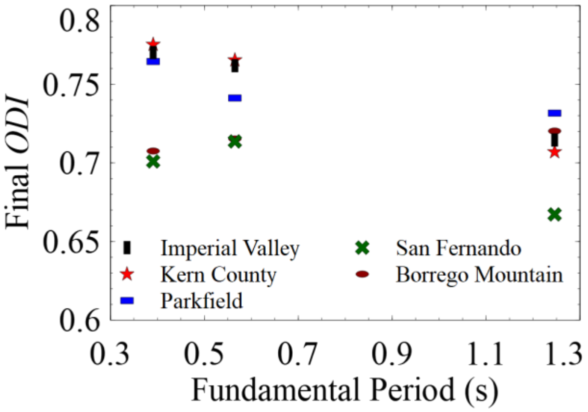

Fig. 13 Variations of final *ODI* with frame period for motions with different PSA spectra (and same time-frequency characteristics as for the Borrego Mountain motion) in the case of initial *ODI* = 0.6

It is further interesting to see how, depending on the energy distribution in the main shock motion, the severity of aftershock motion changes. For this the parent (main shock) motions as shown in Figure 5 (and Figure 6) are considered after scaling for the initial *ODI* of 0.6, and variations in the final *ODI* value with the fundamental periods of the example frames are shown in Figure 13. It is apparent from the figure that for the three motions, viz., Imperial Valley, Kern County and Parkfield, which are dominated by short- to intermediate-period waves, Frame-1 and Frame-2 have more severity of aftershocks than they have for the broad-band motions. This is because the number of hysteresis cycles are expected to be more for a structure of shorter fundamental period and subjected to a motion dominated by the short-period waves, which results in a higher contribution from the second term in Equation (2). It is also clear from the figure that the severity of aftershocks is reduced for Frame-3 (compared to that for Frame-2) under any aftershock motion that has relatively little energy at the longer periods, like Imperial Valley, Parkfield, and Kern County motions (see Figure 8). There is a smaller reduction, however, in the aftershock severity for the Parkfield motion due to the additional contribution of higher modes to the final *ODI*. For the broad-banded motions like the Borrego Mountain and San Fernando motions, the severity of aftershocks may increase (as for the Borrego motion), decrease (as for the San Fernando motion), or remain unchanged, depending on the relative contributions of the higher modes and number of response cycles to the additional damage, as discussed already in the case of Figure 12. It may be added here based on the results in Figures 12 and 13 that the first term in Equation (2) is generally not increased during an aftershock motion, as also reported by a recent study (Zhai et al. [64]). Even when the dominant period of the aftershock motion is longer than the fundamental period of the structure, the softening of the structure due to stiffness degradation mostly affects the second term.

The results shown in Figures 12 and 13 are for the initial *ODI* of 0.6. It will be useful to see how the severity of the aftershock motion would change for the initial *ODI* s of 0.4 and 0.8. The *ODI* values of 0.4, 0.6 and 0.8 can be reasonably considered as 'threshold of irreparable', 'severe' and 'very severe' (near collapse), respectively. Figure 14 shows the variations in the final *ODI* with the initial *ODI* for the three example frames, when these frames are subjected to the pairs of main shock and aftershock motions corresponding to the 'Parkfield Spectrum' motion shown in Figure 5 (with the aftershock spectrum as shown in Figure 8).

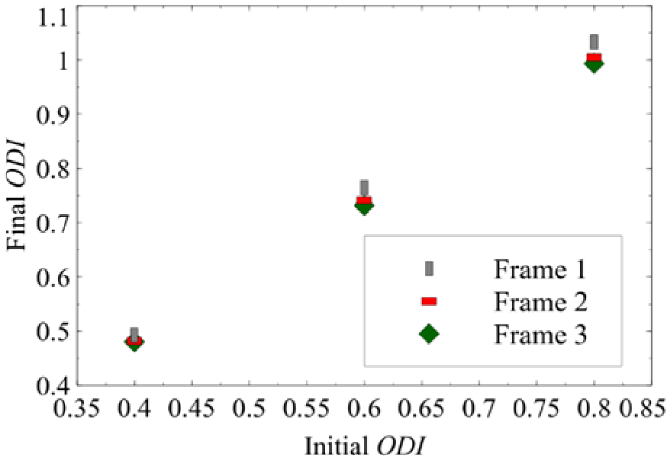

Fig. 14 Increasing trend of final ODI with initial ODI for different frames

It is clear from Figure 14 that for all the frames, the aftershock severity varies almost linearly with the initial ODI within the range of 0.4 to 0.8. This observation of linear trend is found to be true for the other parent main shock motions as well, except when the motion has significant long-period energy. In that case, Frame-3 is associated with a higher rate of increase (than a constant value) in total damage with the initial ODI. This happens because a higher initial damage causes a softening of the structure, and therefore an aftershock motion with a significant long-period energy content gets better tuned with the (increased) period of the structure.

The above results pertained to the seismic scenario of $\Delta M = 0.3$, $R_{\text{rup}} = 15$ km, $\Delta h = 0$, and $s = 0$ for the aftershock motion. Let us now consider possible variations in this hypothetical scenario exclusively for two cases of main shock motions, with the initial ODI taken as 0.6: (a) MS1 motion shown in Figure 5 corresponding to the Borrego Mountain motion as seed motion and Parkfield motion spectrum as the target spectrum, and (b) MS2 motion shown in Figure 3 corresponding to the Parkfield motion as seed motion and San Fernando motion spectrum as the target spectrum. Whereas the MS1 motion is a long-duration, short-period motion, the MS2 motion is a short-duration, broad-band motion. These two motions are expected to provide sufficient insight into the additional aftershock-induced damage vis-à-vis variations in the aftershock scenario (in respect of ΔM, R_{rup}, Δh, and s). Various ground motion characteristics, i.e., PGA, PSA spectrum ordinates at five different periods, and SMD, of the simulated aftershocks motions used in this numerical exercise relative to the same characteristics of the preceding MS1 and MS2 main shock motions are given in Table 4. These relative characteristics will be used to explore their role in the additional aftershock-induced damage.

Figure 15 shows variations in the final ODI with the magnitude difference ΔM for the three example frames, with the main shock magnitude (both local and moment) taken as 7, and $R_{\text{rup}} = 15$ km, $\Delta h = 0$, and $s = 0$ as before. It is clear from the figure that with increasing magnitude difference the final ODI gradually converges to the initial ODI. This confirms that only the larger aftershocks should be considered critical for the additional aftershock damage. In practice the smaller aftershocks having $\Delta M > 0.8$ may be safely ignored for any additional damage. Further, the smaller additional damage seen in Figure 15 for Frame-1 under the MS2 motion indicates that short-period structures are likely to exhibit more damage for the MS1-type main shock motions than for the (broad-band, short-duration) MS2-type main shock motions.

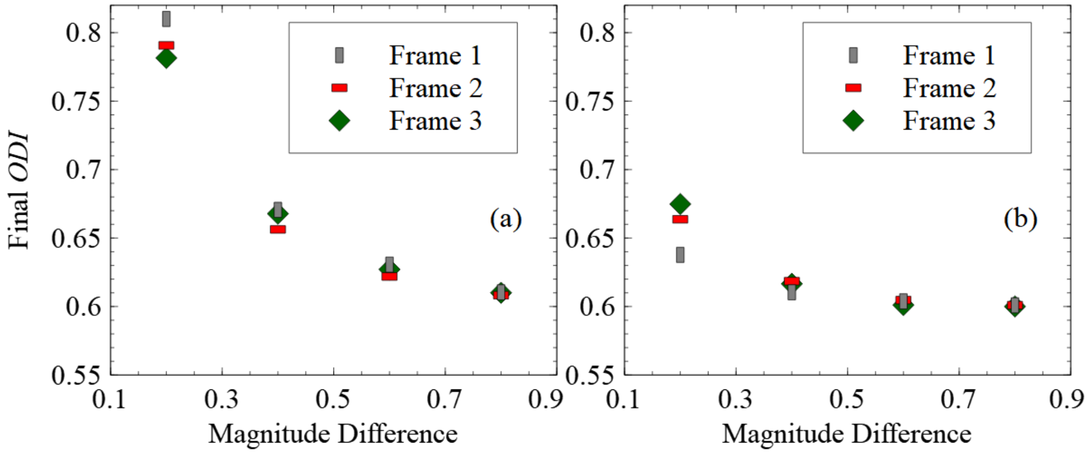

Fig. 15 Variations of final *ODI* with magnitude difference ΔM for different frames, in the case of initial *ODI* = 0.6 with (a) MS1 as the main shock motion, (b) MS2 as the main shock motion

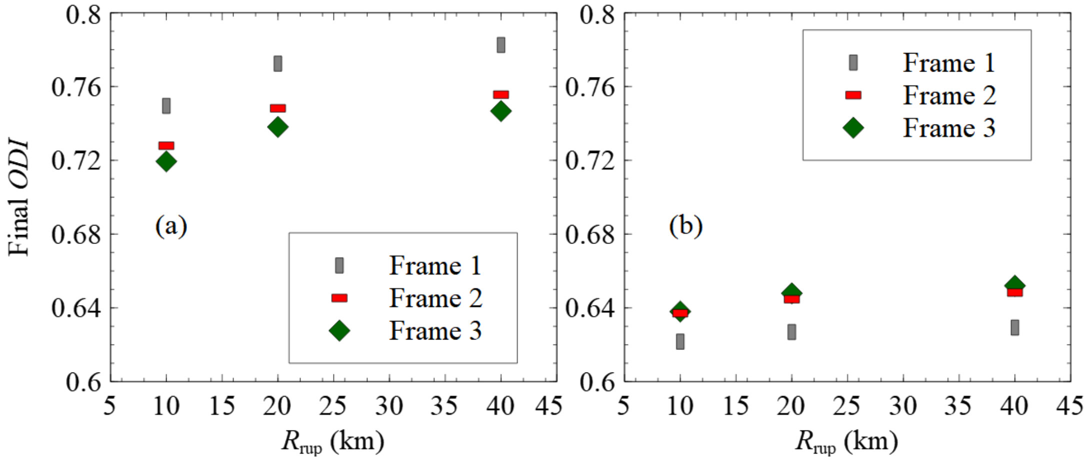

Fig. 16 Variations of final *ODI* with R_{rup} for different frames, in the case of initial *ODI* = 0.6 with (a) MS1 as the main shock motion, (b) MS2 as the main shock motion

Figure 16 shows the variations in final *ODI* with the closest distance to the fault rupture, R_{rup}, for the three example frames, with $\Delta M = 0.3$, $\Delta h = 0$ and $s = 0$ (as considered for Figures 12–14). Since the initial *ODI* is maintained at 0.6 for these results, the main shock motion remains unchanged for different values of R_{rup}. It is clear from the figure that the change in final *ODI* with R_{rup} is insignificant, irrespective of the type of main shock, with final *ODI* undergoing a maximum change of 0.033 for 30 km variation in R_{rup}, in the case of MS1. This is because the conditional model used for the aftershock response spectrum (Das and Gupta [24]) depends on the ratio of the representative distance for the main shock motion to the representative distance for the aftershock motion, where the representative distance is defined in terms of R_{rup} and near-source saturation term D_{sat} (which is governed by the moment magnitude of the event) (Das and Gupta [24]). With the same value of R_{rup} considered for the main shock and aftershock motions in the conditional model (Das and Gupta [24]), the representative distances of a site for the main shock and aftershock motions differ only due to the difference in the D_{sat} values of the two events. Since the representative distance is dominated by the D_{sat} value for the small values of R_{rup} and by R_{rup} for the large values of R_{rup}, the ratio of representative distances decreases asymptotically to unity with an increase in R_{rup}. This leads to an increased strength of the aftershock motion relative to that of the mainshock motion, and thus to an increased aftershock contribution to the final ODI (with saturation due to the decay in the rate of increase of this contribution), with an increase in R_{rup}. It may be mentioned that even though the nature of variation with respect to R_{rup} is similar in Figures 16(a) and 16(b), greater values of final ODI are obtained in Figure 16(a) for Frame-1 due to the motion being a high-frequency motion and in Figure 16(b) for Frame-3 due to a broad-band motion.

Figure 17 shows the variations in final ODI with Δh for the three example frames, with $\Delta M = 0.3$, $R_{\text{rup}} = 15$ km and $s = 0$ (as considered for Figures 12–14). As expected, the severity of aftershock motions increases for shallow aftershocks (Δh > 0). Shallower aftershock motions are stronger and in effect contain relatively longer period waves (Das and Gupta [24]). This causes greater increase in the aftershock severity for flexible structures, as seen in Figure 17 for Frame-3 (compared to Frame-1 and Frame-2). An unusual increase in ODI is observed in the case of MS2, however, due to the column-sway mechanism wherein all the columns in the third storey show more than 300% increase in their rotational ductility demand from that of the main shock. This leads to a significant increase in the first term of the local DI s and thus to the observed increase in ODI. This increase takes place for the MS2 motion because the aftershock in this case has stronger long-period waves, thus resulting in a larger response of a softened (degraded) structure. It may also be mentioned that Frame-3 is deficient in terms of SCWB from the third storey onward, and thus, a SCWB-non-compliant multi-storeyed frame may be vulnerable to storey mechanism in response to an aftershock of a broad-band main shock. It may also be observed in Figure 17 that for flexible structures, deeper aftershocks ($\Delta h < 0$) cause lesser additional damage as compared to the stiff structures. It may be mentioned that a higher value of ODI in Figure 17 beyond 1 indicates a greater severity of aftershock damage than that caused for ODI = 1. Since the structure is deemed to collapse for $ODI \geq 1$, this implies that greater is the value of ODI beyond 1, more premature is the structure collapse taking place during the aftershock motion.

Figure 18 shows the variations in final ODI with local soil conditions for the three example frames, with $\Delta M = 0.3$, $R_{\text{rup}} = 15$ km, and $\Delta h = 0$ (as considered for Figures 12–14). Here, s = 0, 2 refers to soft soil, and rock or very dense soil type, respectively. It is clear from the figure that different types of soil conditions do not have much effect on the severity of aftershock motion irrespective of the frame period, even though the severity for the soft soil sites is little higher due to a more prominent nonlinear site response during the main shock motion than that during the aftershock, which leads to a relatively greater amplified aftershock motion. For the same reason, Frame-3 in the case of MS2 shows maximum sensitivity with respect to the soil type. The order of magnitudes of the final ODI for various frames in Figures 18(a) and 18(b) can be explained based on the frequency contents of MS1 and MS2 as discussed above in the context of Figure 16.

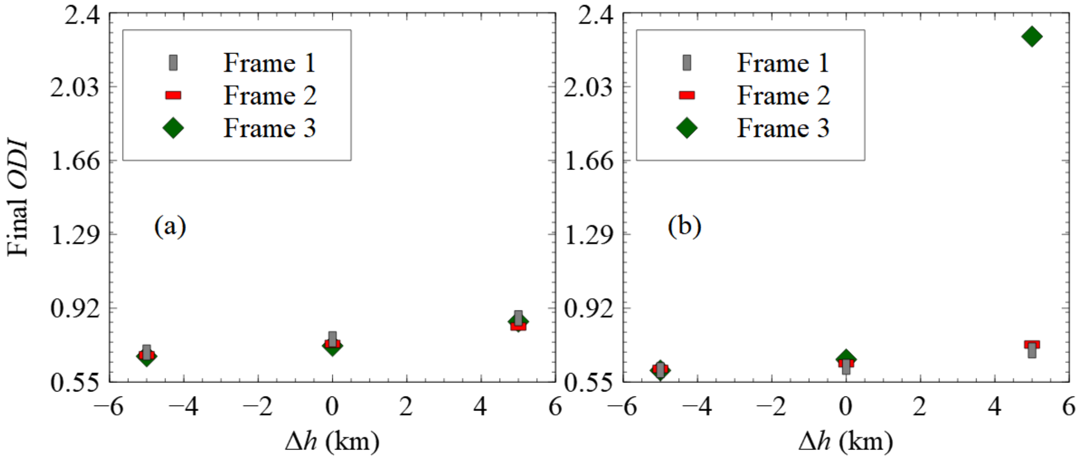

Fig. 17 Variations of final ODI with focal depth difference Δh (Δh > 0 indicates shallower aftershock) for different frames, in the case of initial ODI = 0.6 with (a) MS1 as the main shock motion, (b) MS2 as the main shock motion

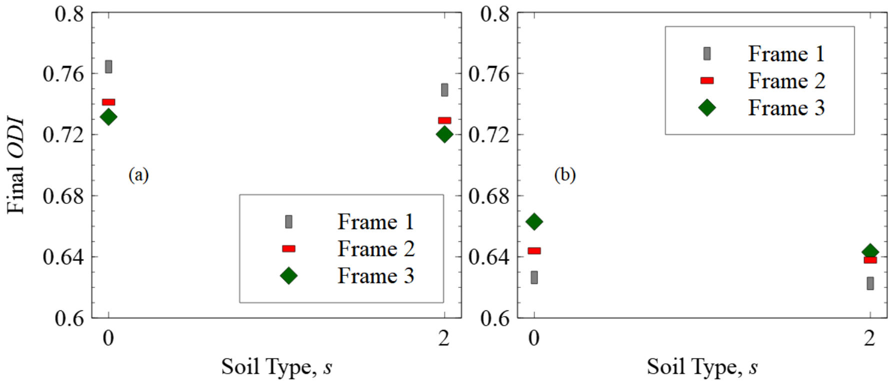

Fig. 18 Variations of final *ODI* with soil type s for different frames, in the case of initial *ODI* = 0.6 with (a) MS1 as the main shock motion, (b) MS2 as the main shock motion

Table 4: Relative ground motion characteristics of the simulated aftershock motions used in Figures 12, 13, and 15–18

Sl. No.	Figure No.	Aftershock Case	PGA Ratio	PSA Ratio at the Period, T (s)							SMD Ratio
				0.05	0.10	0.50	1.00	1.50	3.00	5.00	
1	12	Imperial Valley	0.73	0.74	0.79	0.64	0.62	0.58	0.50	0.44	0.56
2	12	Kern County	0.49	0.49	0.56	0.48	0.70	0.57	0.52	0.39	0.54
3	12	Parkfield	0.69	0.68	0.66	0.61	0.58	0.58	0.54	0.61	0.37
4	12	San Fernando	0.80	0.80	0.75	0.52	0.59	0.59	0.53	0.46	0.56
5	12	Borrego Mountain	0.72	0.71	0.73	0.63	0.59	0.58	0.53	0.47	0.64
6	13	Imperial Valley	0.69	0.73	0.73	0.66	0.56	0.61	0.53	0.42	0.66
7	13	Kern County	0.66	0.64	0.79	0.71	0.52	0.60	0.54	0.45	0.66
8	13	Parkfield	0.71	0.64	0.84	0.60	0.49	0.61	0.53	0.42	0.67
9	13	San Fernando	0.72	0.71	0.73	0.63	0.59	0.58	0.53	0.47	0.64
10	13	Borrego Mountain	0.65	0.65	0.79	0.57	0.55	0.59	0.53	0.45	0.78
11	15(a)	$\Delta M = 0.2$	0.82	0.68	0.96	0.68	0.61	0.70	0.63	0.53	0.71
12	15(a)	$\Delta M = 0.4$	0.63	0.57	0.68	0.52	0.40	0.47	0.39	0.28	0.60
13	15(a)	$\Delta M = 0.6$	0.51	0.42	0.57	0.33	0.31	0.32	0.25	0.19	0.51
14	15(a)	$\Delta M = 0.8$	0.33	0.35	0.44	0.26	0.23	0.23	0.16	0.12	0.44
15	15(b)	$\Delta M = 0.2$	0.63	0.56	0.61	0.76	0.68	0.63	0.53	0.51	0.43
16	15(b)	$\Delta M = 0.4$	0.49	0.44	0.48	0.56	0.48	0.43	0.35	0.30	0.35
17	15(b)	$\Delta M = 0.6$	0.39	0.34	0.39	0.41	0.34	0.28	0.21	0.18	0.28
18	15(b)	$\Delta M = 0.8$	0.31	0.27	0.31	0.31	0.24	0.20	0.15	0.11	0.23
19	16(a)	$R_{\mathrm{rup}} = 10$ km	0.70	0.62	0.81	0.58	0.47	0.58	0.51	0.40	0.66
20	16(a)	$R_{\mathrm{rup}} = 20$ km	0.72	0.66	0.85	0.61	0.51	0.62	0.55	0.43	0.67
21	16(a)	$R_{\mathrm{rup}} = 40$ km	0.73	0.67	0.86	0.62	0.52	0.64	0.56	0.45	0.67
22	16(b)	$R_{\mathrm{rup}} = 10$ km	0.60	0.51	0.55	0.66	0.59	0.54	0.47	0.40	0.39
23	16(b)	$R_{\mathrm{rup}} = 20$ km	0.64	0.54	0.59	0.69	0.63	0.58	0.51	0.43	0.39
24	16(b)	$R_{\mathrm{rup}} = 40$ km	0.66	0.56	0.60	0.70	0.65	0.60	0.52	0.44	0.39
25	17(a)	$\Delta h = -5$ km	0.61	0.63	0.75	0.52	0.39	0.45	0.28	0.25	0.69
26	17(a)	$\Delta h = 0$	0.71	0.64	0.84	0.60	0.49	0.61	0.53	0.42	0.67
27	17(a)	$\Delta h = 5$ km	0.84	0.72	0.91	0.71	0.64	0.83	1.02	1.19	0.65
28	17(b)	$\Delta h = -5$ km	0.52	0.51	0.55	0.59	0.47	0.51	0.25	0.16	0.34
29	17(b)	$\Delta h = 0$	0.69	0.68	0.66	0.61	0.58	0.58	0.54	0.58	0.37
30	17(b)	$\Delta h = 5$ km	0.60	0.55	0.60	0.79	0.80	0.75	0.91	1.12	0.49
31	18(a)	$s = 0$	0.71	0.64	0.84	0.60	0.49	0.61	0.53	0.42	0.67
32	18(a)	$s = 2$	0.69	0.63	0.81	0.57	0.47	0.59	0.53	0.42	0.67
33	18(b)	$s = 0$	0.69	0.68	0.66	0.61	0.58	0.58	0.54	0.58	0.37
34	18(b)	$s = 2$	0.61	0.52	0.56	0.65	0.59	0.55	0.50	0.43	0.39

As already mentioned, various ground motion characteristics of the aftershock motions used in Figures 12, 13, and 15–18 relative to the same characteristics of the MS1 and MS2 motions are given in Table 4. It may be useful to correlate the aftershock-induced additional damage with these ground motion characteristics to make the above observations applicable to the main shock-aftershock sequences in the other regions of interest. Based on the aftershock-induced additional damage observed in Figures 12, 13 and 14–18 and the corresponding relative ground motion parameters, viz., the PSA ratio (around the fundamental period of the structure), SMD ratio, and PGA ratio as shown in Table 4, it is possible to find out when the aftershock induced damage may be ignored and when this damage may be significant. To facilitate this, the visual illustrations of the percentage increase in the aftershock damage vis-a-vis the PSA, SMD, and PGA ratios in the different cases of Table 4 are shown in Figures 19–21 for Frame-1, Frame-2, and Frame-3, respectively. It is evident from these figures that the final *ODI* is likely to be less than 0.62 (i.e., < 3% increase), when (1) the PSA ratio is less than 0.4 (e.g., for Rows 17, 18 in Figures 19–21), (2) the SMD ratio is less than 0.35 (e.g., for Rows 17, 18, 28 in Figures 19–21), and (3) PGA ratio is less than 0.4 (e.g., for Row 17 in Figures 19–21), especially if the SMD of the main shock motion is short. On the other hand, the final *ODI* is likely to be more than 0.72 (i.e., > 20% increase), when (1) the PSA ratio is greater than 0.55 for Frame-1 and Frame-2 (e.g., for Rows 19–21, 31, 32 in Figures 19 and 20) and 0.65 for Frame-3 (e.g., for Rows 19–21, 31, 32 in Figure 21), (2) the SMD ratio is greater than 0.65 (e.g., for Rows 6–8, 10, 31, 32 in Figures 19–21), and (3) the PGA ratio is greater than 0.7 (e.g., for Rows 8, 19–21 in Figure 19–21), unless the motion is a broad-band motion which may reduce the aftershock severity as seen in Figure 12.

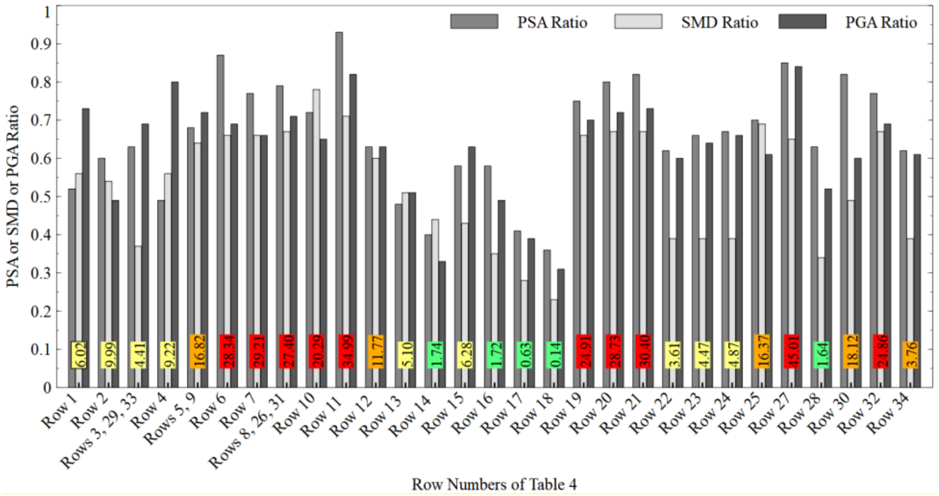

Fig. 19 Visual illustration of percentage increase in aftershock damage vis-à-vis PSA, SMD, and PGA ratios for various rows of Table 4 in the case of Frame-1 (the percentage increase values are given inside the vertical bars)

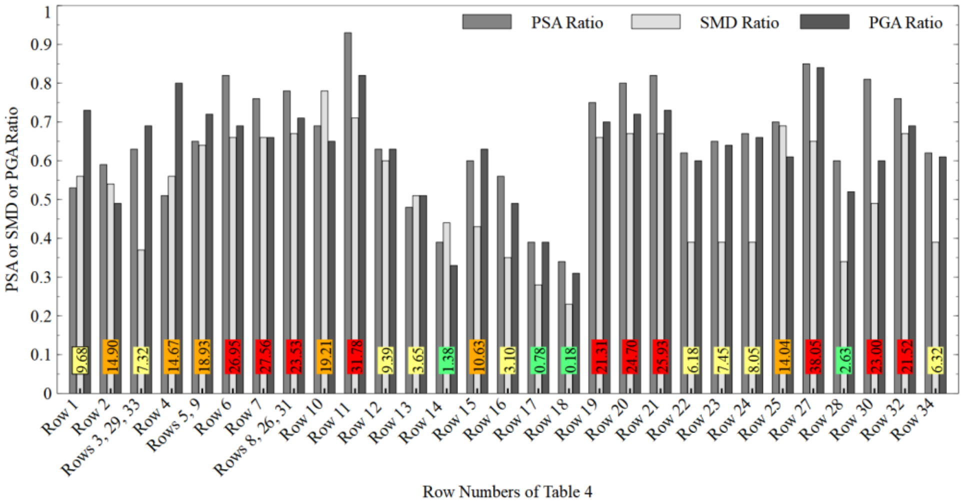

Fig. 20 Visual illustration of percentage increase in aftershock damage vis-à-vis PSA, SMD, and PGA ratios for various rows of Table 4 in the case of Frame-2 (the percentage increase values are given inside the vertical bars)

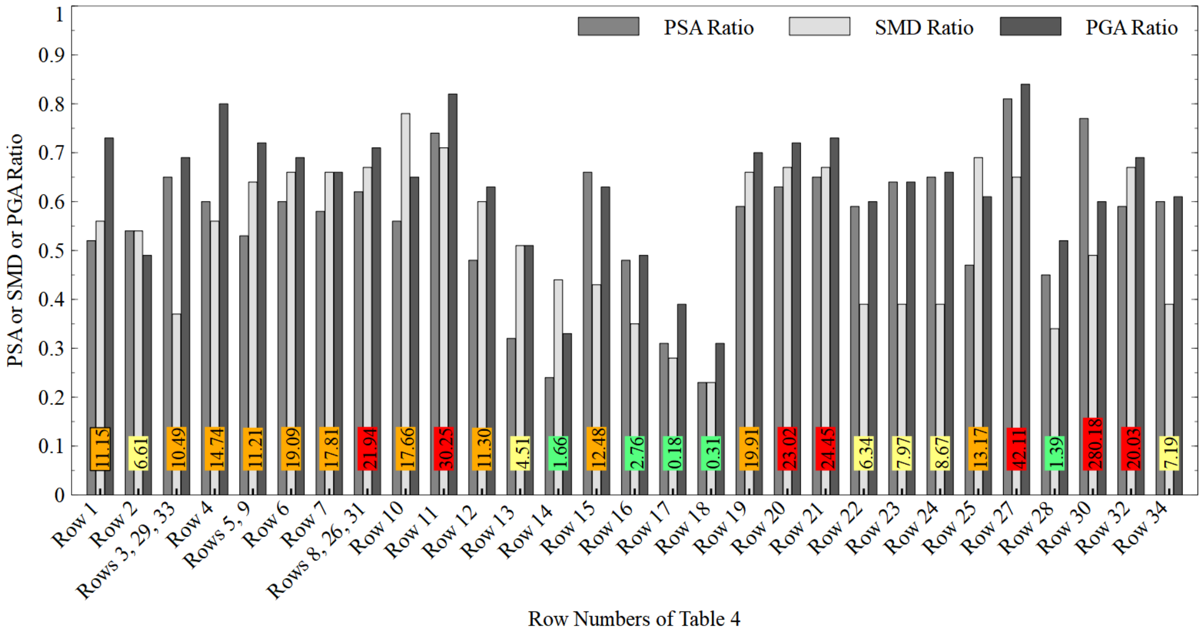

Fig. 21 Visual illustration of percentage increase in aftershock damage vis-à-vis PSA, SMD, and PGA ratios for various rows of Table 4 in the case of Frame-3 (the percentage increase values are given inside the vertical bars)

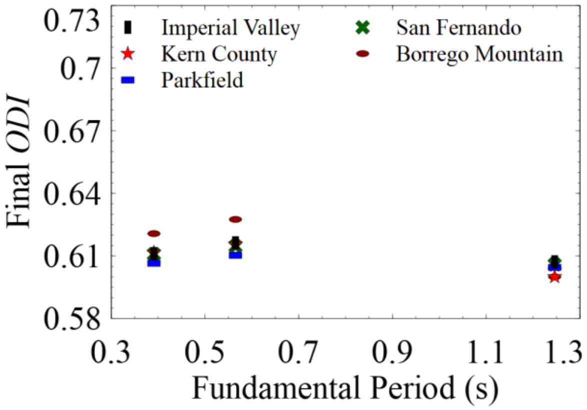

Fig. 22 Variation of final *ODI* with frame period for motions of different time-frequency characteristics (and same PSA spectrum) in the case of initial *ODI* = 0.6 and multiple-aftershocks scenario

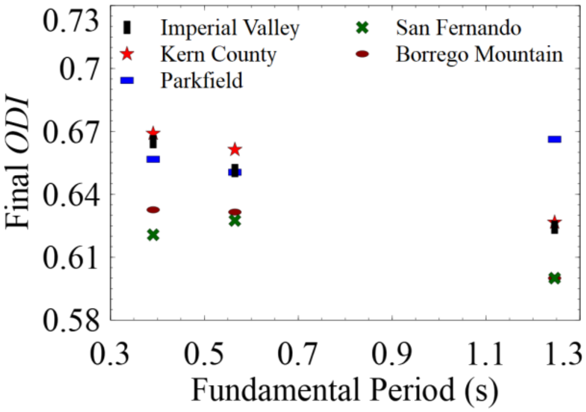

Fig. 23 Variation of final *ODI* with frame period for motions with different PSA spectra (and same time-frequency characteristics) in the case of initial *ODI* = 0.6 and multiple-aftershocks scenario

The above numerical exercise is based on the aftershock sequences simulated by using the conditional models of the aftershock response spectrum and strong-motion duration developed for the 1999 Chi-Chi earthquake and its aftershocks, and thus the relation of the generated aftershock motions to the main shock motions in terms of response spectrum and strong-motion duration is strictly applicable to the seismic region of the 1999 Chi-Chi earthquake, even though there is no similarity of the generated motions with the motions recorded during the Chi-Chi aftershocks in terms of their temporal features. It will be therefore desirable to examine the applicability of the above observations on additional aftershock damage vis-à-vis relative ground motion characteristics in the cases of recorded main shock-aftershock sequences. To this end, four as-recorded main shock-aftershock sequences from two different main shock events are considered. The recorded main shock accelerograms are (i) MS3: N90E component recorded at the CHY039 station, Nantau County, Taiwan during the Chi-Chi main event (17:47 UTC, 20 September 1999) with 7.6 magnitude, (ii) MS4: N90E component recorded at the CHY058 station, Nantau County, Taiwan during the same main event as MS3, (iii) MS5: N90E component recorded at the DGG SAN station, Chile during the Valparaiso main event (22:47 UTC, 3 March 1985) with 7.8 magnitude, and (iv) MS6: N00E component of the same ground motion as MS5. The corresponding recorded aftershock accelerograms are respectively (i) MS3-AS: N90E component recorded at the CHY039 station, Taiwan during the Chi-Chi aftershock event (23:52 UTC, 25 September 1999) with 6.8 magnitude, (ii) MS4-AS: N90E component recorded at the CHY058 station, Taiwan during the same aftershock event as MS3-AS, (iii) MS5-AS: N90E component recorded at the DGG SAN station, Chile during the Valparaiso aftershock event (01:56 UTC, 9 April 1985) with 7.2 magnitude, and (iv) MS6-AS: N00E component of the same ground motion as MS5-AS. The relative ground motion properties of the MS3-AS, MS4-AS, MS5-AS, MS6-AS motions are provided in Table 5 along with the final *ODI*s for the example three frames (with the initial *ODI* fixed at 0.6). Based on these properties and the preceding discussion, it is expected that the additional damage induced by the MS3-AS and MS4-AS motions would be significant, while the additional damage due to the MS5-AS and MS6-AS motions would be insignificant. This is indeed the case as shown by a minimum of 20% increase in the final *ODI*s for five out of six analyses under the MS3-AS and MS4-AS motions, and the additional damage being less than 0.01 (on the *ODI* scale) for all the six analyses under the MS5-AS and MS6-AS motions.

Table 5: Relative ground motion characteristics of the recorded aftershock motions (MS3-AS, MS4-AS, MS5-AS, and MS6-AS)

Sl.	**Aftershock**	**PGA**	**PSA Ratio at the Period, *T* (s)**							**SMD**	**Final *ODI***		
No.	**Case**	**Ratio**	**0.05**	**0.10**	**0.50**	**1.00**	**1.50**	**3.00**	**5.00**	**Ratio**	**F1**	**F2**	**F3**
1	MS3-AS	0.90	0.88	1.02	0.81	0.58	0.63	0.89	0.43	0.67	0.68	0.72	0.72
2	MS4-AS	0.90	0.87	0.90	0.64	0.68	0.81	1.25	0.89	0.63	0.73	0.77	0.98
3	MS5-AS	0.21	0.22	0.28	0.10	0.16	0.22	0.11	0.39	0.56	0.60	0.60	0.60
4	MS6-AS	0.20	0.18	0.15	0.16	0.13	0.17	0.07	0.06	0.54	0.60	0.60	0.60

Note: F1 – Frame 1, F2 – Frame 2, F3 – Frame 3

The above results are based on considering only the contribution of the largest aftershock motion to the total seismic damage. Figures 22 and 23 show the results similar to those in Figures 12 and 13, respectively, for the main shock-aftershock sequences comprising three aftershocks (instead of just one). The moment and local magnitudes of the main shock are considered as 7.6 and 7.3, respectively, here, while the local magnitudes of the aftershocks are considered as 6.8, 6.8 and 6.6, respectively. This sequence of main shock and aftershock magnitudes is based on the magnitudes of the 1999 Chi-Chi earthquake and its aftershocks. Moment magnitudes of the aftershocks are assumed to be same as the local magnitudes. There is no other change in the seismic scenario considered for the results in Figures 12 and 13. Table 6 gives various ground motion characteristics, i.e., PGA, PSA spectrum ordinates at five different periods, and SMD, of the simulated aftershocks motions used in Figures 22 and 23 relative to the same characteristics of the preceding main shock motions. The necessary details of various sequences considered for Figures 12–18 and 22–23 are summarized in Tables A1–A3 of the appendix (the figure numbers S1–S120 given for these sequences refer to the figures provided in the supplementary data file).

Table 6: Relative ground motion characteristics of the aftershock motions used in Figures 22 and 23

Sl.	**Figure**	**Aftershock**	**PGA**	**PSA Ratio at the Period, *T* (s)**							**SMD**
No.	**No.**	**Case**	**Ratio**	**0.05**	**0.10**	**0.50**	**1.00**	**1.50**	**3.00**	**5.00**	**Ratio**
1	22	IV, $M = 6.8$	0.45	0.45	0.48	0.46	0.29	0.29	0.22	0.22	0.48
2	22	IV, $M = 6.6$	0.36	0.34	0.39	0.29	0.19	0.19	0.15	0.16	0.31
3	22	KC, $M = 6.8$	0.30	0.30	0.36	0.29	0.32	0.29	0.23	0.19	0.41
4	22	KC, $M = 6.6$	0.22	0.23	0.27	0.23	0.21	0.19	0.15	0.11	0.36
5	22	PF, $M = 6.8$	0.39	0.38	0.41	0.36	0.26	0.29	0.23	0.23	0.34
6	22	PF, $M = 6.6$	0.35	0.35	0.36	0.29	0.18	0.19	0.20	0.12	0.32
7	22	SF, $M = 6.8$	0.44	0.44	0.50	0.31	0.29	0.29	0.24	0.23	0.43
8	22	SF, $M = 6.6$	0.37	0.37	0.40	0.27	0.19	0.20	0.16	0.15	0.43
9	22	BM, $M = 6.8$	0.49	0.49	0.50	0.35	0.31	0.28	0.24	0.19	0.54
10	22	BM, $M = 6.6$	0.36	0.36	0.39	0.26	0.24	0.19	0.15	0.11	0.44
11	23	IV, $M = 6.8$	0.43	0.39	0.47	0.37	0.31	0.30	0.24	0.20	0.56
12	23	IV, $M = 6.6$	0.37	0.34	0.39	0.26	0.21	0.20	0.15	0.11	0.46
13	23	KC, $M = 6.8$	0.52	0.49	0.43	0.39	0.29	0.29	0.24	0.19	0.49

14	23	KC, M = 6.6	0.41	0.39	0.33	0.29	0.21	0.20	0.15	0.11	0.42
15	23	PF, M = 6.8	0.46	0.38	0.53	0.36	0.31	0.31	0.24	0.18	0.55
16	23	PF, M = 6.6	0.38	0.31	0.42	0.25	0.20	0.21	0.15	0.14	0.46
17	23	SF, M = 6.8	0.49	0.49	0.50	0.35	0.31	0.28	0.24	0.19	0.54
18	23	SF, M = 6.6	0.36	0.36	0.39	0.26	0.24	0.19	0.15	0.11	0.44
19	23	BM, M = 6.8	0.39	0.41	0.45	0.41	0.29	0.29	0.24	0.19	0.67
20	23	BM, M = 6.6	0.37	0.36	0.38	0.26	0.21	0.20	0.15	0.11	0.57

It is clear from the comparison of Figures 12–13 and Figures 22–23 that the inferences drawn for the single-aftershock scenario are applicable to the multiple-aftershocks scenario also. The drop in ODIs observed for Frame-3 is more pronounced because the aftershocks considered for the multiple-aftershocks scenario are much smaller in magnitude (than the main shock) in comparison with the aftershock considered in the single aftershock case. Due to this, the multiple-scenario aftershocks are not as rich in long-period waves as the single aftershock, and thus the response of Frame-3 (with a longer period) gets reduced. For the Parkfield motion case in Figure 23, where the main shock motion (i.e., the MS1 motion) is a narrow-band, high-frequency motion, Frame-3 incurs a little increase in damage due to the greater higher-mode response contribution and three large aftershock motions. Considering that the situations highlighted in the case of single-aftershock scenario for significant effects of aftershocks on damage-based seismic design are generally applicable for a multiple-aftershocks scenario also, the aftershock severity may be considered high for small values of ΔM and positive values of Δh, provided the main shock motion is a sufficiently long and/or high-frequency motion. To illustrate, we consider the S00E component of the motion recorded at the station USC0060 during the 1994 Northridge earthquake as the main shock motion. The SMD of this accelerogram is 16.98 s as per the definition in Trifunac and Brady [43], and the dominant period is 0.16 s. Assuming that this motion corresponds to the event of 6.5 magnitude, the corresponding aftershock motion generated for $\Delta M = 0.2$, $\Delta h = 5$ km, s = 0 (Das and Gupta [24, 42]) will cause the final ODIs of 0.848 and 1.032, respectively, for Frame-1 and Frame-3 in the case of the initial ODI of 0.6. On the other hand, we may consider the N90E component of the motion recorded at the station C070 during the 1999 Chi-Chi earthquake as the main shock motion to illustrate the case where the effects of aftershocks may be ignored as in the conventional seismic design, provided the value of ΔM is large and the value of Δh is negative. The SMD of this accelerogram is 55.6 s as per the definition in Trifunac and Brady [43], and the dominant period is 0.56 s. Assuming that this motion corresponds to the event of 7.0 magnitude, the corresponding aftershock motion generated for $\Delta M = 0.8$, $\Delta h = -5$ km, s = 0 (Das and Gupta [24, 42]) will cause the final ODIs to be less than 0.605 for Frame-1 and Frame-3 in the case of the initial ODI of 0.6. There is a negligible increase in damage due to the aftershock motion in this case despite a much larger value of SMD (compared to the Northridge motion) because of the dominating effects of ΔM, Δh and energy distribution in the main shock and aftershock motions.

SUMMARY AND CONCLUSIONS

A systematic investigation has been carried out on the contribution of aftershock motions to the cumulative structural damage in a building designed for the main shock in a given seismic scenario. This investigation is based on simulated main shock and aftershock ground motions for a variety of seismological scenarios, and energy distribution and time-frequency characteristics of the main shock motion. It has been assumed that the response spectrum and time-frequency characteristics of the aftershock motions are related to the response spectrum and time-frequency characteristics of the preceding main shock motion. Based on three code-designed concrete bare frames having different fundamental periods, it has been found that longer is the strong motion duration of the main shock motion, greater will be the additional damage-causing ability of its aftershocks. Also, one- and two-storey structures are more vulnerable to the aftershock-induced damage, when those are subjected to a higher-frequency main shock ground motion instead of a broad-band motion, with the additional damage being more than 10%. Tall and flexible structures are relatively less vulnerable to aftershocks, as compared to the short-height structures, in the case of a high-frequency main shock motion. However, there is a possibility that a SCWB-non-compliant tall frame undergoes the column-sway mechanism in response to an aftershock of a broad-band main shock motion. Further, a parametric study has shown that the severity of aftershock motions increases significantly (> 35%) for the shallower aftershock events (in comparison with the main shock motions), especially for the flexible structures, which may collapse prematurely (final $ODI > 1$). Finally, the relative ground motion properties of aftershocks show that the effect of aftershocks may be ignored (additional damage < 3%), when the PSA, SMD, and PGA ratios are respectively within 0.40, 0.35, and 0.40. On the other hand, the aftershock damage can be significant (> 20%), when the PSA, SMD, and PGA ratios respectively exceed 0.55, 0.65, and 0.70. Depending on the above findings, it may be prudent to increase yield capacities of the frame sections and/or ductility capacities of the plastic hinges beyond the levels needed for the main shock alone.

This study has considered a limited numbers of RC frames and main shock-aftershock sequences wherein the aftershock motions have been simulated by using the median level estimates of the conditional scaling models (of PSV spectrum and duration) developed for the seismic region of the 1999 Chi-Chi earthquake and its aftershocks. The consideration of higher confidence levels and/or conditional scaling models for other seismic regions should lead to only quantitative changes in the results of the numerical study carried out. Further, the quantification of the damage states of various plastic hinges via different damage models, along with the consideration of frames with a variety of collapse mechanisms, would be needed to firmly establish the conclusions of this study.

SUPPLEMENTAL DATA FILE

Figures S1–S120 mentioned in the text are available online on the Journal website (https://iset.org.in/issues).

APPENDIX

Table A1: Details of normalized sequences used in Figures 12, 13, and 15–18 for different frames

Sl. No.	Figure No.	Normalized Sequence No.	MS Seed Motion	Target MS Spectrum	Frame	Seismological Details for MS				Seismological Details for AS				Figure No. for Scaled Sequence
						M_L	M_W	R_{rup} (km)	s	M_L	R_{rup} (km)	Δh (km)	s	
1	12	01	IV	SF	Frame-1	6.1	6.2	15.0	0	5.8	15.0	0.0	0	S1
2	12	01	IV	SF	Frame-2	6.1	6.2	15.0	0	5.8	15.0	0.0	0	S2
3	12	01	IV	SF	Frame-3	6.1	6.2	15.0	0	5.8	15.0	0.0	0	S3
4	12	02	KC	SF	Frame-1	6.1	6.2	15.0	0	5.8	15.0	0.0	0	S4
5	12	02	KC	SF	Frame-2	6.1	6.2	15.0	0	5.8	15.0	0.0	0	S5
6	12	02	KC	SF	Frame-3	6.1	6.2	15.0	0	5.8	15.0	0.0	0	S6
7	12	03	PF	SF	Frame-1	6.1	6.2	15.0	0	5.8	15.0	0.0	0	S7
8	12	03	PF	SF	Frame-2	6.1	6.2	15.0	0	5.8	15.0	0.0	0	S8
9	12	03	PF	SF	Frame-3	6.1	6.2	15.0	0	5.8	15.0	0.0	0	S9
10	12	04	SF	SF	Frame-1	6.1	6.2	15.0	0	5.8	15.0	0.0	0	S10
11	12	04	SF	SF	Frame-2	6.1	6.2	15.0	0	5.8	15.0	0.0	0	S11
12	12	04	SF	SF	Frame-3	6.1	6.2	15.0	0	5.8	15.0	0.0	0	S12
13	12	05	BM	SF	Frame-1	6.1	6.2	15.0	0	5.8	15.0	0.0	0	S13
14	12	05	BM	SF	Frame-2	6.1	6.2	15.0	0	5.8	15.0	0.0	0	S14
15	12	05	BM	SF	Frame-3	6.1	6.2	15.0	0	5.8	15.0	0.0	0	S15
16	13	06	BM	IV	Frame-1	6.1	6.2	15.0	0	5.8	15.0	0.0	0	S16
17	13	06	BM	IV	Frame-2	6.1	6.2	15.0	0	5.8	15.0	0.0	0	S17
18	13	06	BM	IV	Frame-3	6.1	6.2	15.0	0	5.8	15.0	0.0	0	S18
19	13	07	BM	KC	Frame-1	6.1	6.2	15.0	0	5.8	15.0	0.0	0	S19
20	13	07	BM	KC	Frame-2	6.1	6.2	15.0	0	5.8	15.0	0.0	0	S20
21	13	07	BM	KC	Frame-3	6.1	6.2	15.0	0	5.8	15.0	0.0	0	S21
22	13	08	BM	PF	Frame-1	6.1	6.2	15.0	0	5.8	15.0	0.0	0	S22
23	13	08	BM	PF	Frame-2	6.1	6.2	15.0	0	5.8	15.0	0.0	0	S23
24	13	08	BM	PF	Frame-3	6.1	6.2	15.0	0	5.8	15.0	0.0	0	S24
25	13	05	BM	SF	Frame-1	6.1	6.2	15.0	0	5.8	15.0	0.0	0	S13
26	13	05	BM	SF	Frame-2	6.1	6.2	15.0	0	5.8	15.0	0.0	0	S14
27	13	05	BM	SF	Frame-3	6.1	6.2	15.0	0	5.8	15.0	0.0	0	S15
28	13	09	BM	BM	Frame-1	6.1	6.2	15.0	0	5.8	15.0	0.0	0	S25
29	13	09	BM	BM	Frame-2	6.1	6.2	15.0	0	5.8	15.0	0.0	0	S26
30	13	09	BM	BM	Frame-3	6.1	6.2	15.0	0	5.8	15.0	0.0	0	S27
31	15(a)	10	BM	PF	Frame-1	7.0	7.0	15.0	0	6.8	15.0	0.0	0	S28
32	15(a)	10	BM	PF	Frame-2	7.0	7.0	15.0	0	6.8	15.0	0.0	0	S29
33	15(a)	10	BM	PF	Frame-3	7.0	7.0	15.0	0	6.8	15.0	0.0	0	S30
34	15(a)	11	BM	PF	Frame-1	7.0	7.0	15.0	0	6.6	15.0	0.0	0	S31
35	15(a)	11	BM	PF	Frame-2	7.0	7.0	15.0	0	6.6	15.0	0.0	0	S32
36	15(a)	11	BM	PF	Frame-3	7.0	7.0	15.0	0	6.6	15.0	0.0	0	S33
37	15(a)	12	BM	PF	Frame-1	7.0	7.0	15.0	0	6.4	15.0	0.0	0	S34
38	15(a)	12	BM	PF	Frame-2	7.0	7.0	15.0	0	6.4	15.0	0.0	0	S35
39	15(a)	12	BM	PF	Frame-3	7.0	7.0	15.0	0	6.4	15.0	0.0	0	S36
40	15(a)	13	BM	PF	Frame-1	7.0	7.0	15.0	0	6.2	15.0	0.0	0	S37
41	15(a)	13	BM	PF	Frame-2	7.0	7.0	15.0	0	6.2	15.0	0.0	0	S38
42	15(a)	13	BM	PF	Frame-3	7.0	7.0	15.0	0	6.2	15.0	0.0	0	S39
43	15(b)	14	PF	SF	Frame-1	7.0	7.0	15.0	0	6.8	15.0	0.0	0	S40
44	15(b)	14	PF	SF	Frame-2	7.0	7.0	15.0	0	6.8	15.0	0.0	0	S41
45	15(b)	14	PF	SF	Frame-3	7.0	7.0	15.0	0	6.8	15.0	0.0	0	S42

46	15(b)	15	PF	SF	Frame-1	7.0	7.0	15.0	0	6.6	15.0	0.0	0	S43
47	15(b)	15	PF	SF	Frame-2	7.0	7.0	15.0	0	6.6	15.0	0.0	0	S44
48	15(b)	15	PF	SF	Frame-3	7.0	7.0	15.0	0	6.6	15.0	0.0	0	S45
49	15(b)	16	PF	SF	Frame-1	7.0	7.0	15.0	0	6.4	15.0	0.0	0	S46
50	15(b)	16	PF	SF	Frame-2	7.0	7.0	15.0	0	6.4	15.0	0.0	0	S47
51	15(b)	16	PF	SF	Frame-3	7.0	7.0	15.0	0	6.4	15.0	0.0	0	S48
52	15(b)	17	PF	SF	Frame-1	7.0	7.0	15.0	0	6.2	15.0	0.0	0	S49
53	15(b)	17	PF	SF	Frame-2	7.0	7.0	15.0	0	6.2	15.0	0.0	0	S50
54	15(b)	17	PF	SF	Frame-3	7.0	7.0	15.0	0	6.2	15.0	0.0	0	S51
55	16(a)	18	BM	PF	Frame-1	6.1	6.2	10.0	0	5.8	10.0	0.0	0	S52
56	16(a)	18	BM	PF	Frame-2	6.1	6.2	10.0	0	5.8	10.0	0.0	0	S53
57	16(a)	18	BM	PF	Frame-3	6.1	6.2	10.0	0	5.8	10.0	0.0	0	S54
58	16(a)	19	BM	PF	Frame-1	6.1	6.2	20.0	0	5.8	20.0	0.0	0	S55
59	16(a)	19	BM	PF	Frame-2	6.1	6.2	20.0	0	5.8	20.0	0.0	0	S56
60	16(a)	19	BM	PF	Frame-3	6.1	6.2	20.0	0	5.8	20.0	0.0	0	S57
61	16(a)	20	BM	PF	Frame-1	6.1	6.2	40.0	0	5.8	40.0	0.0	0	S58
62	16(a)	20	BM	PF	Frame-2	6.1	6.2	40.0	0	5.8	40.0	0.0	0	S59
63	16(a)	20	BM	PF	Frame-3	6.1	6.2	40.0	0	5.8	40.0	0.0	0	S60
64	16(b)	21	PF	SF	Frame-1	6.1	6.2	10.0	0	5.8	10.0	0.0	0	S61
65	16(b)	21	PF	SF	Frame-2	6.1	6.2	10.0	0	5.8	10.0	0.0	0	S62
66	16(b)	21	PF	SF	Frame-3	6.1	6.2	10.0	0	5.8	10.0	0.0	0	S63
67	16(b)	22	PF	SF	Frame-1	6.1	6.2	20.0	0	5.8	20.0	0.0	0	S64
68	16(b)	22	PF	SF	Frame-2	6.1	6.2	20.0	0	5.8	20.0	0.0	0	S65
69	16(b)	22	PF	SF	Frame-3	6.1	6.2	20.0	0	5.8	20.0	0.0	0	S66
70	16(b)	23	PF	SF	Frame-1	6.1	6.2	40.0	0	5.8	40.0	0.0	0	S67
71	16(b)	23	PF	SF	Frame-2	6.1	6.2	40.0	0	5.8	40.0	0.0	0	S68
72	16(b)	23	PF	SF	Frame-3	6.1	6.2	40.0	0	5.8	40.0	0.0	0	S69
73	17(a)	24	BM	PF	Frame-1	6.1	6.2	15.0	0	5.8	15.0	-5.0	0	S70
74	17(a)	24	BM	PF	Frame-2	6.1	6.2	15.0	0	5.8	15.0	-5.0	0	S71
75	17(a)	24	BM	PF	Frame-3	6.1	6.2	15.0	0	5.8	15.0	-5.0	0	S72
76	17(a)	08	BM	PF	Frame-1	6.1	6.2	15.0	0	5.8	15.0	0.0	0	S22
77	17(a)	08	BM	PF	Frame-2	6.1	6.2	15.0	0	5.8	15.0	0.0	0	S23
78	17(a)	08	BM	PF	Frame-3	6.1	6.2	15.0	0	5.8	15.0	0.0	0	S24
79	17(a)	25	BM	PF	Frame-1	6.1	6.2	15.0	0	5.8	15.0	5.0	0	S73
80	17(a)	25	BM	PF	Frame-2	6.1	6.2	15.0	0	5.8	15.0	5.0	0	S74
81	17(a)	25	BM	PF	Frame-3	6.1	6.2	15.0	0	5.8	15.0	5.0	0	S75
82	17(b)	26	PF	SF	Frame-1	6.1	6.2	15.0	0	5.8	15.0	-5.0	0	S76
83	17(b)	26	PF	SF	Frame-2	6.1	6.2	15.0	0	5.8	15.0	-5.0	0	S77
84	17(b)	26	PF	SF	Frame-3	6.1	6.2	15.0	0	5.8	15.0	-5.0	0	S78
85	17(b)	03	PF	SF	Frame-1	6.1	6.2	15.0	0	5.8	15.0	0.0	0	S7
86	17(b)	03	PF	SF	Frame-2	6.1	6.2	15.0	0	5.8	15.0	0.0	0	S8
87	17(b)	03	PF	SF	Frame-3	6.1	6.2	15.0	0	5.8	15.0	0.0	0	S9
88	17(b)	27	PF	SF	Frame-1	6.1	6.2	15.0	0	5.8	15.0	5.0	0	S79
89	17(b)	27	PF	SF	Frame-2	6.1	6.2	15.0	0	5.8	15.0	5.0	0	S80
90	17(b)	27	PF	SF	Frame-3	6.1	6.2	15.0	0	5.8	15.0	5.0	0	S81
91	18(a)	08	BM	PF	Frame-1	6.1	6.2	15.0	0	5.8	15.0	0.0	0	S22
92	18(a)	08	BM	PF	Frame-2	6.1	6.2	15.0	0	5.8	15.0	0.0	0	S23
93	18(a)	08	BM	PF	Frame-3	6.1	6.2	15.0	0	5.8	15.0	0.0	0	S24
94	18(a)	28	BM	PF	Frame-1	6.1	6.2	15.0	2	5.8	15.0	0.0	2	S82
95	18(a)	28	BM	PF	Frame-2	6.1	6.2	15.0	2	5.8	15.0	0.0	2	S83
96	18(a)	28	BM	PF	Frame-3	6.1	6.2	15.0	2	5.8	15.0	0.0	2	S84
97	18(b)	03	PF	SF	Frame-1	6.1	6.2	15.0	0	5.8	15.0	0.0	0	S7
98	18(b)	03	PF	SF	Frame-2	6.1	6.2	15.0	0	5.8	15.0	0.0	0	S8
99	18(b)	03	PF	SF	Frame-3	6.1	6.2	15.0	0	5.8	15.0	0.0	0	S9
100	18(b)	29	PF	SF	Frame-1	6.1	6.2	15.0	2	5.8	15.0	0.0	2	S85
101	18(b)	29	PF	SF	Frame-2	6.1	6.2	15.0	2	5.8	15.0	0.0	2	S86
102	18(b)	29	PF	SF	Frame-3	6.1	6.2	15.0	2	5.8	15.0	0.0	2	S87

Note: MS – Main shock, AS – Aftershock, M_L – Local Magnitude, M_W – Moment Magnitude, IV – Imperial Valley, KC – Kern County, PF – Parkfield, SF – San Fernando, BM – Borrego Mountain.

Table A2: Details of normalized sequences used in Figure 14 for different frames

Sl. No.	**Fig. No.**	**Norm. Seq. No.**	**MS Seed Motion**	**Target MS Spectrum**	**Frame**	**Target *ODI***	**Seismological Details for MS**				**Seismological Details for AS**				**Fig. No. for Scaled Seq.**
							M_L	M_W	R_{rup} **(km)**	s	M_L	R_{rup} **(km)**	Δh **(km)**	s	
1	14	08	BM	PF	Frame-1	0.40	6.1	6.2	15.0	0	5.8	15.0	0.0	0	S88
2	14	08	BM	PF	Frame-2	0.40	6.1	6.2	15.0	0	5.8	15.0	0.0	0	S89
3	14	08	BM	PF	Frame-3	0.40	6.1	6.2	15.0	0	5.8	15.0	0.0	0	S90
4	14	08	BM	PF	Frame-1	0.60	6.1	6.2	15.0	0	5.8	15.0	0.0	0	S22
5	14	08	BM	PF	Frame-2	0.60	6.1	6.2	15.0	0	5.8	15.0	0.0	0	S23
6	14	08	BM	PF	Frame-3	0.60	6.1	6.2	15.0	0	5.8	15.0	0.0	0	S24
7	14	08	BM	PF	Frame-1	0.80	6.1	6.2	15.0	0	5.8	15.0	0.0	0	S91
8	14	08	BM	PF	Frame-2	0.80	6.1	6.2	15.0	0	5.8	15.0	0.0	0	S92
9	14	08	BM	PF	Frame-3	0.80	6.1	6.2	15.0	0	5.8	15.0	0.0	0	S93

Note: MS – Main shock, AS – Aftershock, M_L – Local Magnitude, M_W – Moment Magnitude, IV – Imperial Valley, KC – Kern County, PF – Parkfield, SF – San Fernando, BM – Borrego Mountain.

Table A3: Details of normalized sequences used in Figures 22 and 23 for different frames

Sl. No.	Fig. No.	Norm. Seq. No.	MS Seed Motion	Target MS Spectrum	Frame	Seismological Details for MS				Seismological Details for AS						Fig. No. for Scaled Seq.
						M_L	M_W	R_{rup} (km)	s	M_L			R_{rup} (km)	Δh (km)	s	
										AS1	AS2	AS3				
1	22	30	IV	SF	Frame-1	7.3	7.6	15.0	0	6.8	6.8	6.6	15.0	0.0	0	S94
2	22	30	IV	SF	Frame-2	7.3	7.6	15.0	0	6.8	6.8	6.6	15.0	0.0	0	S95
3	22	30	IV	SF	Frame-3	7.3	7.6	15.0	0	6.8	6.8	6.6	15.0	0.0	0	S96
4	22	31	KC	SF	Frame-1	7.3	7.6	15.0	0	6.8	6.8	6.6	15.0	0.0	0	S97
5	22	31	KC	SF	Frame-2	7.3	7.6	15.0	0	6.8	6.8	6.6	15.0	0.0	0	S98
6	22	31	KC	SF	Frame-3	7.3	7.6	15.0	0	6.8	6.8	6.6	15.0	0.0	0	S99
7	22	32	PF	SF	Frame-1	7.3	7.6	15.0	0	6.8	6.8	6.6	15.0	0.0	0	S100
8	22	32	PF	SF	Frame-2	7.3	7.6	15.0	0	6.8	6.8	6.6	15.0	0.0	0	S101
9	22	32	PF	SF	Frame-3	7.3	7.6	15.0	0	6.8	6.8	6.6	15.0	0.0	0	S102
10	22	33	SF	SF	Frame-1	7.3	7.6	15.0	0	6.8	6.8	6.6	15.0	0.0	0	S103
11	22	33	SF	SF	Frame-2	7.3	7.6	15.0	0	6.8	6.8	6.6	15.0	0.0	0	S104
12	22	33	SF	SF	Frame-3	7.3	7.6	15.0	0	6.8	6.8	6.6	15.0	0.0	0	S105
13	22	34	BM	SF	Frame-1	7.3	7.6	15.0	0	6.8	6.8	6.6	15.0	0.0	0	S106
14	22	34	BM	SF	Frame-2	7.3	7.6	15.0	0	6.8	6.8	6.6	15.0	0.0	0	S107
15	22	34	BM	SF	Frame-3	7.3	7.6	15.0	0	6.8	6.8	6.6	15.0	0.0	0	S108
16	23	35	BM	IV	Frame-1	7.3	7.6	15.0	0	6.8	6.8	6.6	15.0	0.0	0	S109
17	23	35	BM	IV	Frame-2	7.3	7.6	15.0	0	6.8	6.8	6.6	15.0	0.0	0	S110
18	23	35	BM	IV	Frame-3	7.3	7.6	15.0	0	6.8	6.8	6.6	15.0	0.0	0	S111
19	23	36	BM	KC	Frame-1	7.3	7.6	15.0	0	6.8	6.8	6.6	15.0	0.0	0	S112
20	23	36	BM	KC	Frame-2	7.3	7.6	15.0	0	6.8	6.8	6.6	15.0	0.0	0	S113
21	23	36	BM	KC	Frame-3	7.3	7.6	15.0	0	6.8	6.8	6.6	15.0	0.0	0	S114
22	23	37	BM	PF	Frame-1	7.3	7.6	15.0	0	6.8	6.8	6.6	15.0	0.0	0	S115
23	23	37	BM	PF	Frame-2	7.3	7.6	15.0	0	6.8	6.8	6.6	15.0	0.0	0	S116
24	23	37	BM	PF	Frame-3	7.3	7.6	15.0	0	6.8	6.8	6.6	15.0	0.0	0	S117
25	23	34	BM	SF	Frame-1	7.3	7.6	15.0	0	6.8	6.8	6.6	15.0	0.0	0	S106
26	23	34	BM	SF	Frame-2	7.3	7.6	15.0	0	6.8	6.8	6.6	15.0	0.0	0	S107
27	23	34	BM	SF	Frame-3	7.3	7.6	15.0	0	6.8	6.8	6.6	15.0	0.0	0	S108
28	23	38	BM	BM	Frame-1	7.3	7.6	15.0	0	6.8	6.8	6.6	15.0	0.0	0	S118
29	23	38	BM	BM	Frame-2	7.3	7.6	15.0	0	6.8	6.8	6.6	15.0	0.0	0	S119
30	23	38	BM	BM	Frame-3	7.3	7.6	15.0	0	6.8	6.8	6.6	15.0	0.0	0	S120

Note: MS – Main shock, AS – Aftershock, AS1 – 1st aftershock, AS2 – 2nd aftershock, AS3 – 3rd aftershock, M_L – Local Magnitude, M_W – Moment Magnitude, IV – Imperial Valley, KC – Kern County, PF – Parkfield, SF – San Fernando, BM – Borrego Mountain.

REFERENCES

1. Das, S., Gupta, V.K. and Srimahavishnu, V. (2007). "Damage-Based Design with no Repairs for Multiple Events and Its Sensitivity to Seismicity Model", *Earthquake Engineering & Structural Dynamics, Vol. 36, No. 3, pp. 307–325.*
2. Sunasaka, Y. and Kiremidjian, A.S. (1993). "A Method for Structural Safety Evaluation under Mainshock-Aftershock Earthquake Sequences", *Technical Report 105, Blume Earthquake Engineering Center, Stanford University, Stanford, U.S.A.*
3. Mahin, S.A. (1980). "Effects of Duration and Aftershocks on Inelastic Design Earthquakes", *Proceedings of the Seventh World Conference on Earthquake Engineering, Istanbul, Turkey, Vol. V, pp. 677–680.*
4. Spence, R. and D'Ayala, D. (1999). "Damage Assessment and Analysis of the 1997 Umbria-Marche Earthquake", *Structural Engineering International, Vol. 9, No. 3, pp. 229–233.*
5. USGS (2000). "Implications for Earthquake Risk Reduction in the United States from the Kocaeli, Turkey, Earthquake of August 17, 1999", *Circular 1193, United States Geological Survey, Denver, U.S.A.*
6. Jalayer, F., Asprone, D., Prota, A. and Manfredi, G. (2011). "A Decision Support System for Post-Earthquake Reliability Assessment of Structures Subjected to Aftershocks: An Application to L'Aquila Earthquake, 2009", *Bulletin of Earthquake Engineering, Vol. 9, No. 4, pp. 997–1014.*

7. Amadio, C., Fragiacomo, M. and Rajgelj, S. (2003). “The Effects of Repeated Earthquake Ground Motions on the Non-Linear Response of SDOF Systems”, *Earthquake Engineering & Structural Dynamics, Vol. 32, No. 2, pp. 291–308*.
8. Fragiacomo, M., Amadio, C. and Macorini, L. (2004). “Seismic Response of Steel Frames under Repeated Earthquake Ground Motions”, *Engineering Structures, Vol. 26, No. 13, pp. 2021–2035*.
9. Li, Q. and Ellingwood, B.R. (2007). “Performance Evaluation and Damage Assessment of Steel Frame Buildings under Main Shock-Aftershock Sequences”, *Earthquake Engineering & Structural Dynamics, Vol. 36, No. 3, pp. 405–427*.
10. Hatzigeorgiou, G.D. and Beskos, D.E. (2009). “Inelastic Displacement Ratios for SDOF Structures Subjected to Repeated Earthquakes”, *Engineering Structures, Vol. 31, No. 11, pp. 2744–2755*.
11. Hatzigeorgiou, G.D. and Liolios, A.A. (2010). “Nonlinear Behaviour of RC Frames under Repeated Strong Ground Motions”, *Soil Dynamics and Earthquake Engineering, Vol. 30, No. 10, pp. 1010–1025*.
12. Hatzigeorgiou, G.D. (2010). “Ductility Demand Spectra for Multiple Near- and Far-Fault Earthquakes”, *Soil Dynamics and Earthquake Engineering, Vol. 30, No. 4, pp. 170–183*.
13. Hatzigeorgiou, G.D. (2010). “Behaviour Factors for Nonlinear Structures Subjected to Multiple Near-Fault Earthquakes”, *Computers & Structures, Vol. 88, No. 5–6, pp. 309–321*.
14. Hatzigeorgiou, G.D. (2010). “Ductility Demands Control under Repeated Earthquakes Using Appropriate Force Reduction Factors”, *Journal of Earthquake and Tsunami, Vol. 4, No. 3, pp. 231–250*.
15. Moustafa, A. and Takewaki, I. (2010). “Modeling Critical Ground-Motion Sequences for Inelastic Structures”, *Advances in Structural Engineering, Vol. 13, No. 4, pp. 665–680*.
16. Ruiz-Garcia, J. and Negrete-Manriquez, J.C. (2011). “Evaluation of Drift Demands in Existing Steel Frames under As-recorded Far-Field and Near-Fault Mainshock Aftershock Seismic Sequences”, *Engineering Structures, Vol. 33, No. 2, pp. 621–634*.
17. Goda, K. and Taylor, C.A. (2012). “Effects of Aftershocks on Peak Ductility Demand due to Strong Ground Motion Records from Shallow Crustal Earthquakes”, *Earthquake Engineering & Structural Dynamics, Vol. 41, No. 15, pp. 2311–2330*.
18. Goda, K. (2012). “Nonlinear Response Potential of Mainshock–Aftershock Sequences from Japanese Earthquakes”, *Bulletin of the Seismological Society of America, Vol. 102, No. 5, pp. 2139–2156*.
19. Yeo, G.L. and Cornell, C.A. (2005). “Stochastic Characterization and Decision Bases under Time-Dependent Aftershock Risk in Performance-Based Earthquake Engineering”, *Report PEER 2005/13, Pacific Earthquake Engineering Research Center, University of California, Berkeley, U.S.A.*
20. Luco, N., Bazzurro, P. and Cornell, C.A. (2004). “Dynamic versus Static Computation of the Residual Capacity of a Mainshock-Damaged Building to Withstand an Aftershock”, *Proceedings of the 13th World Conference on Earthquake Engineering, Vancouver, Canada, Paper 2405 (on CD)*.
21. Gupta, V.K., Nielsen, S.R.K. and Kirkegaard, P.H. (2001). “A Preliminary Prediction of Seismic Damage-Based Degradation in RC Structures”, *Earthquake Engineering & Structural Dynamics, Vol. 30, No. 7, pp. 981–993*.
22. Hancock, J., Watson-Lamprey, J., Abrahamson, N.A., Bommer, J.J., Markatis, A., McCoy, E. and Mendis, R. (2006). “An Improved Method of Matching Response Spectra of Recorded Earthquake Ground Motion Using Wavelets”, *Journal of Earthquake Engineering, Vol. 10, No. 1, pp. 67–89*.
23. Ruiz-García, J. (2012). “Mainshock-Aftershock Ground Motion Features and Their Influence in Building's Seismic Response”, *Journal of Earthquake Engineering, Vol. 16, No. 5, pp. 719–737*.
24. Das, S. and Gupta, V.K. (2010). “Scaling of Response Spectrum and Duration for Aftershocks”, *Soil Dynamics and Earthquake Engineering, Vol. 30, No. 8, pp. 724–735*.
25. Yingnan, Z., Xudong, Z. and Feng, F. (2019). “Study of the Correlations between Main Shocks and Aftershocks and Aftershock Synthesis Method”, *Earthquake Engineering and Engineering Vibration, Vol. 18, No. 4, pp. 759–775*.
26. Nithin, V.L., Das, S. and Kaushik, H.B. (2020). “Stochastic Simulation of Fully Nonstationary Aftershock Ground Motions from Known Preceding Main Shock”, *Soil Dynamics and Earthquake Engineering, Vol. 130, Paper 106006*.

27. Zhai, C.-H., Wen, W.-P., Chen, Z., Li, S. and Xie, L.-L. (2013). “Damage Spectra for the Mainshock–Aftershock Sequence-Type Ground Motions”, *Soil Dynamics and Earthquake Engineering, Vol. 45, pp. 1–12*.
28. Song, R., Li, Y. and Lindt, J. (2014). “Loss Estimation of a Code-Conforming Steel Building to Mainshock-Aftershock Sequences”, *Proceedings of the 10th U.S. National Conference on Earthquake Engineering 2014 (10NCEE), Anchorage, U.S.A., pp. 8242–8252*.
29. Tesfamariam, S., Goda, K. and Mondal, G. (2015). “Seismic Vulnerability of Reinforced Concrete Frame with Unreinforced Masonry Infill due to Main Shock-Aftershock Earthquake Sequences”, *Earthquake Spectra, Vol. 31, No. 3, pp. 1427–1449*.
30. Jalayer, F. and Ebrahimian, H. (2017). “Seismic Risk Assessment Considering Cumulative Damage due to Aftershocks”, *Earthquake Engineering & Structural Dynamics, Vol. 46, No. 3, pp. 369–389*.
31. Shin, M. and Kim, B. (2017). “Effects of Frequency Contents of Aftershock Ground Motions on Reinforced Concrete (RC) Bridge Columns”, *Soil Dynamics and Earthquake Engineering, Vol. 97, pp. 48–59*.
32. Rinaldin, G., Amadio, C. and Fragiacomo, M. (2017). “Effects of Seismic Sequences on Structures with Hysteretic or Damped Dissipative Behaviour”, *Soil Dynamics and Earthquake Engineering, Vol. 97, pp. 205–215*.
33. Omranian, E., Abdelnaby, A.E. and Abdollahzadeh, G. (2018). “Seismic Vulnerability Assessment of RC Skew Bridges Subjected to Mainshock-Aftershock Sequences”, *Soil Dynamics and Earthquake Engineering, Vol. 114, pp. 186–197*.
34. Wen, W., Ji, D., Zhai, C., Li, X. and Sun, P. (2018). “Damage Spectra of the Mainshock-Aftershock Ground Motions at Soft Soil Sites”, *Soil Dynamics and Earthquake Engineering, Vol. 115, pp. 815–825*.
35. Shokrabadi, M., Burton, H.V. and Stewart, J.P. (2018). “Impact of Sequential Ground Motion Pairing on Mainshock-Aftershock Structural Response and Collapse Performance Assessment”, *Journal of Structural Engineering, ASCE, Vol. 144, No. 10, Paper 04018177*.
36. Trapani, F.D. and Malavisi, M. (2019). “Seismic Fragility Assessment of Infilled Frames Subject to Mainshock/Aftershock Sequences Using a Double Incremental Dynamic Analysis Approach”, *Bulletin of Earthquake Engineering, Vol. 17, pp. 211–235*.
37. Shafaei, H. and Naderpour, H. (2020). “Seismic Fragility Evaluation of FRP-Retrofitted RC Frames Subjected to Mainshock-Aftershock Records”, *Structures, Vol. 27, pp. 950–961*.
38. Wen, W., Ji, D. and Zhai, C. (2020). “Cumulative Damage of Structures under the Mainshock-Aftershock Sequences in the Near-Fault Region”, *Journal of Earthquake Engineering, Vol. 26, No. 4, pp. 2088–2102*.
39. Iervolino, I., Chioccarelli, E. and Suzuki, A. (2020). “Seismic Damage Accumulation in Multiple Mainshock-Aftershock Sequences”, *Earthquake Engineering & Structural Dynamics, Vol. 49, No. 10, pp. 1007–1027*.
40. Qiao, Y.-M., Lu, D.-G. and Yu, X.-H. (2020). “Shaking Table Tests of a Reinforced Concrete Frame Subjected to Mainshock-Aftershock Sequences”, *Journal of Earthquake Engineering, Vol. 26, No. 4, pp. 1693–1722*.
41. Abdelnaby, A.E. (2018). “Fragility Curves for RC Frames Subjected to Tohoku Mainshock-Aftershocks Sequences”, *Journal of Earthquake Engineering, Vol. 22, No. 5, pp. 902–920*.
42. Das, S. and Gupta, V.K. (2008). “Wavelet-Based Simulation of Spectrum-Compatible Aftershock Accelerograms”, *Earthquake Engineering & Structural Dynamics, Vol. 37, No. 11, pp. 1333–1348*.
43. Trifunac, M.D. and Brady, A.G. (1975). “A Study on the Duration of Strong Earthquake Ground Motion”, *Bulletin of the Seismological Society of America, Vol. 65, No. 3, pp. 581–626*.
44. Papadopoulos, A.N., Kohrangi, M. and Bazzurro, P. (2020). “Mainshock-Consistent Ground Motion Record Selection for Aftershock Sequences”, *Earthquake Engineering & Structural Dynamics, Vol. 49, No. 8, pp. 754–771*.
45. Papadopoulos, A.N., Kohrangi, M. and Bazzurro, P. (2019). “Correlation of Spectral Acceleration Values of Mainshock-Aftershock Ground Motion Pairs”, *Earthquake Spectra, Vol. 35, No. 1, pp. 39–60*.

46. Hu, S., Gardoni, P. and Xu, L. (2018). “Stochastic Procedure for the Simulation of Synthetic Main Shock-Aftershock Ground Motion Sequences”, *Earthquake Engineering & Structural Dynamics, Vol. 47, No. 11, pp. 2275–2296.*
47. Mukhopadhyay, S., Das, S. and Gupta, V.K. (2019). “Wavelet-Based Generation of Accelerogram-Consistent, Spectrum-Compatible Motions: New Algorithms and Short-Period Overestimation”, *Soil Dynamics and Earthquake Engineering, Vol. 121, pp. 327–340*.
48. Mukherjee, S. and Gupta, V.K. (2022). “Wavelet-Based Generation of Spectrum-Compatible Time-Histories”, *Soil Dynamics and Earthquake Engineering, Vol. 22, No. 9–12, pp. 799–804*.
49. BHRC (2004). “Catalogue of Earthquake Strong Ground Motion Records”, *Report R-466, Building and Housing Research Center, Tehran, Iran*.
50. BIS (2000). “IS 456: 2000—Plain and Reinforced Concrete—Code of Practice (Fourth Revision)”, *Indian Standard, Bureau of Indian Standards, New Delhi*.
51. BIS (2016). “IS 1893 (Part 1): 2016—Criteria for Earthquake Resistant Design of Structures: Part 1 General Provisions and Buildings (Sixth Revision)”, *Indian Standard, Bureau of Indian Standards, New Delhi*.
52. BIS (1993). “IS 13920: 1993—Ductile Detailing of Reinforced Concrete Structures Subjected to Seismic Forces—Code of Practice”, *Indian Standard, Bureau of Indian Standards, New Delhi*.
53. Mazzoni, S., McKenna, F., Scott, M.H., Fenves, G.L., et al. (2005). “OpenSees Command Language Manual”, *Pacific Earthquake Engineering Research Center, University of California, Berkeley, U.S.A.*
54. Scott, M.H. and Fenves, G.L. (2006). “Plastic Hinge Integration Methods for Force-Based Beam-Column Elements”, *Journal of Structural Engineering, ASCE, Vol. 132, No. 2, pp. 244–252*.
55. Paulay, T. and Priestley, M.J.N. (1992). “Seismic Design of Reinforced Concrete and Masonry Buildings”, *John Wiley & Sons, New York, U.S.A.*
56. BIS (2016). “IS 13920: 2016—Ductile Design and Detailing of Reinforced Concrete Structures Subjected to Seismic Forces—Code of Practice (First Revision)”, *Indian Standard, Bureau of Indian Standards, New Delhi*.
57. NZS (2006). “NZS 3101: Part 1: 2006—Concrete Structures Standard, Part 1—The Design of Concrete Structures”, *New Zealand Standard, Standards New Zealand, Wellington, New Zealand.*
58. BSI (2004). “BS EN 1998-1:2004—Eurocode 8: Design of Structures for Earthquake Resistance, Part 1: General Rules, Seismic Actions and Rules for Buildings”, *British Standards Institution, London, U.K.*
59. ACI (2014). “Building Code Requirements for Structural Concrete (ACI 318-14) and Commentary (ACI 318R-14)”, *ACI Standard, American Concrete Institute, Farmington Hills, U.S.A.*
60. Elenas, A. (2000). “Correlation between Seismic Acceleration Parameters and Overall Structural Damage Indices of Buildings”, *Soil Dynamics and Earthquake Engineering, Vol. 20, No. 1–4, pp. 93–100*.
61. Cosenza, E., Manfredi, G. and Ramasco, R. (1993). “The Use of Damage Functionals in Earthquake Engineering”, *Earthquake Engineering & Structural Dynamics, Vol. 22, No. 10, pp. 855–868*.
62. van de Lindt, J.W. and Goh, G. (2004). “Earthquake Duration Effect on Structural Reliability”, *Journal of Structural Engineering, ASCE, Vol. 130, No. 5, pp. 821–826*.
63. Williams, M.S. and Sexsmith, R.G. (1997). “Seismic Assessment of Concrete Bridges Using Inelastic Damage Analysis”, *Engineering Structures, Vol. 19, No. 3, pp. 208–216*.
64. Zhai, C.-H., Wen, W.-P., Li, S., Chen, Z.Q., Chang, Z. and Xie, L.-L. (2014). “The Damage Investigation of Inelastic SDOF Structure under the Mainshock-Aftershock Sequence-Type Ground Motions”, *Soil Dynamics and Earthquake Engineering, Vol. 59, pp. 30–41*.

Main shock | Aftershock

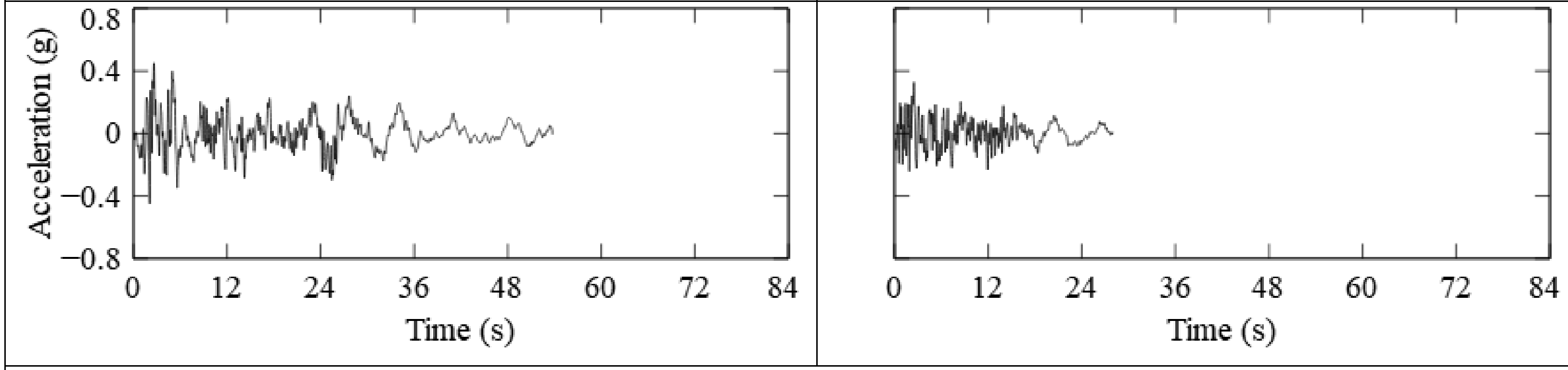

Fig. S1 Scaled Sequence Considered for Sl. No. 1 in Table A1

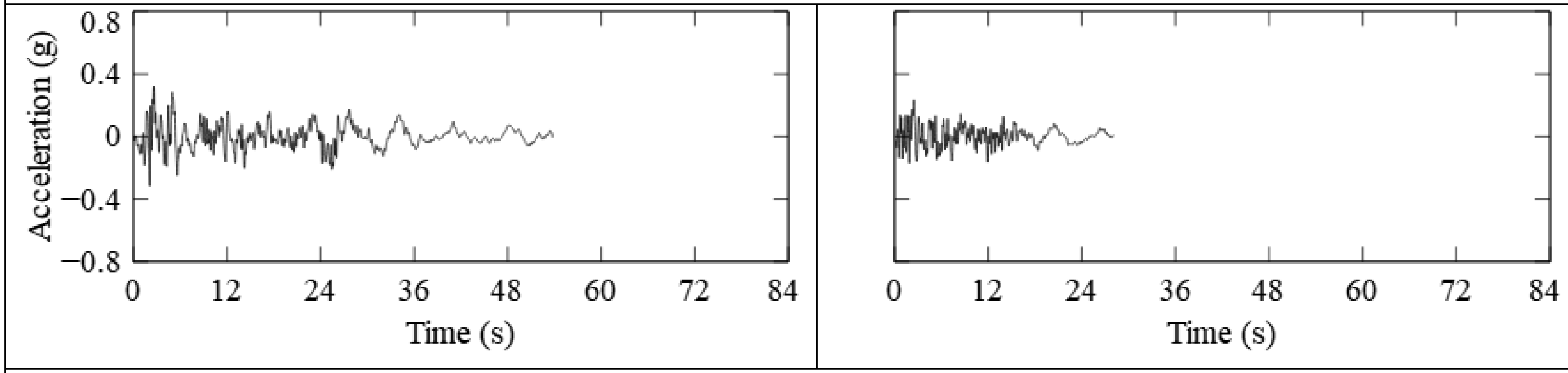

Fig. S2 Scaled Sequence Considered for Sl. No. 2 in Table A1

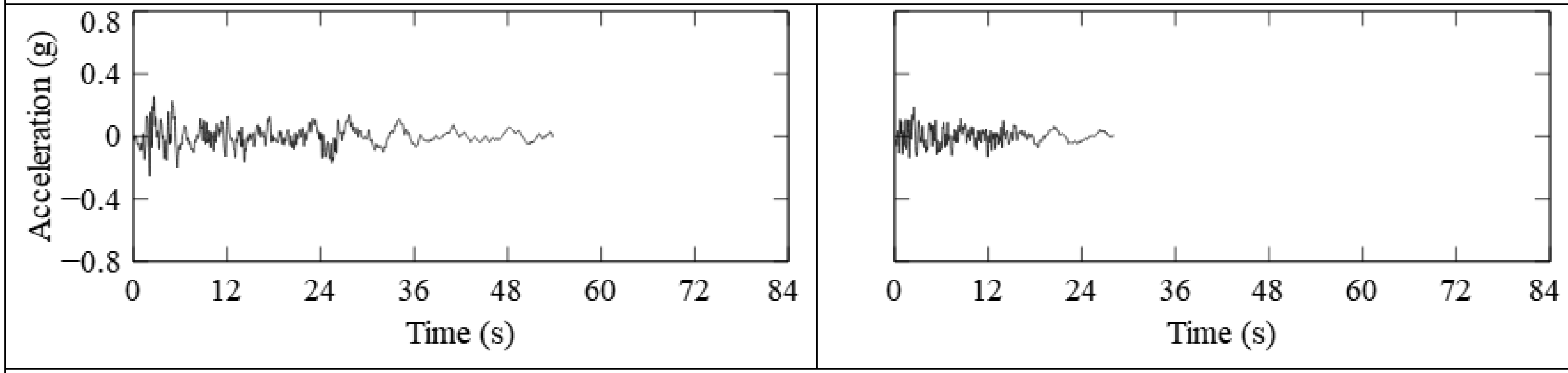

Fig. S3 Scaled Sequence Considered for Sl. No. 3 in Table A1

Main shock | Aftershock

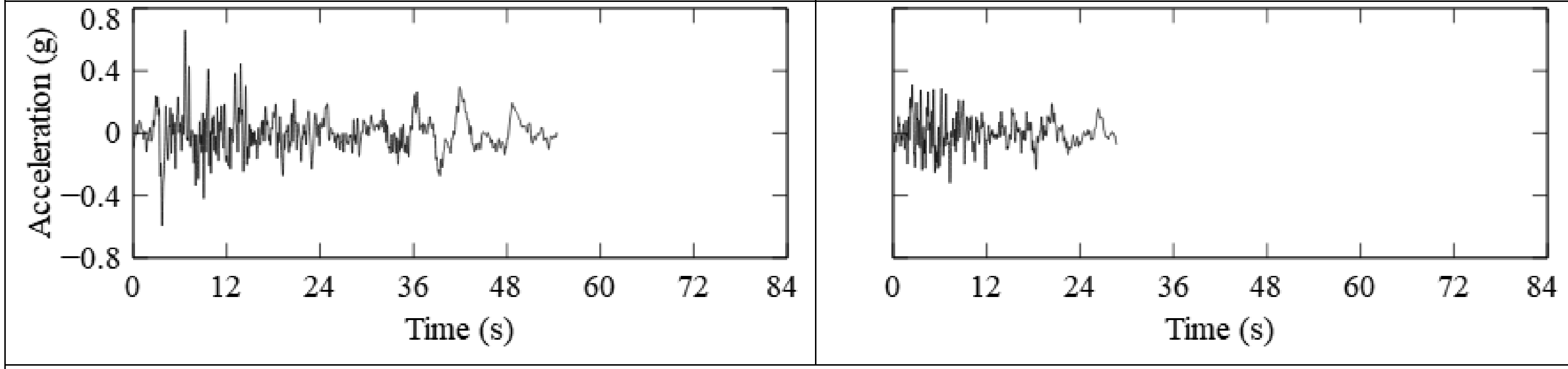

Fig. S4 Scaled Sequence Considered for Sl. No. 4 in Table A1

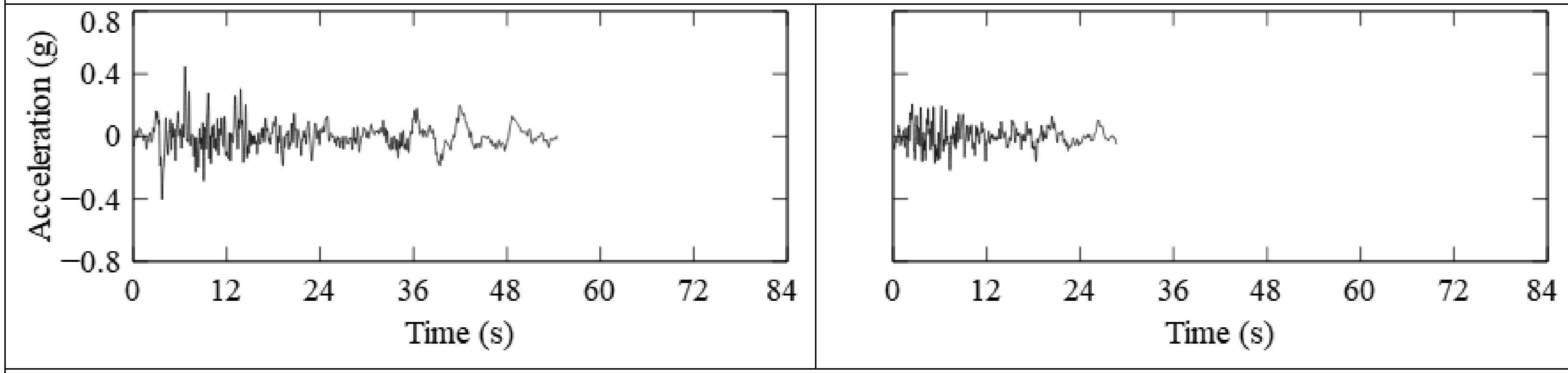

Fig. S5 Scaled Sequence Considered for Sl. No. 5 in Table A1

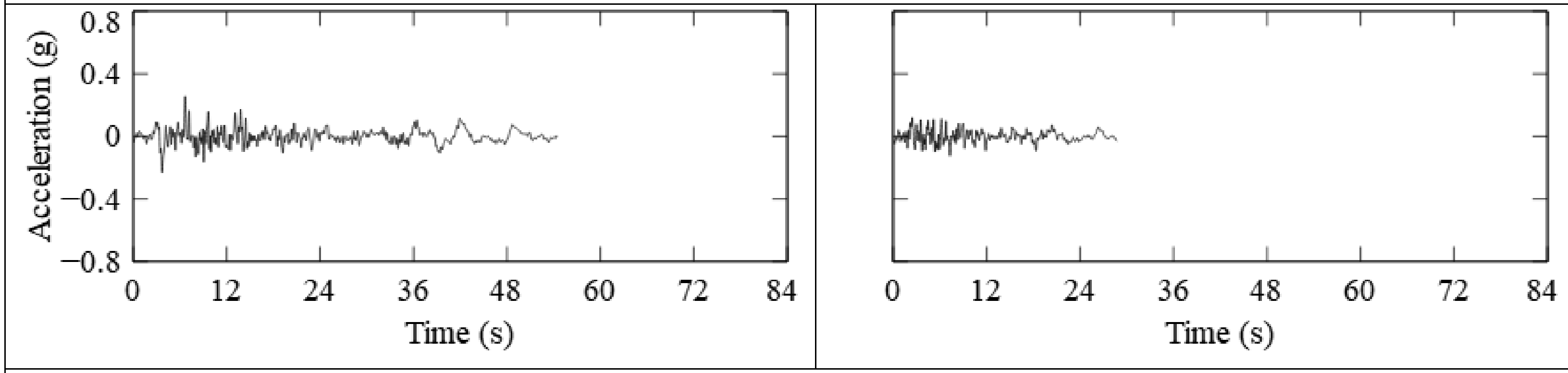

Fig. S6 Scaled Sequence Considered for Sl. No. 6 in Table A1

Main shock	Aftershock

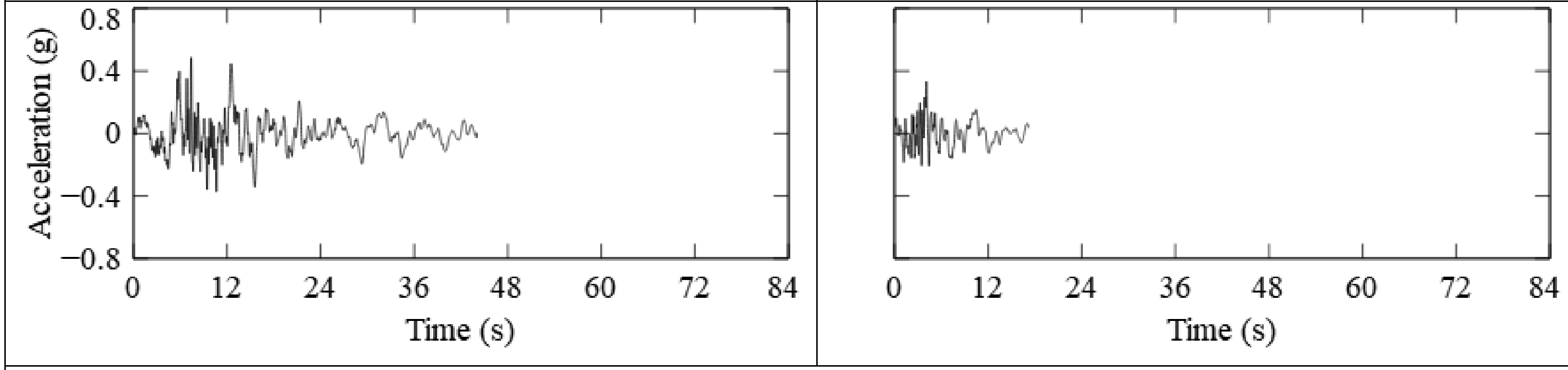

Fig. S7 Scaled Sequences Considered for Sl. Nos. 7, 85 and 97 in Table A1

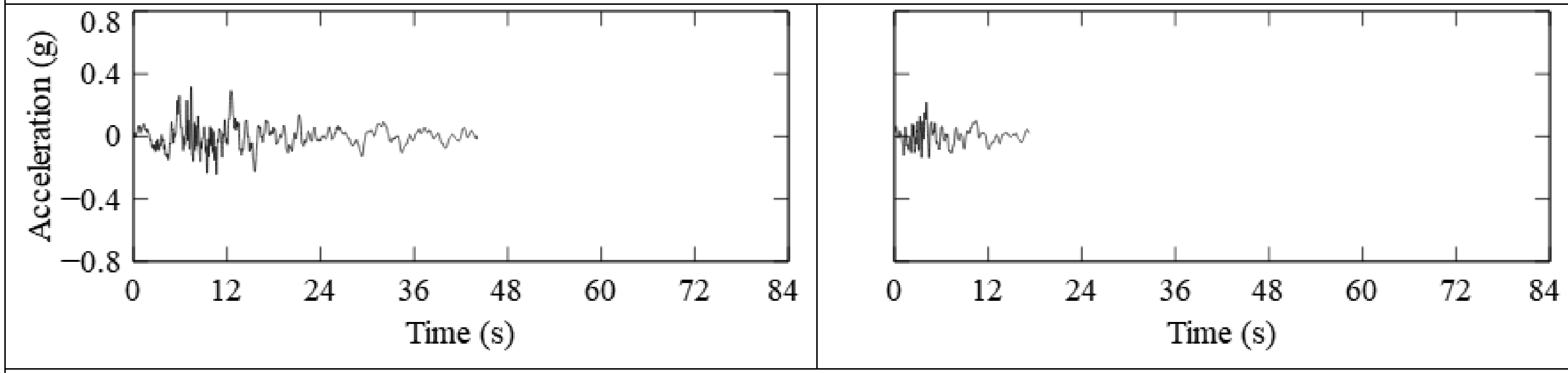

Fig. S8 Scaled Sequences Considered for Sl. Nos. 8, 86 and 98 in Table A1

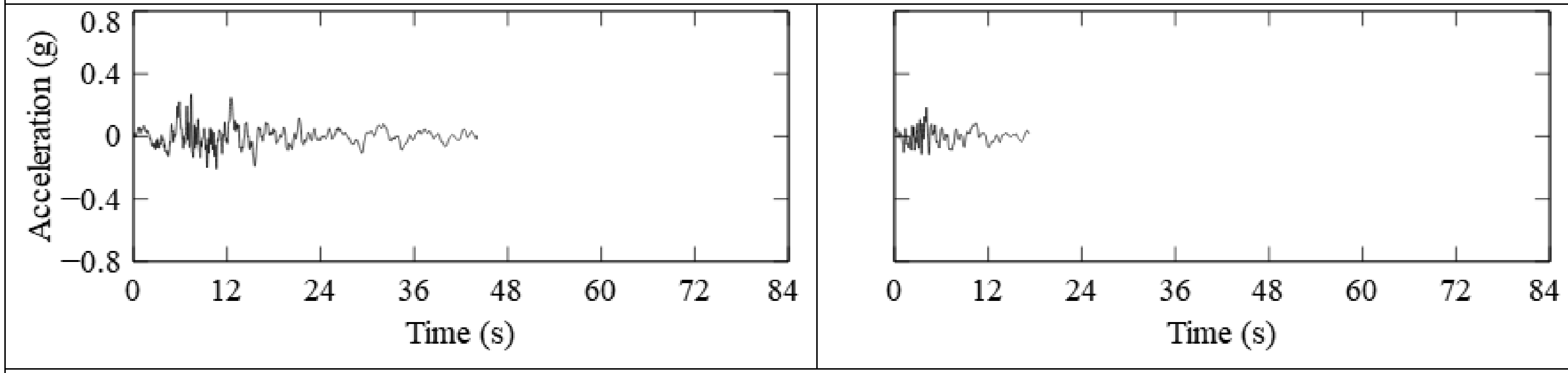

Fig. S9 Scaled Sequences Considered for Sl. Nos. 9, 87 and 99 in Table A1

Main shock

Aftershock

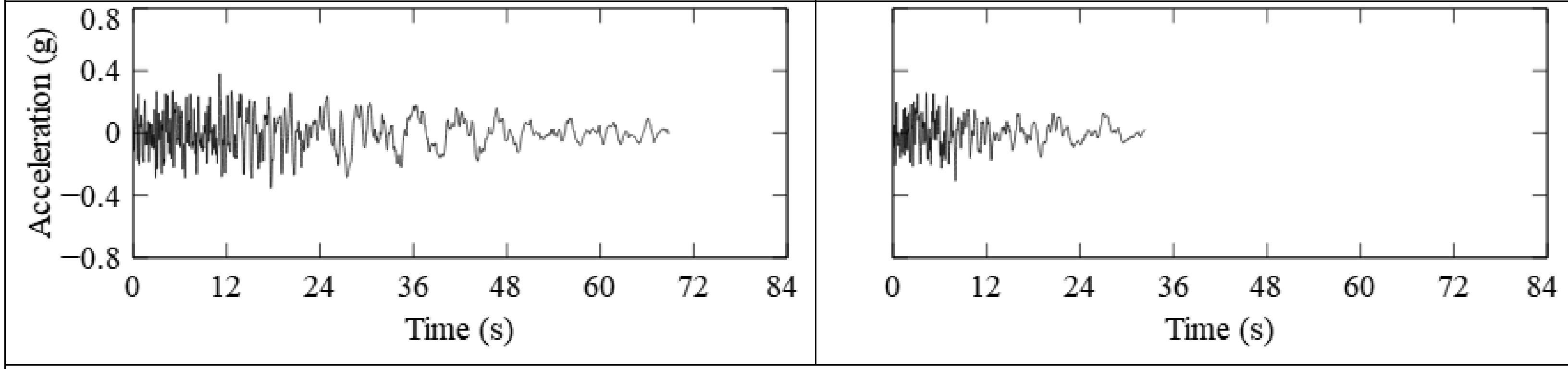

Fig. S10 Scaled Sequence Considered for Sl. No. 10 in Table A1

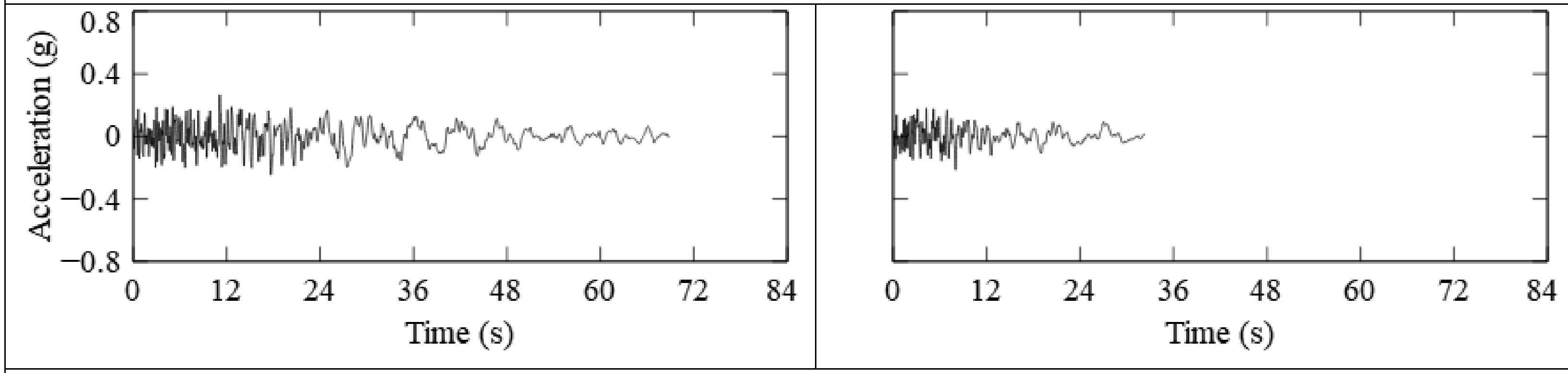

Fig. S11 Scaled Sequence Considered for Sl. No. 11 in Table A1

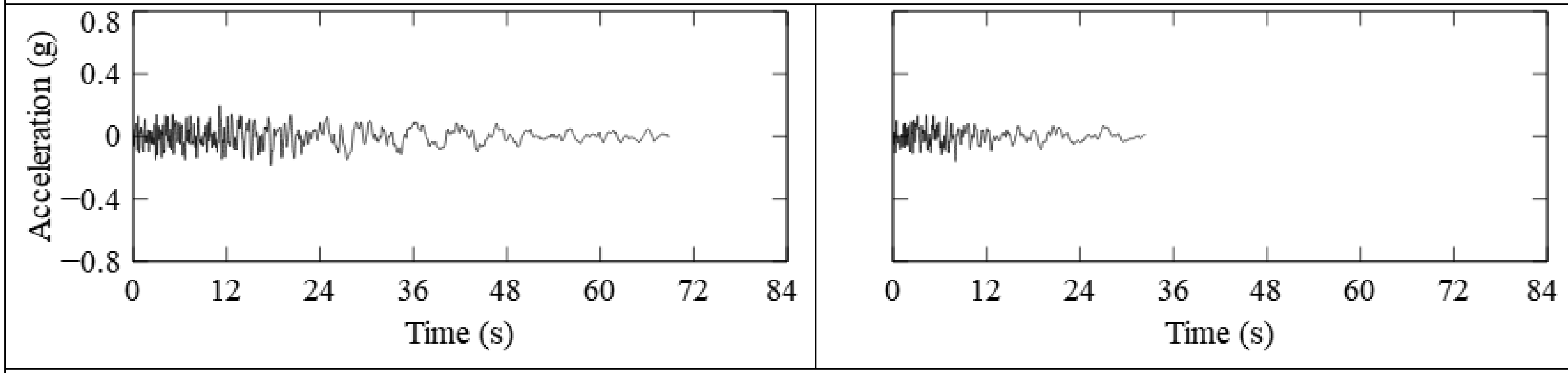

Fig. S12 Scaled Sequence Considered for Sl. No. 12 in Table A1

Main shock	Aftershock

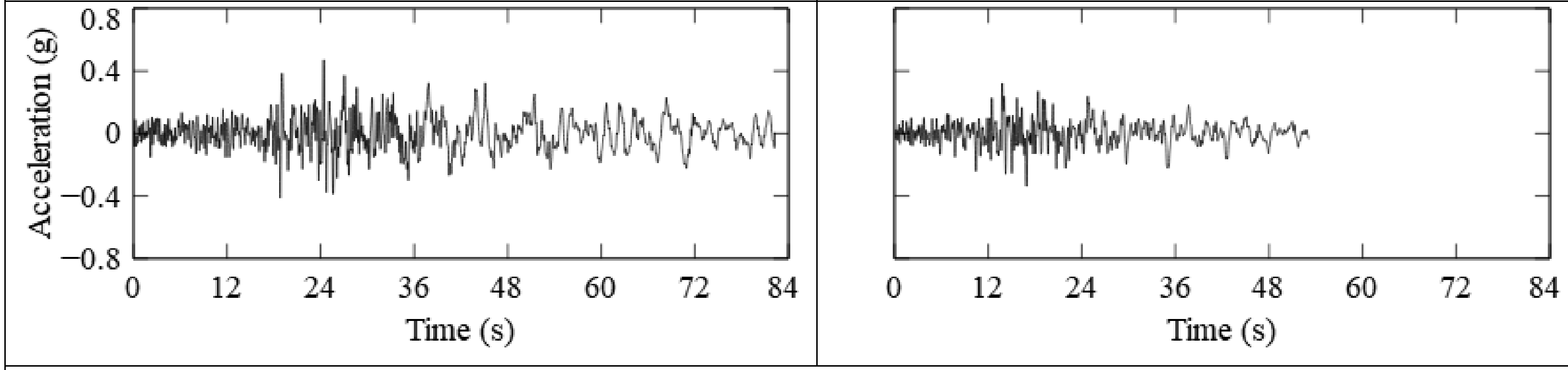

Fig. S13 Scaled Sequences Considered for Sl. Nos. 13 and 25 in Table A1

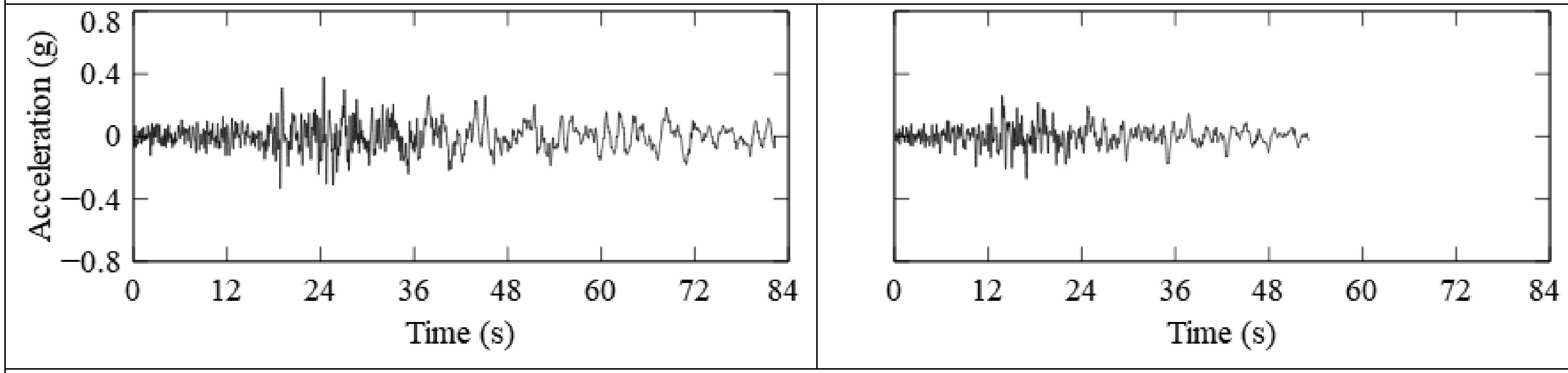

Fig. S14 Scaled Sequences Considered for Sl. Nos. 14 and 26 in Table A1

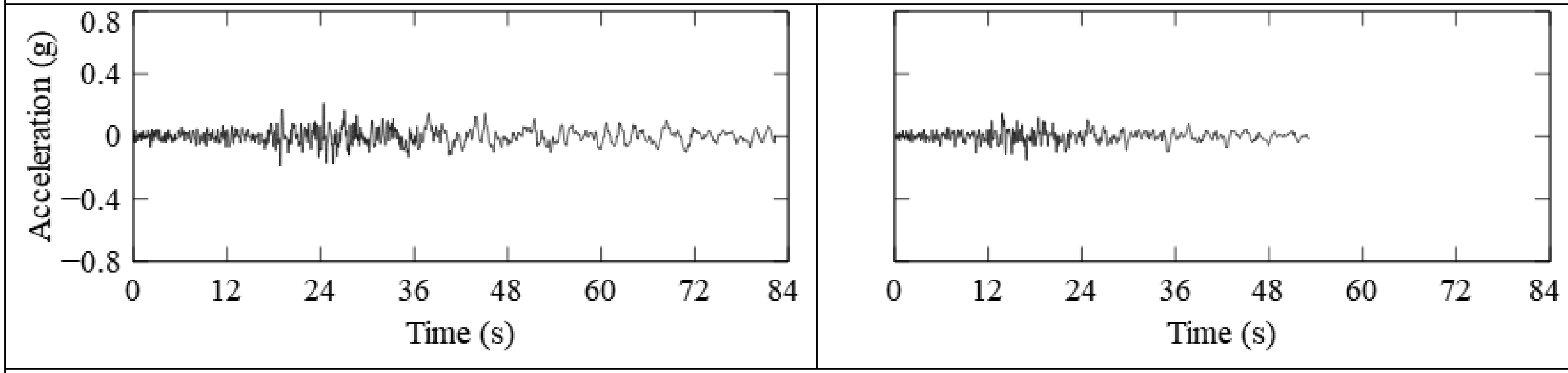

Fig. S15 Scaled Sequences Considered for Sl. Nos. 15 and 27 in Table A1

Main shock

Aftershock

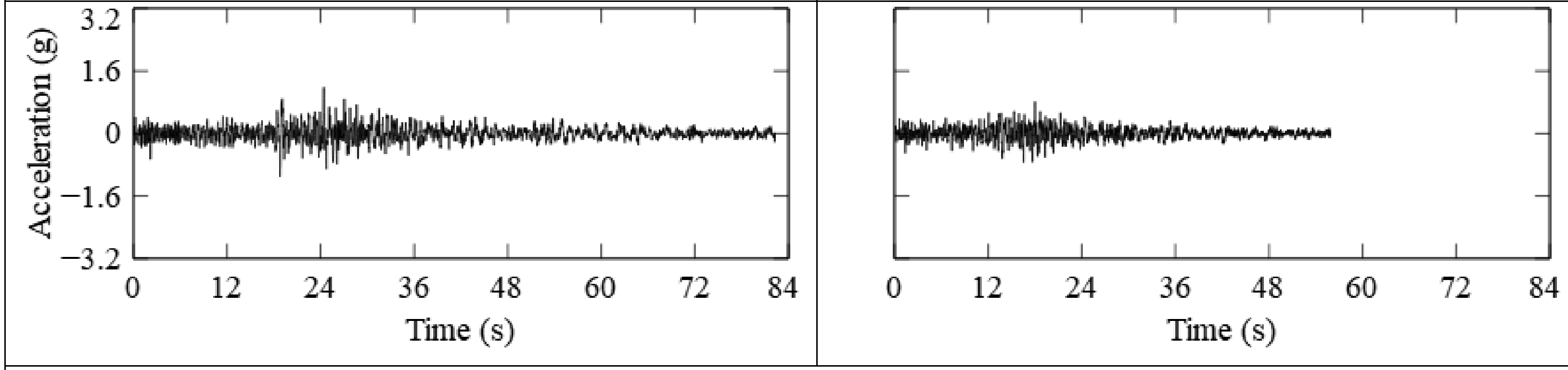

Fig. S16 Scaled Sequence Considered for Sl. No. 16 in Table A1

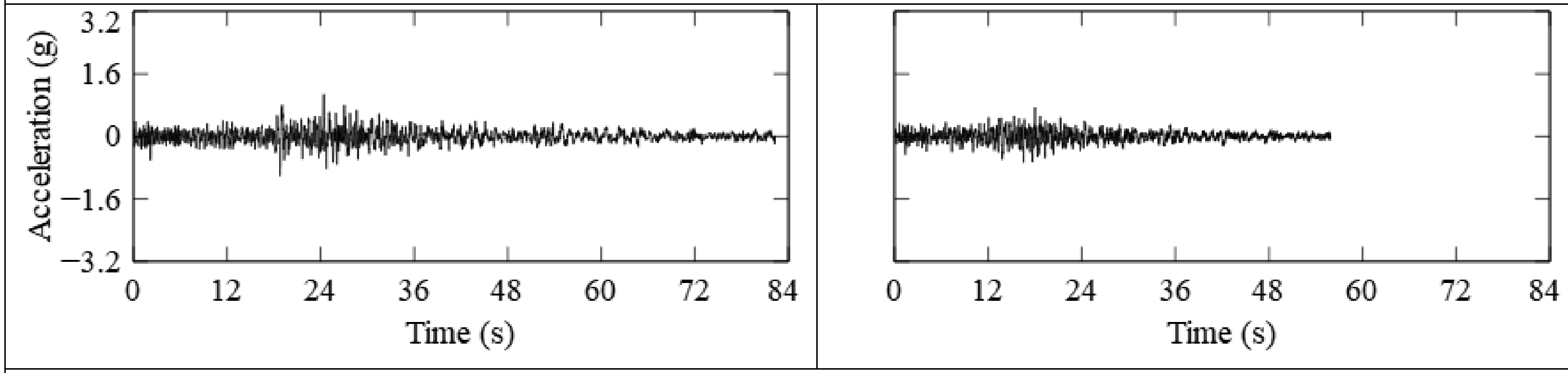

Fig. S17 Scaled Sequence Considered for Sl. No. 17 in Table A1

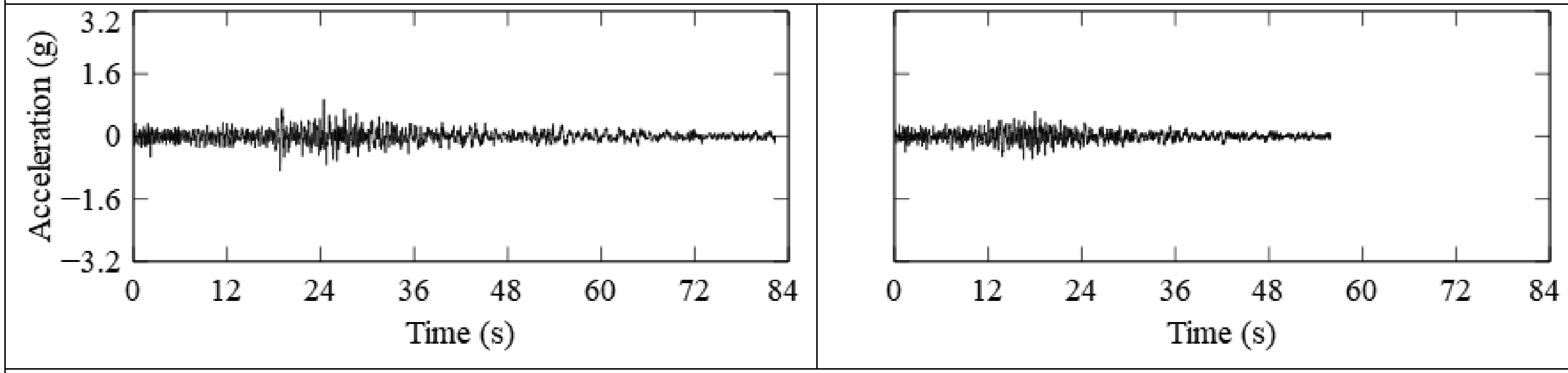

Fig. S18 Scaled Sequence Considered for Sl. No. 18 in Table A1

Main shock | Aftershock

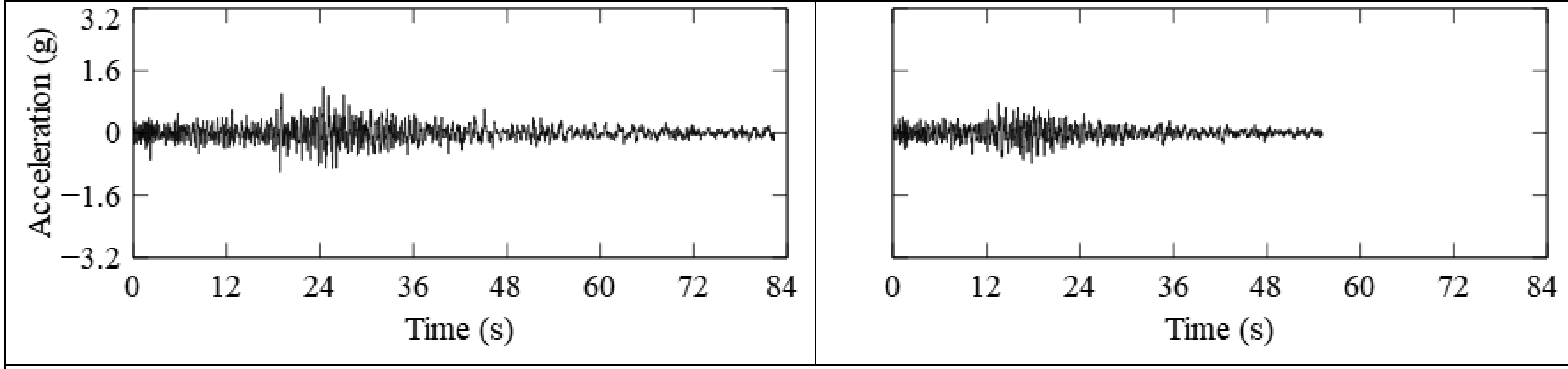

Fig. S19 Scaled Sequence Considered for Sl. No. 19 in Table A1

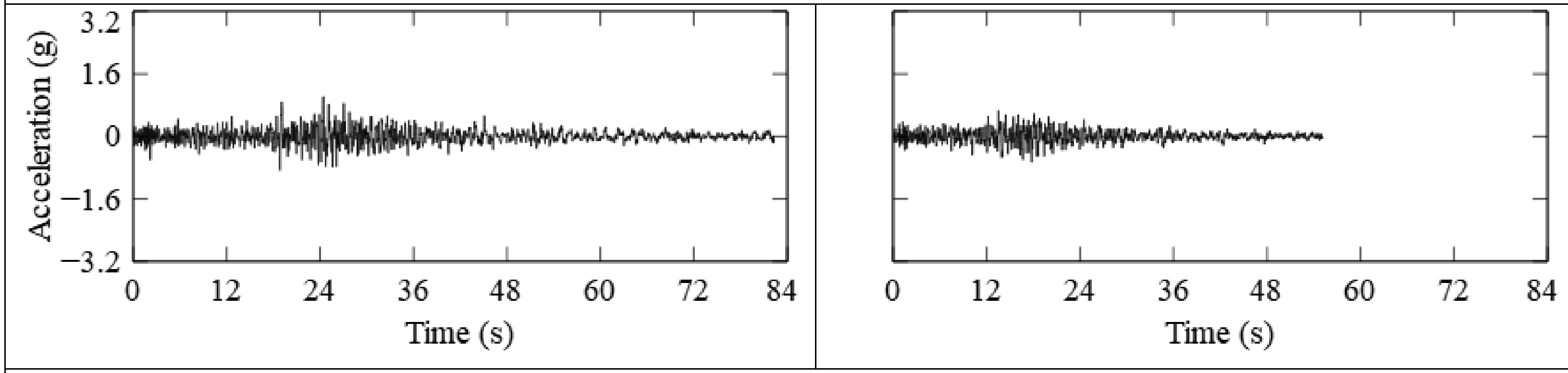

Fig. S20 Scaled Sequence Considered for Sl. No. 20 in Table A1

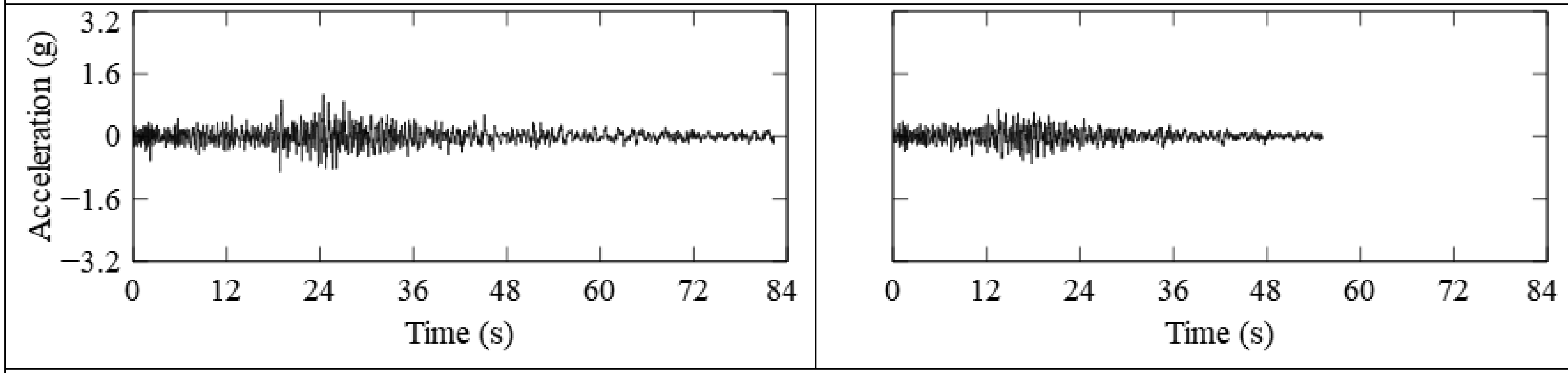

Fig. S21 Scaled Sequence Considered for Sl. No. 21 in Table A1

<table>
<tr><th>Main shock</th><th>Aftershock</th></tr>
<tr><td>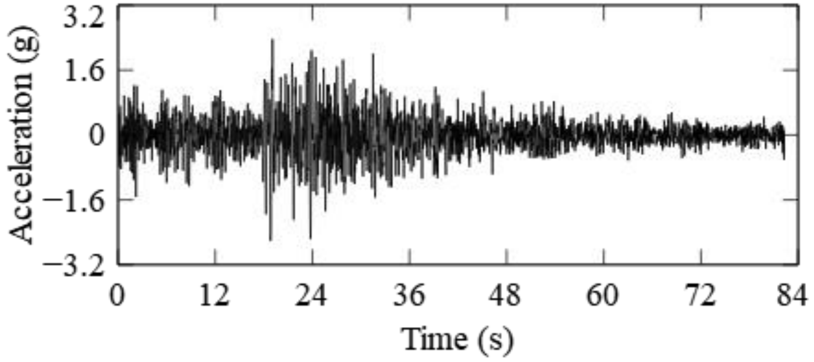
</td><td>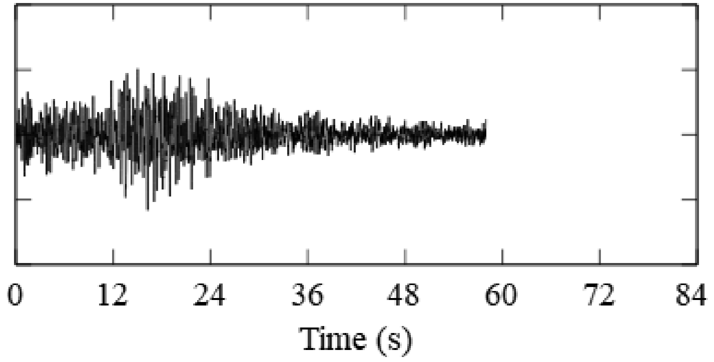
</td></tr>
<tr><td colspan="2">Fig. S22 Scaled Sequences Considered for Sl. Nos. 22, 76, 91 in Table A1, and Sl. No. 4 in Table A2</td></tr>
<tr><td>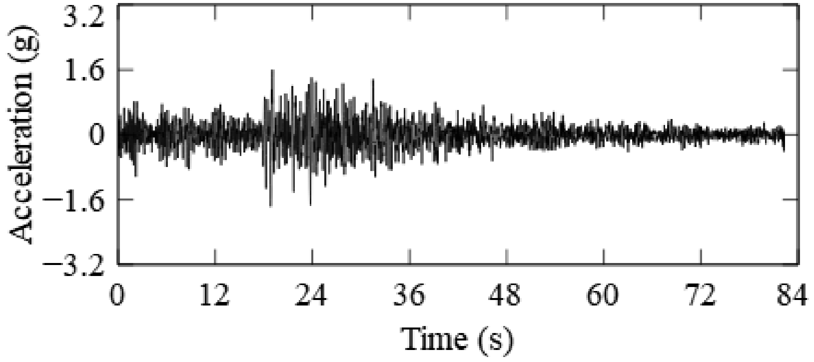
</td><td>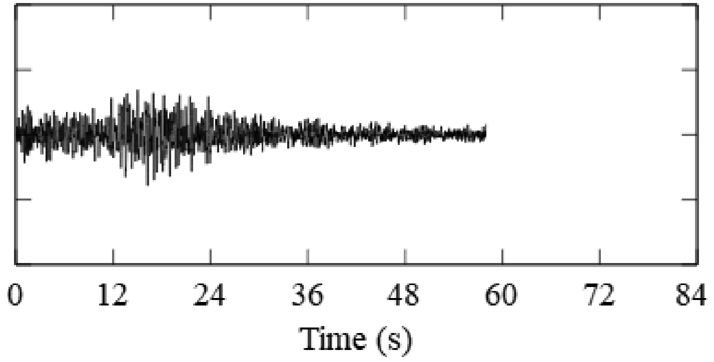
</td></tr>
<tr><td colspan="2">Fig. S23 Scaled Sequences Considered for Sl. Nos. 23, 77, 92 in Table A1, and Sl. No. 5 in Table A2</td></tr>
<tr><td>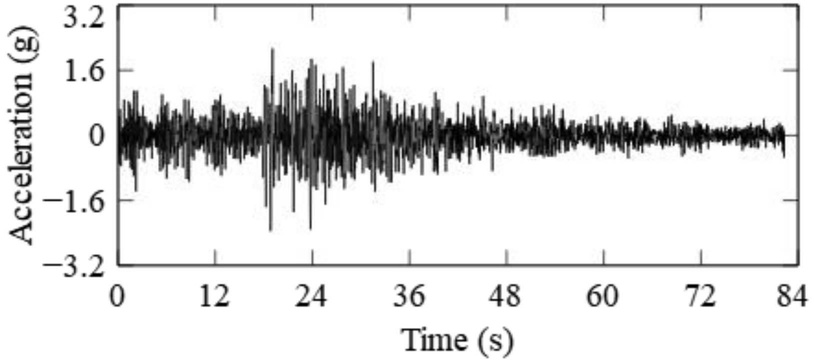
</td><td>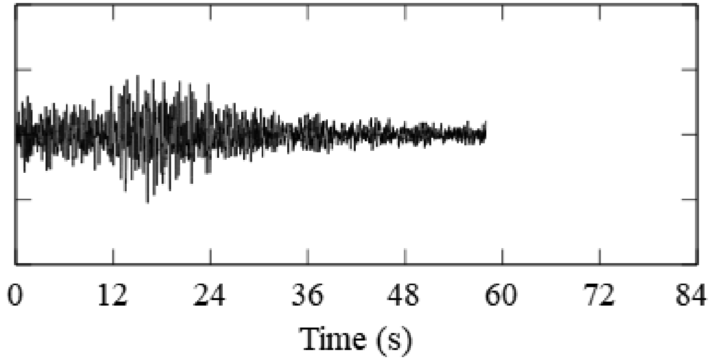
</td></tr>
<tr><td colspan="2">Fig. S24 Scaled Sequences Considered for Sl. Nos. 24, 78, 93 in Table A1, and Sl. No. 6 in Table A2</td></tr>
</table>

Main shock	Aftershock

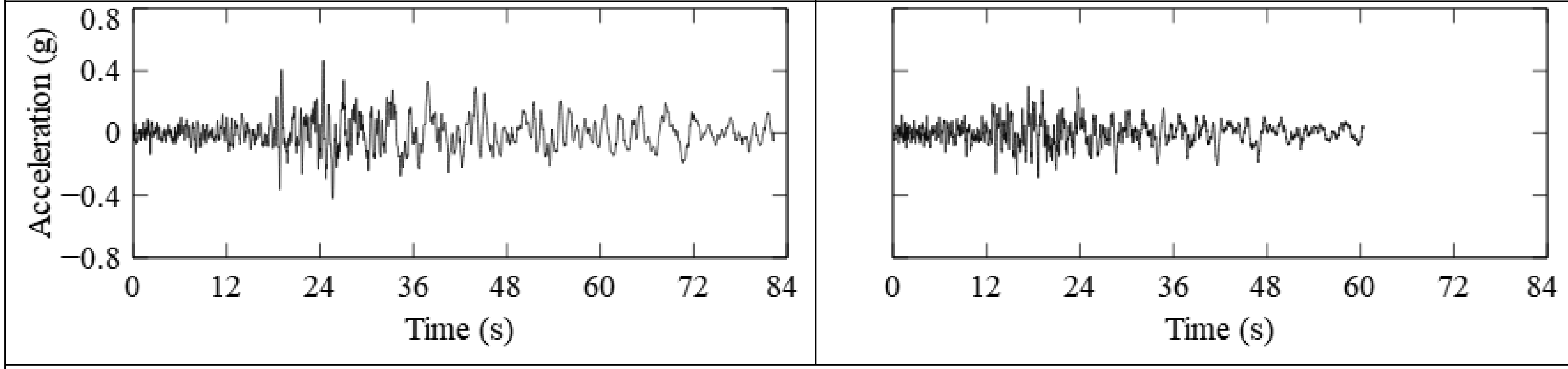

Fig. S25 Scaled Sequence Considered for Sl. No. 28 in Table A1

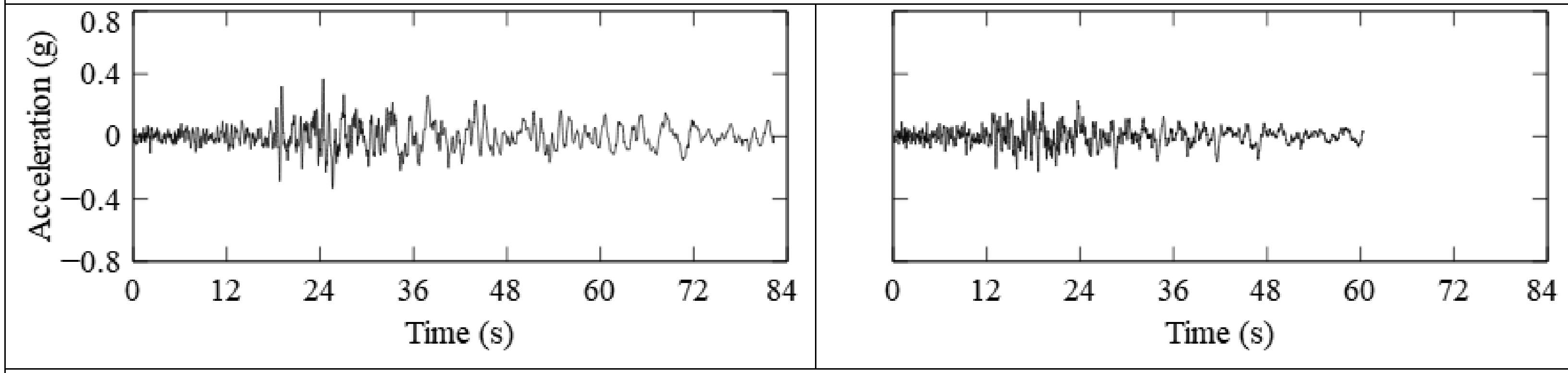

Fig. S26 Scaled Sequence Considered for Sl. No. 29 in Table A1

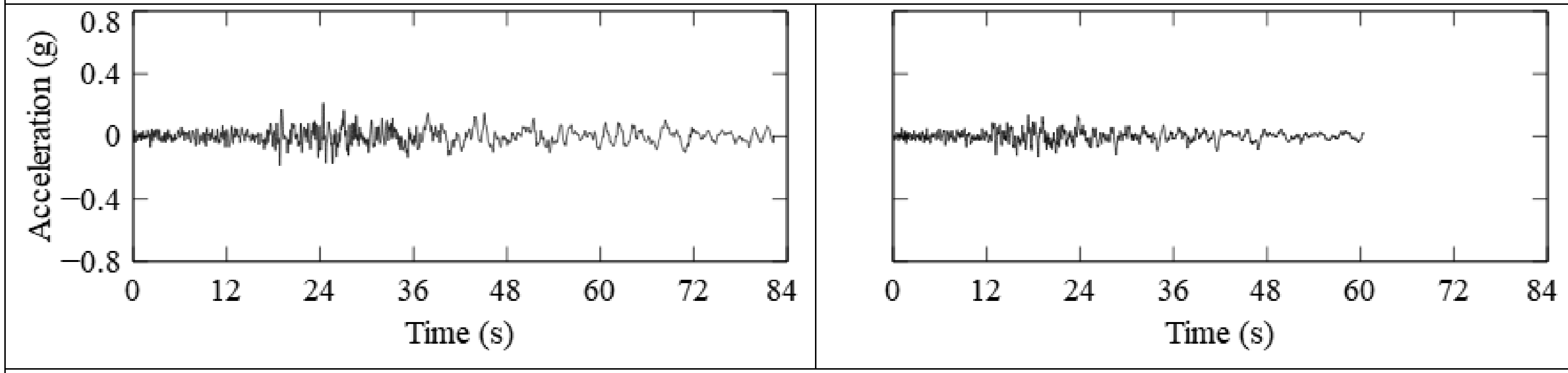

Fig. S27 Scaled Sequence Considered for Sl. No. 30 in Table A1

<table>
<tr><th>Main shock</th><th>Aftershock</th></tr>
<tr><td>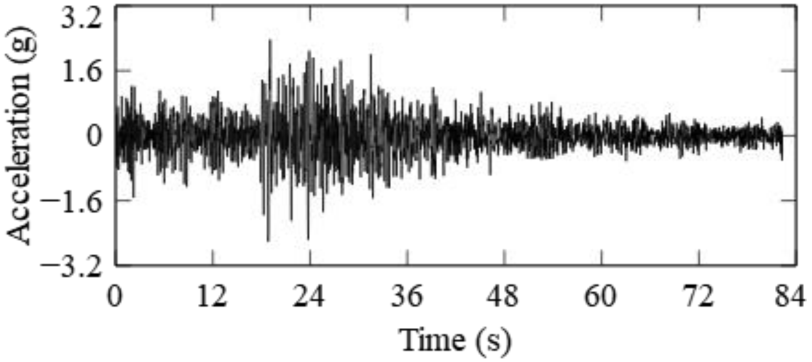
</td><td>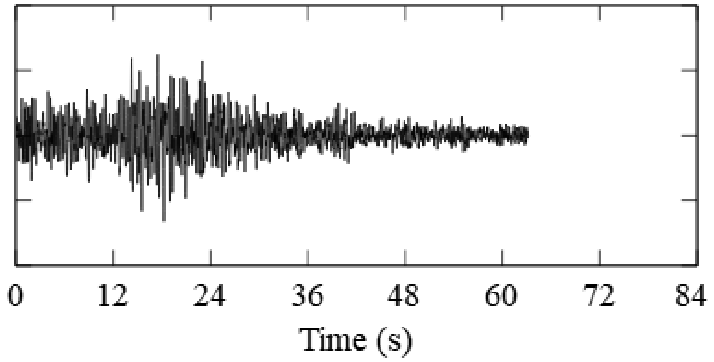
</td></tr>
<tr><td colspan="2">Fig. S28 Scaled Sequence Considered for Sl. No. 31 in Table A1</td></tr>
<tr><td>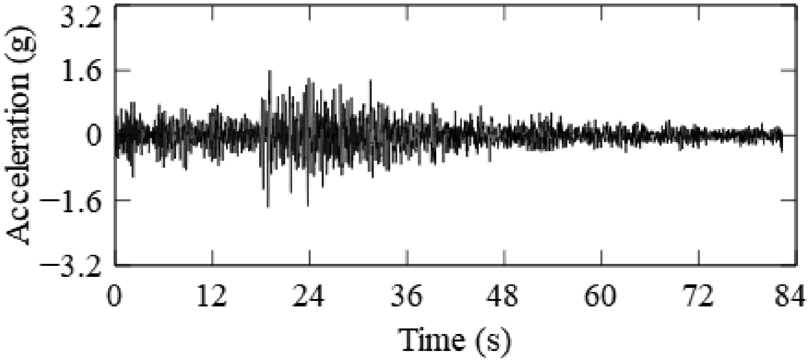
</td><td>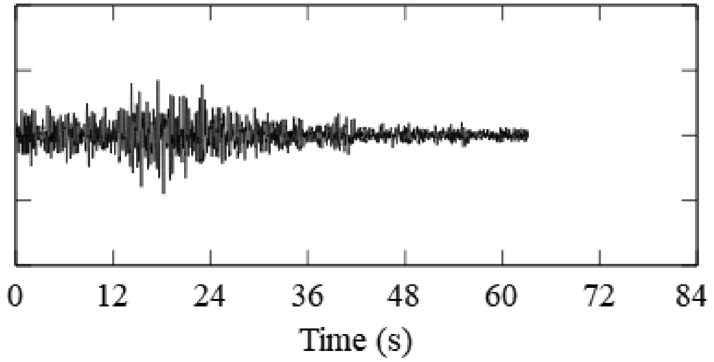
</td></tr>
<tr><td colspan="2">Fig. S29 Scaled Sequence Considered for Sl. No. 32 in Table A1</td></tr>
<tr><td>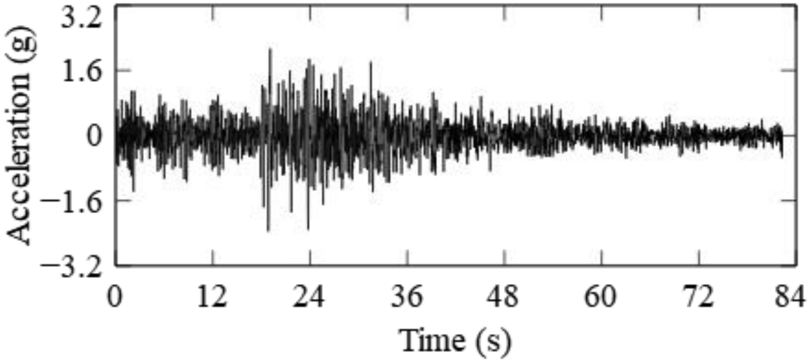
</td><td>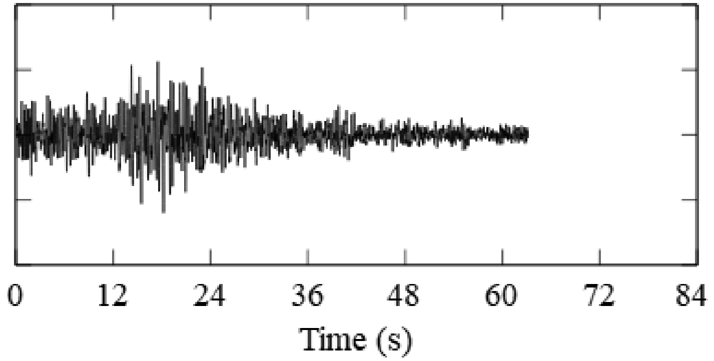
</td></tr>
<tr><td colspan="2">Fig. S30 Scaled Sequence Considered for Sl. No. 33 in Table A1</td></tr>
</table>

<table>
<tr><th>Main shock</th><th>Aftershock</th></tr>
<tr><td>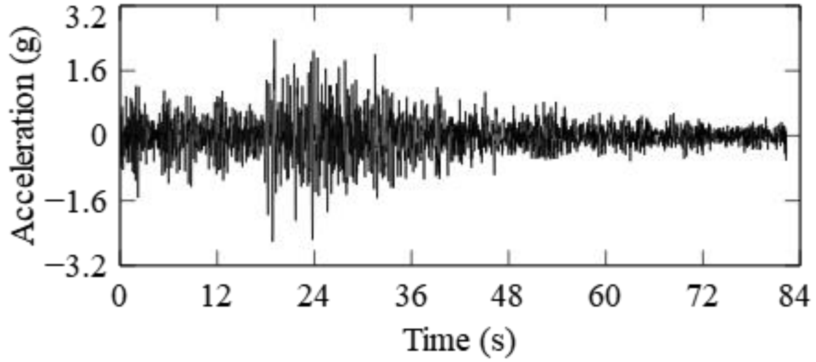
</td><td>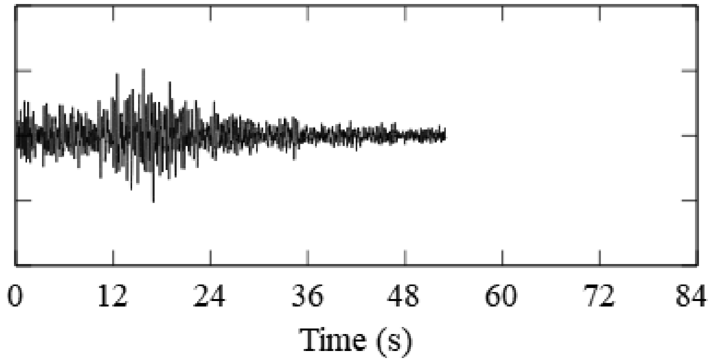
</td></tr>
<tr><td colspan="2">Fig. S31 Scaled Sequence Considered for Sl. No. 34 in Table A1</td></tr>
<tr><td>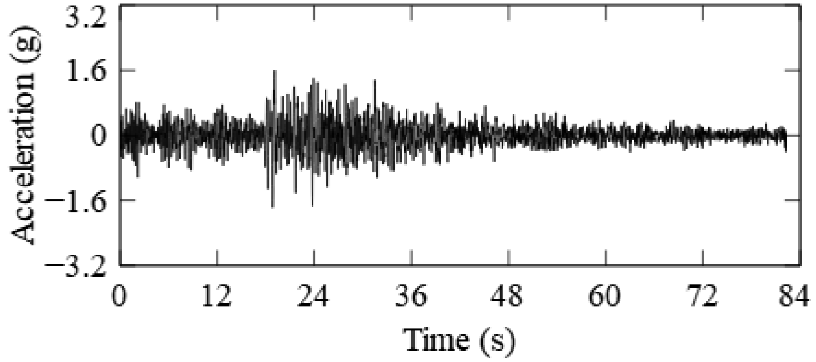
</td><td>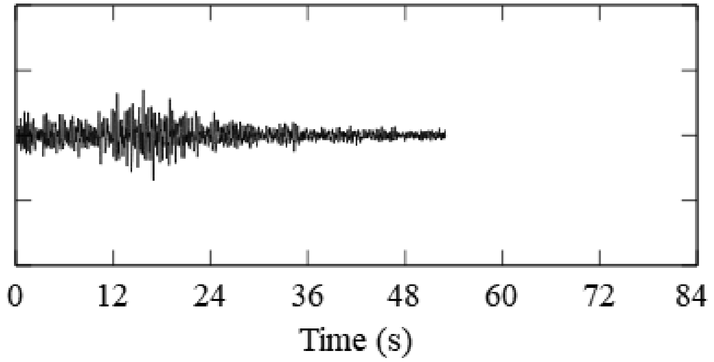
</td></tr>
<tr><td colspan="2">Fig. S32 Scaled Sequence Considered for Sl. No. 35 in Table A1</td></tr>
<tr><td>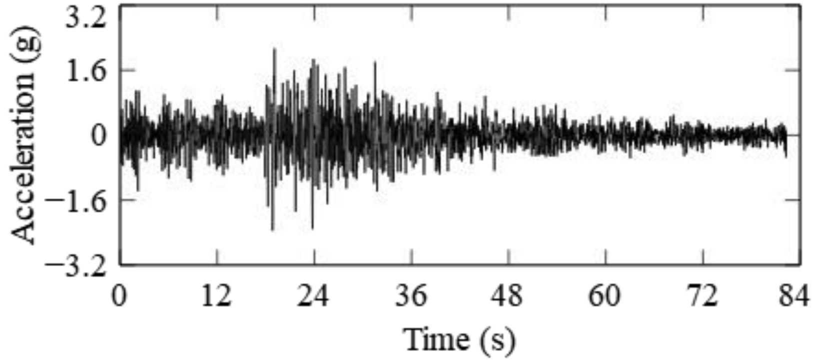
</td><td>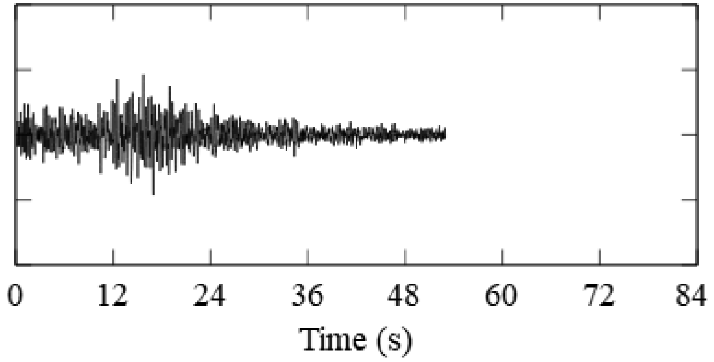
</td></tr>
<tr><td colspan="2">Fig. S33 Scaled Sequence Considered for Sl. No. 36 in Table A1</td></tr>
</table>

Main shock	Aftershock

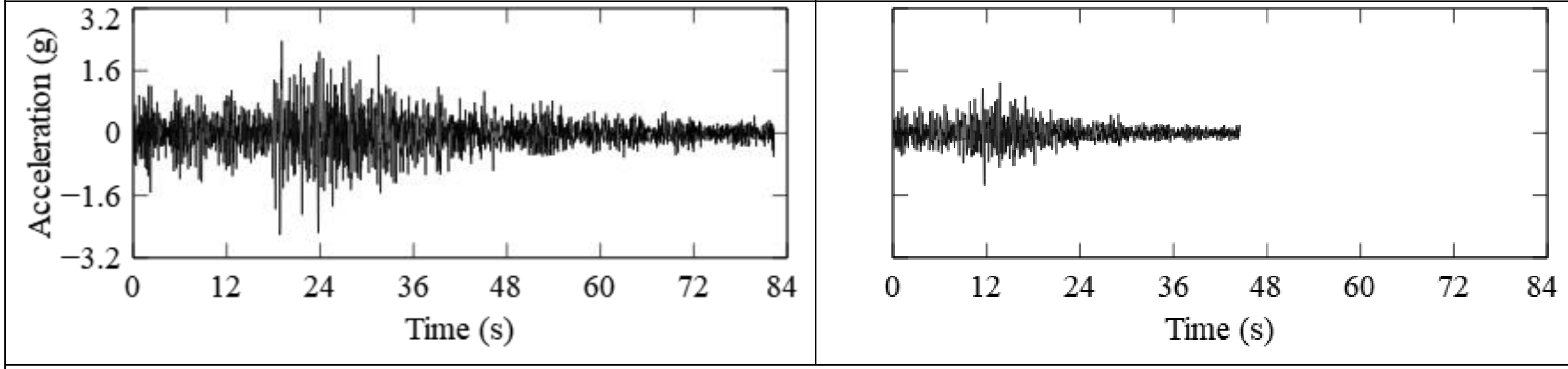

Fig. S34 Scaled Sequence Considered for Sl. No. 37 in Table A1

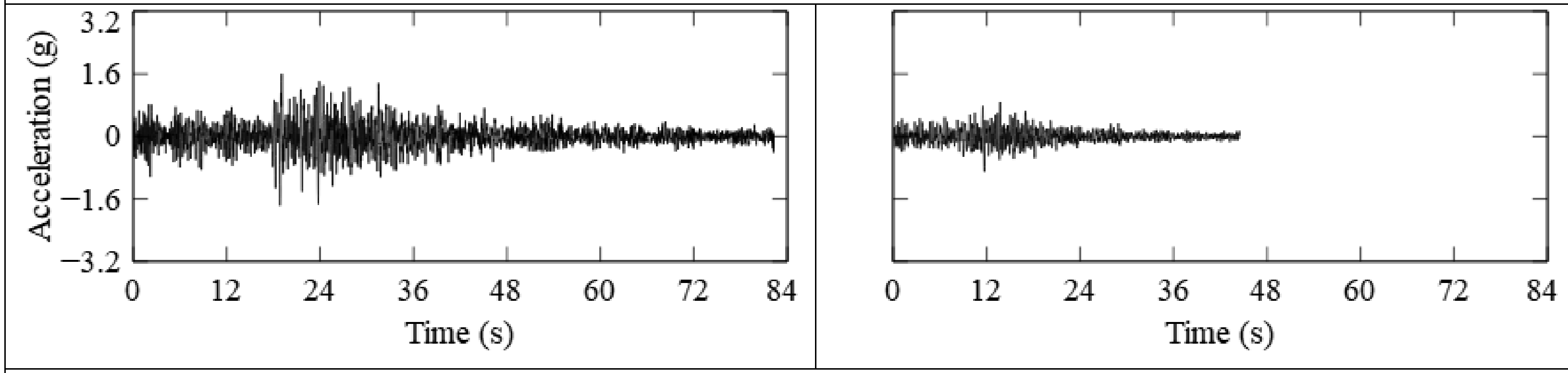

Fig. S35 Scaled Sequence Considered for Sl. No. 38 in Table A1

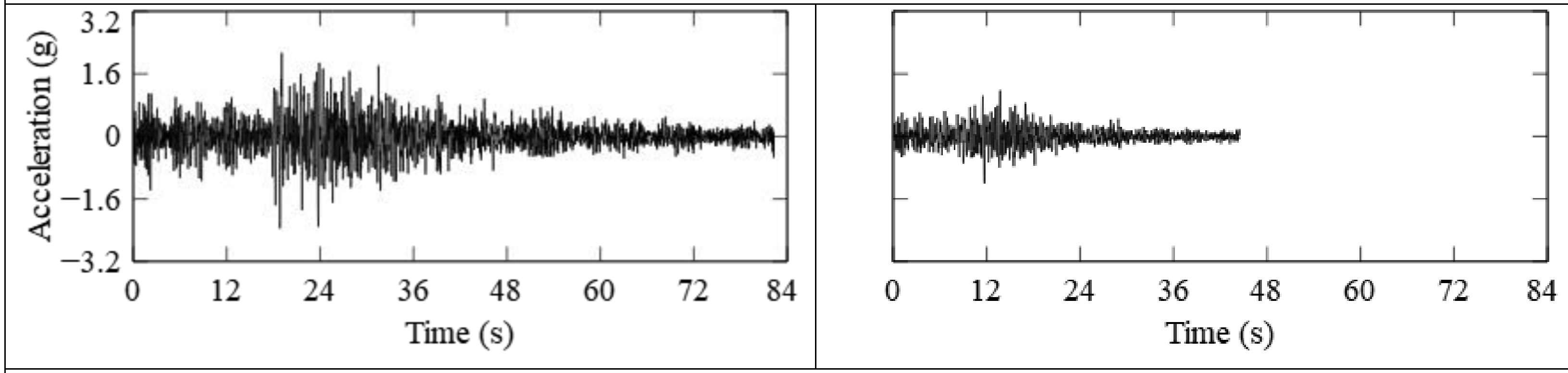

Fig. S36 Scaled Sequence Considered for Sl. No. 39 in Table A1

<table>
<tr><th>Main shock</th><th>Aftershock</th></tr>
<tr><td colspan="2">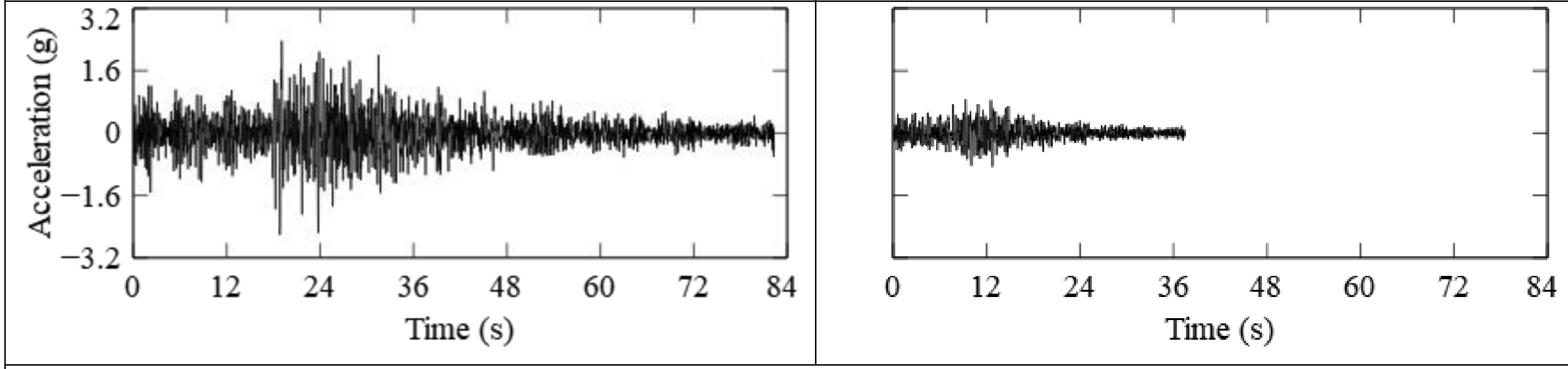
</td></tr>
<tr><td colspan="2">Fig. S37 Scaled Sequence Considered for Sl. No. 40 in Table A1</td></tr>
<tr><td colspan="2">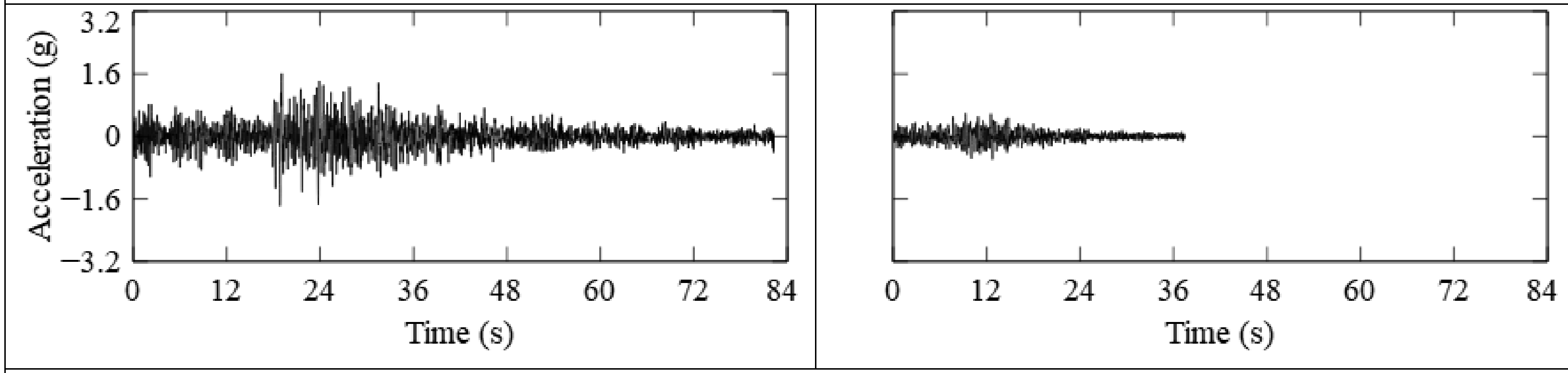
</td></tr>
<tr><td colspan="2">Fig. S38 Scaled Sequence Considered for Sl. No. 41 in Table A1</td></tr>
<tr><td colspan="2">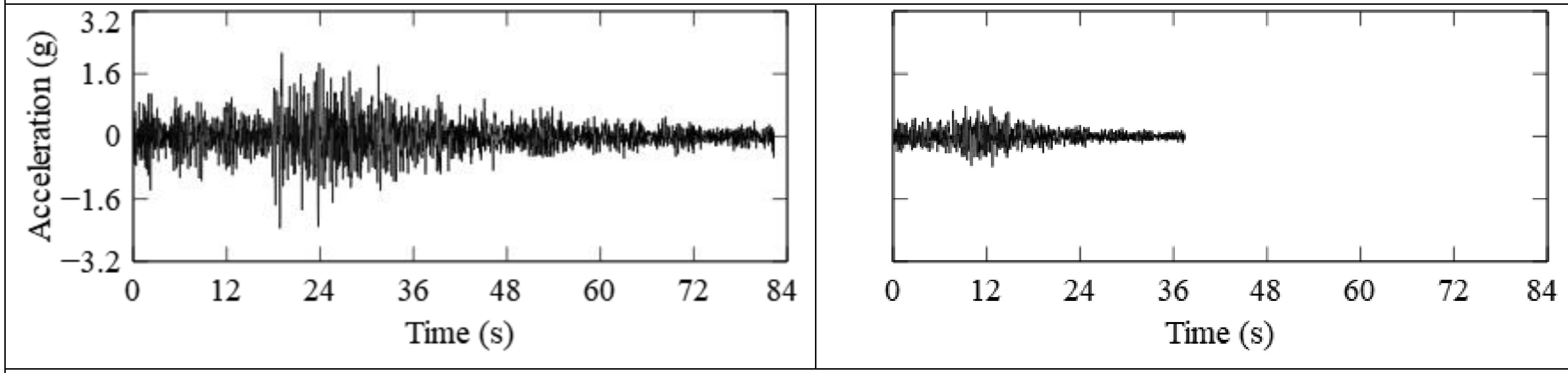
</td></tr>
<tr><td colspan="2">Fig. S39 Scaled Sequence Considered for Sl. No. 42 in Table A1</td></tr>
</table>

Main shock | Aftershock

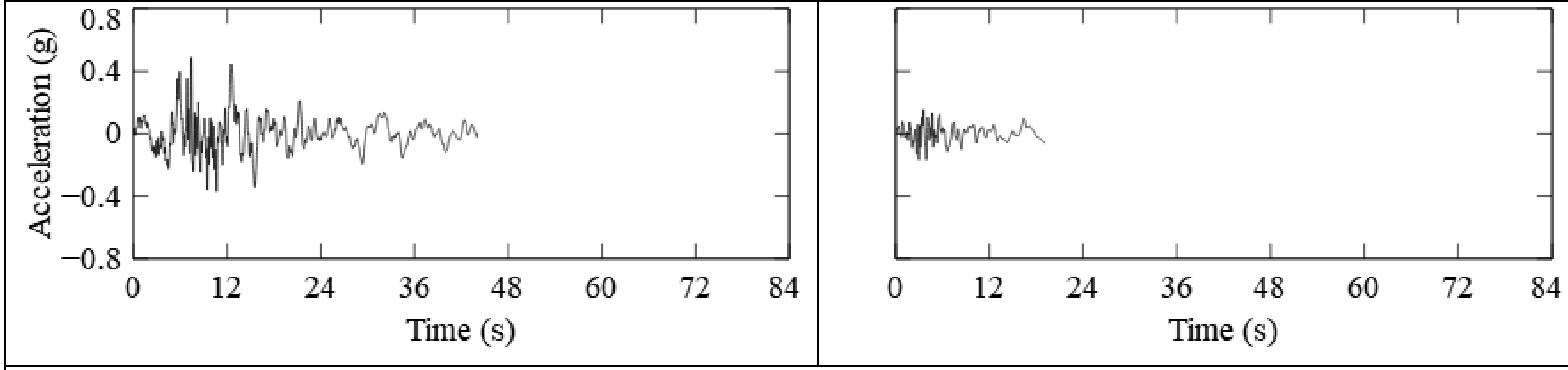

Fig. S40 Scaled Sequence Considered for Sl. No. 43 in Table A1

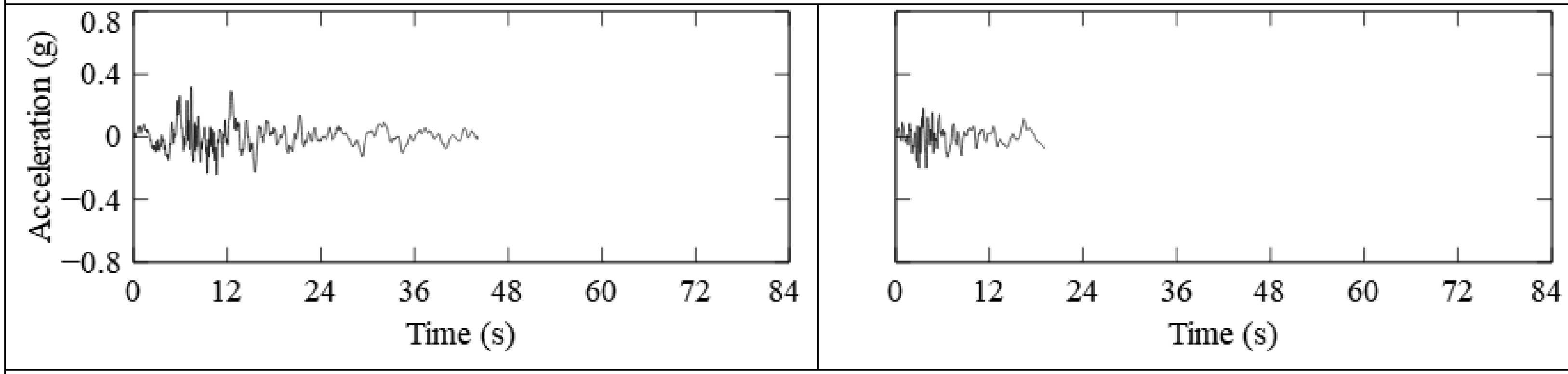

Fig. S41 Scaled Sequence Considered for Sl. No. 44 in Table A1

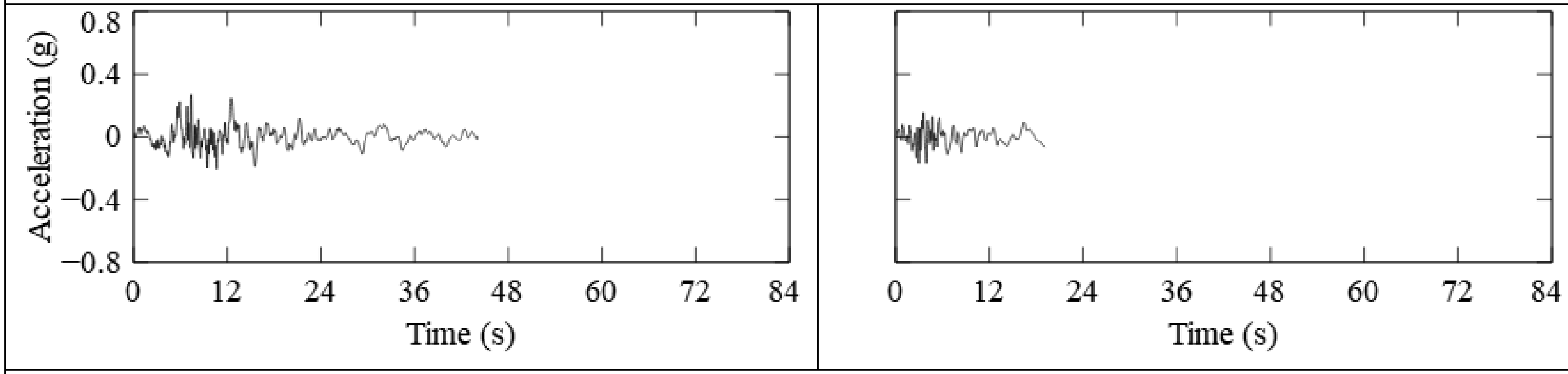

Fig. S42 Scaled Sequence Considered for Sl. No. 45 in Table A1

Main shock	Aftershock

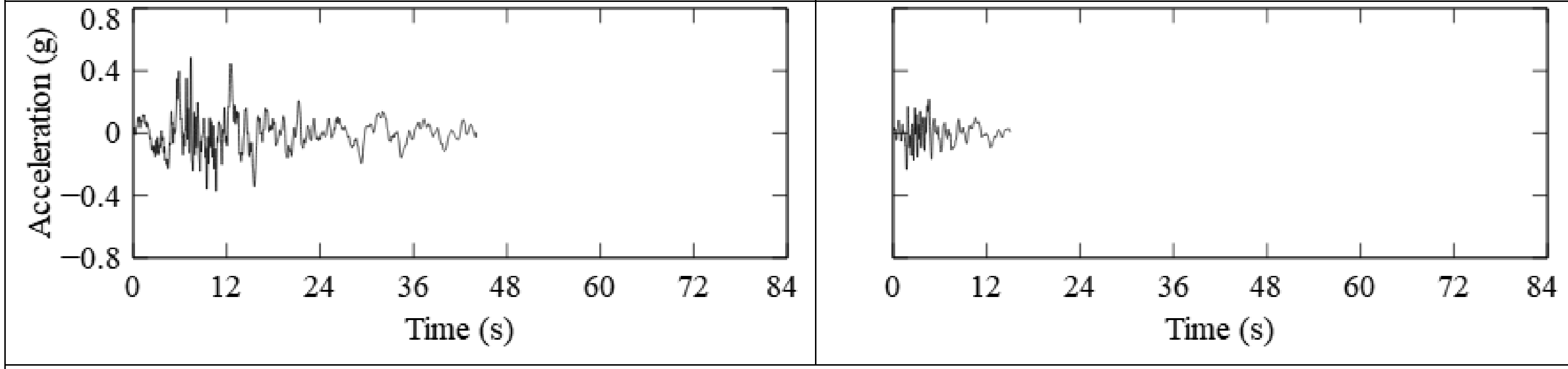

Fig. S43 Scaled Sequence Considered for Sl. No. 46 in Table A1

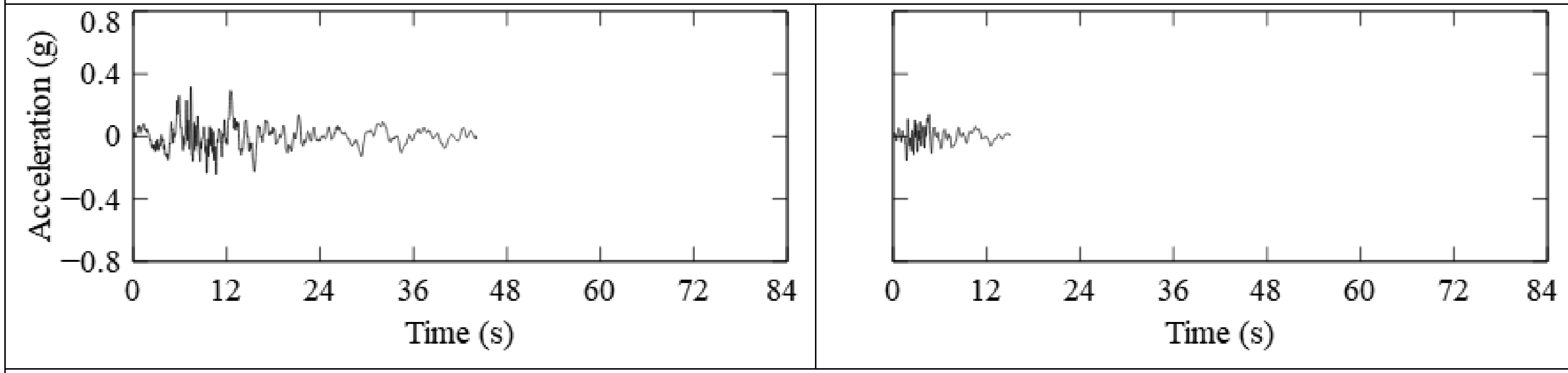

Fig. S44 Scaled Sequence Considered for Sl. No. 47 in Table A1

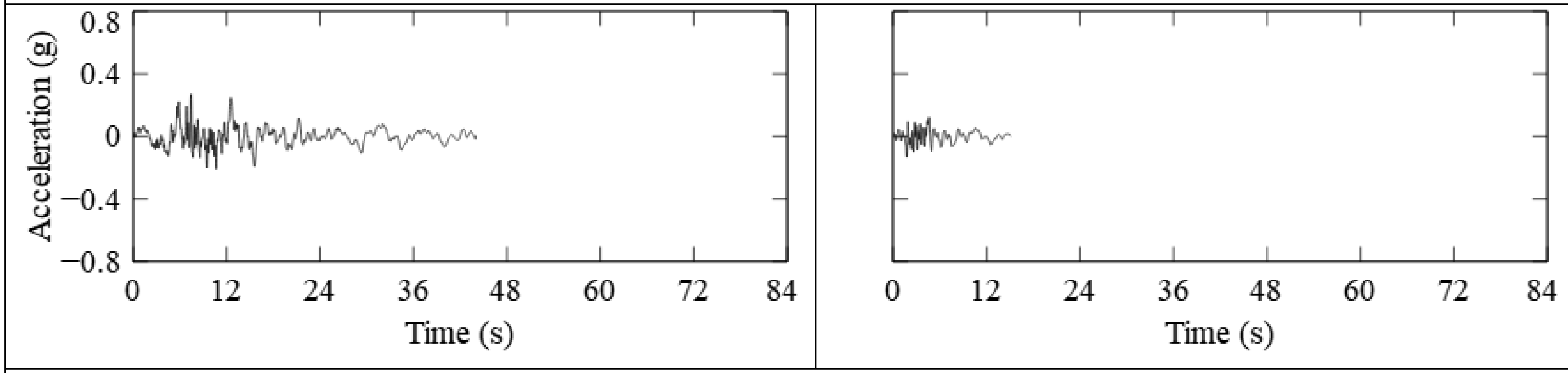

Fig. S45 Scaled Sequence Considered for Sl. No. 48 in Table A1

Main shock	Aftershock

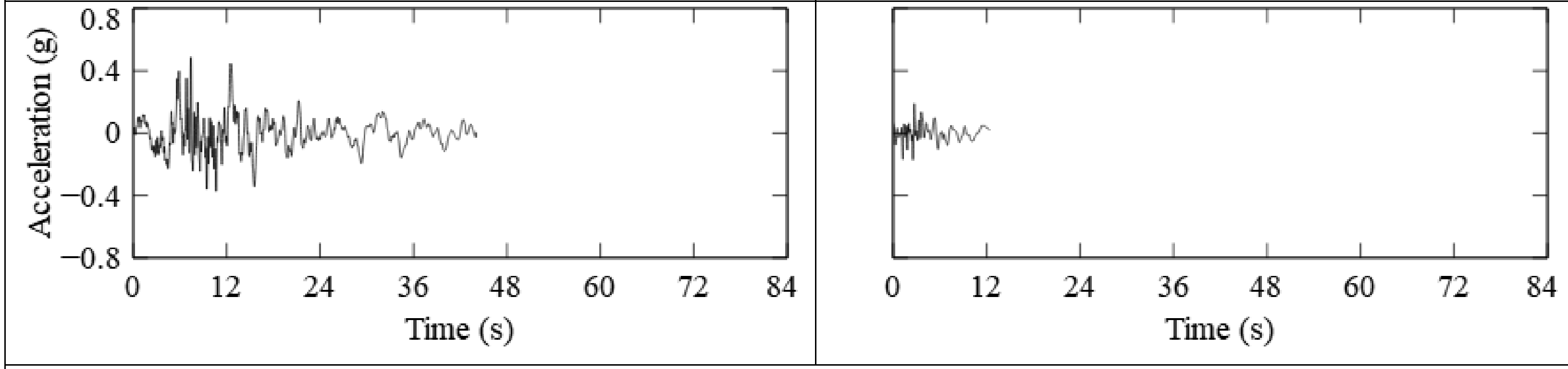

Fig. S46 Scaled Sequence Considered for Sl. No. 49 in Table A1

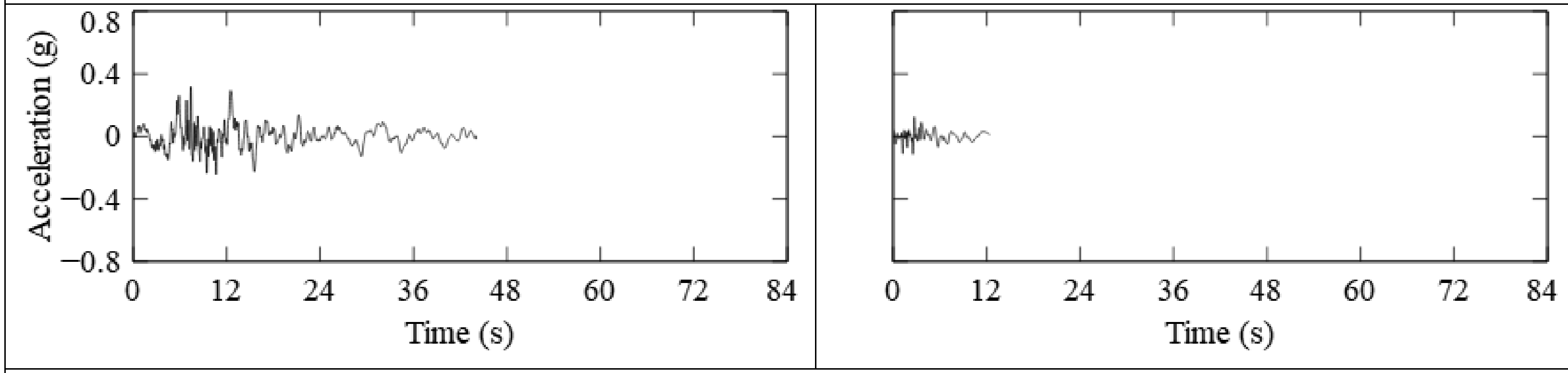

Fig. S47 Scaled Sequence Considered for Sl. No. 50 in Table A1

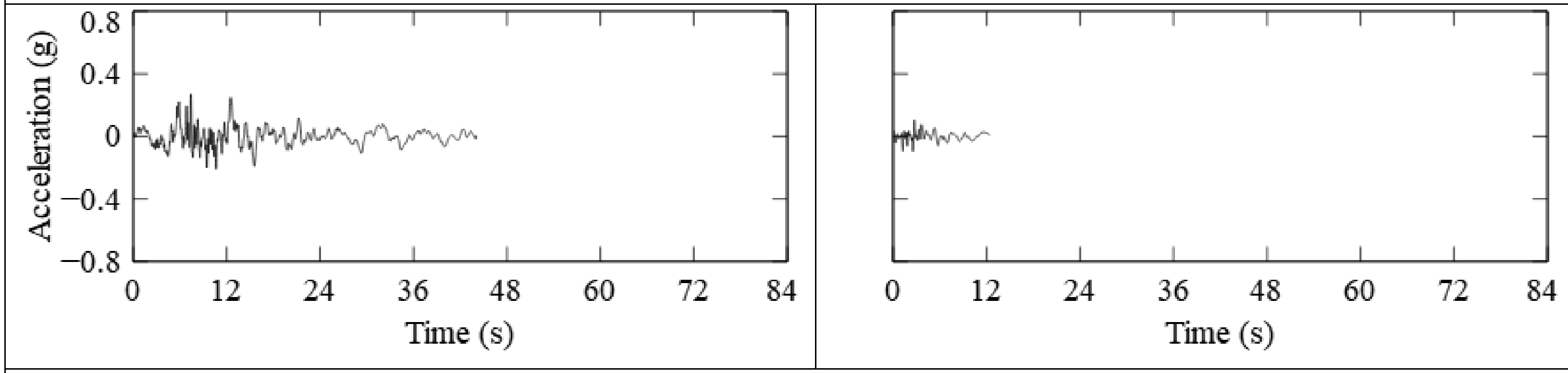

Fig. S48 Scaled Sequence Considered for Sl. No. 51 in Table A1

Main shock

Aftershock

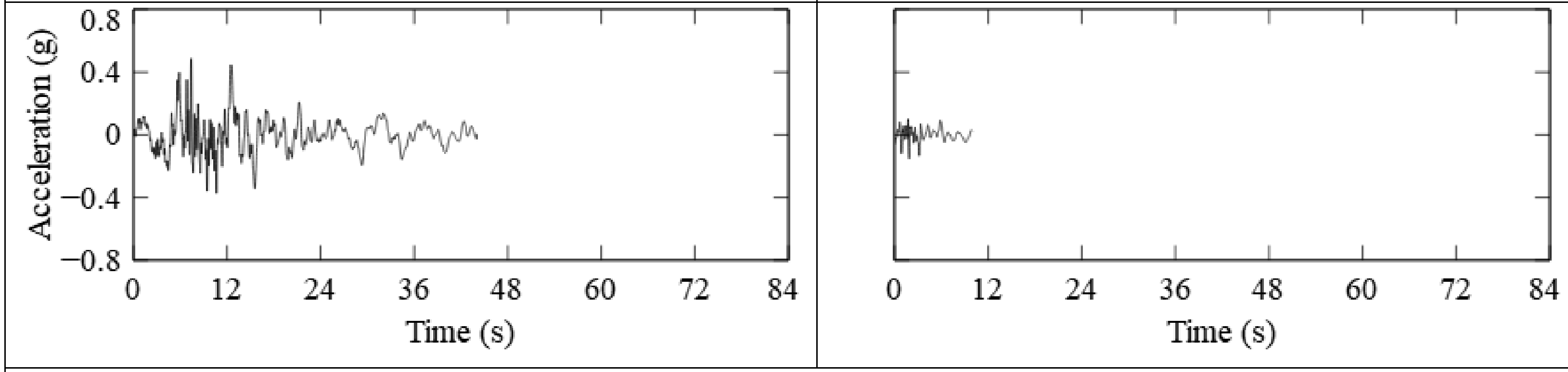

Fig. S49 Scaled Sequence Considered for Sl. No. 52 in Table A1

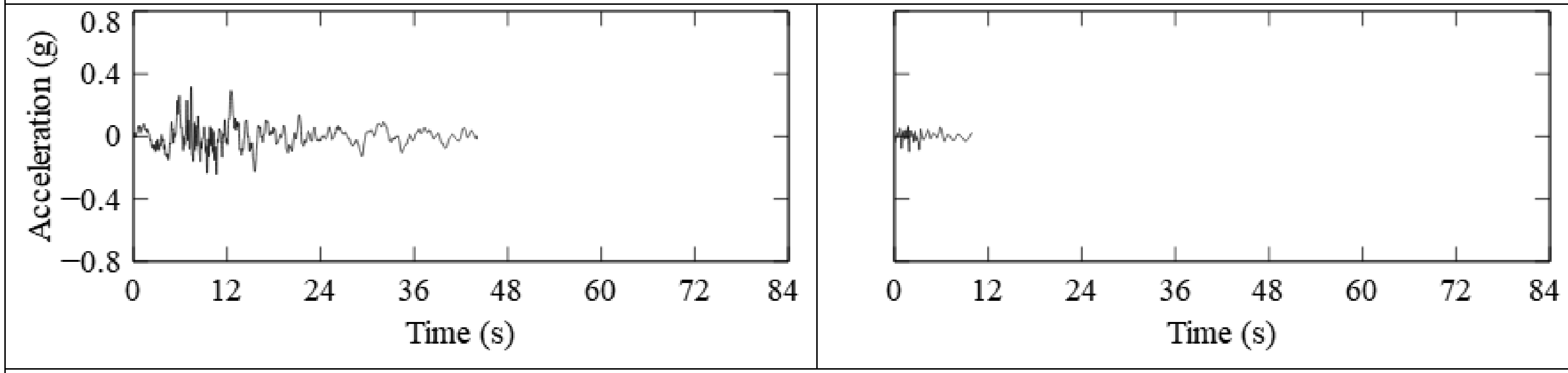

Fig. S50 Scaled Sequence Considered for Sl. No. 53 in Table A1

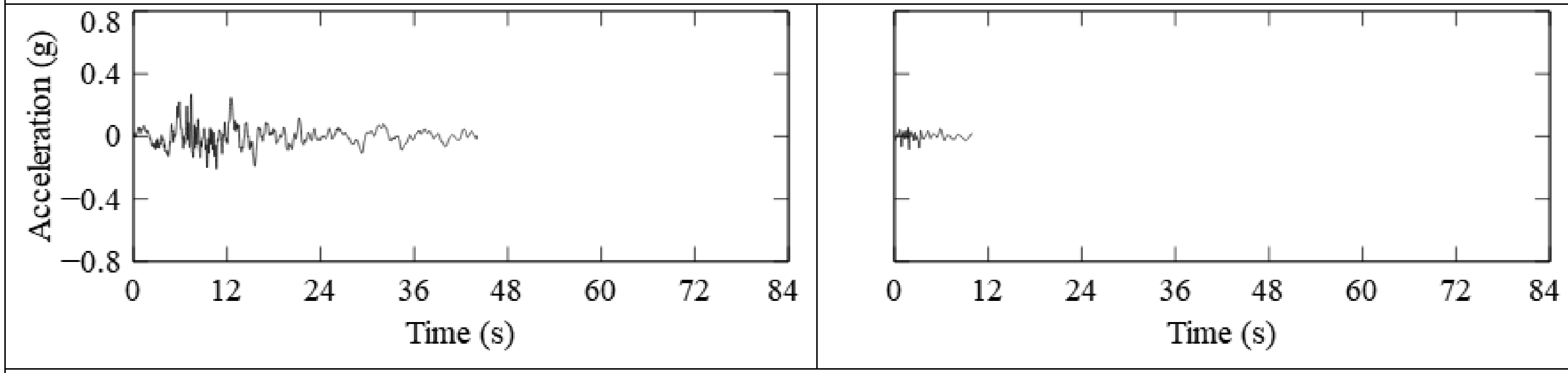

Fig. S51 Scaled Sequence Considered for Sl. No. 54 in Table A1

<table>
<tr><th>Main shock</th><th>Aftershock</th></tr>
<tr><td>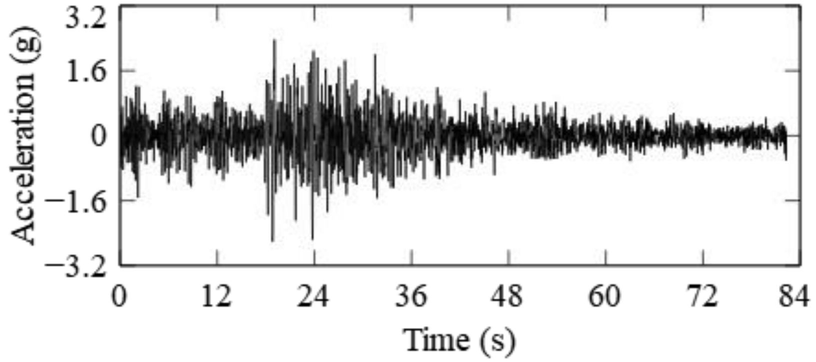
</td><td>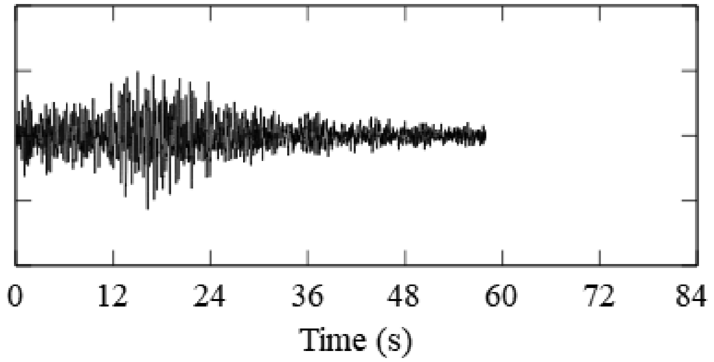
</td></tr>
<tr><td colspan="2">Fig. S52 Scaled Sequence Considered for Sl. No. 55 in Table A1</td></tr>
<tr><td>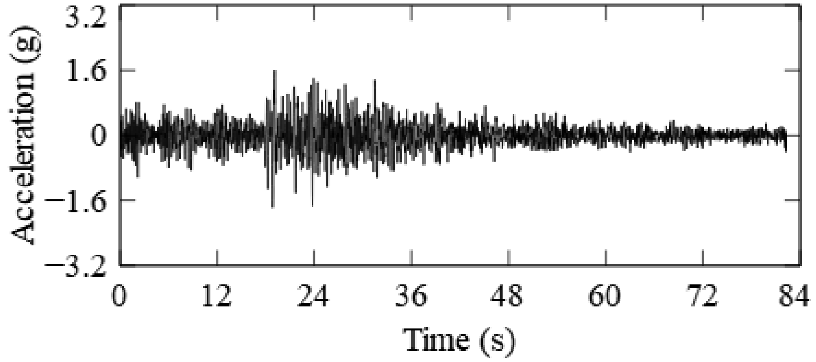
</td><td>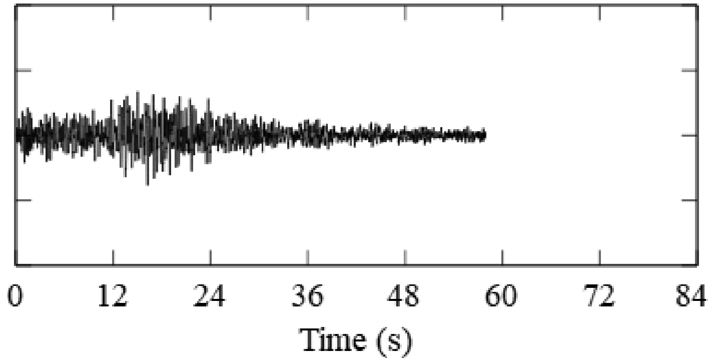
</td></tr>
<tr><td colspan="2">Fig. S253 Scaled Sequence Considered for Sl. No. 56 in Table A1</td></tr>
<tr><td>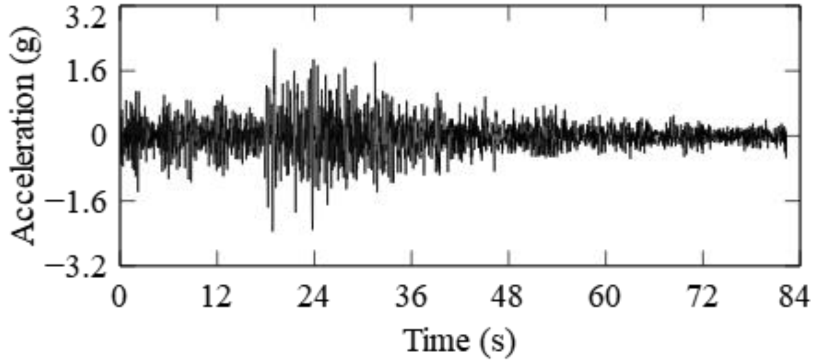
</td><td>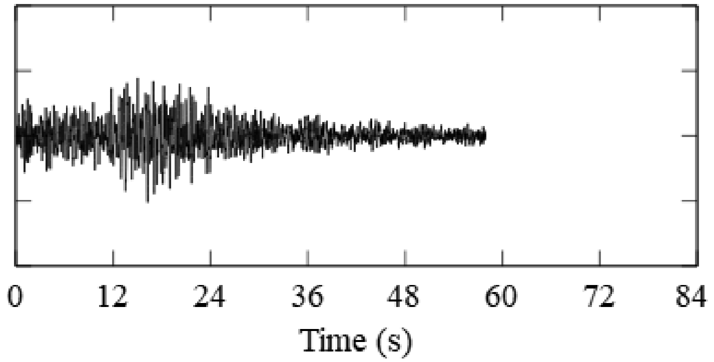
</td></tr>
<tr><td colspan="2">Fig. S54 Scaled Sequence Considered for Sl. No. 57 in Table A1</td></tr>
</table>

Main shock | Aftershock

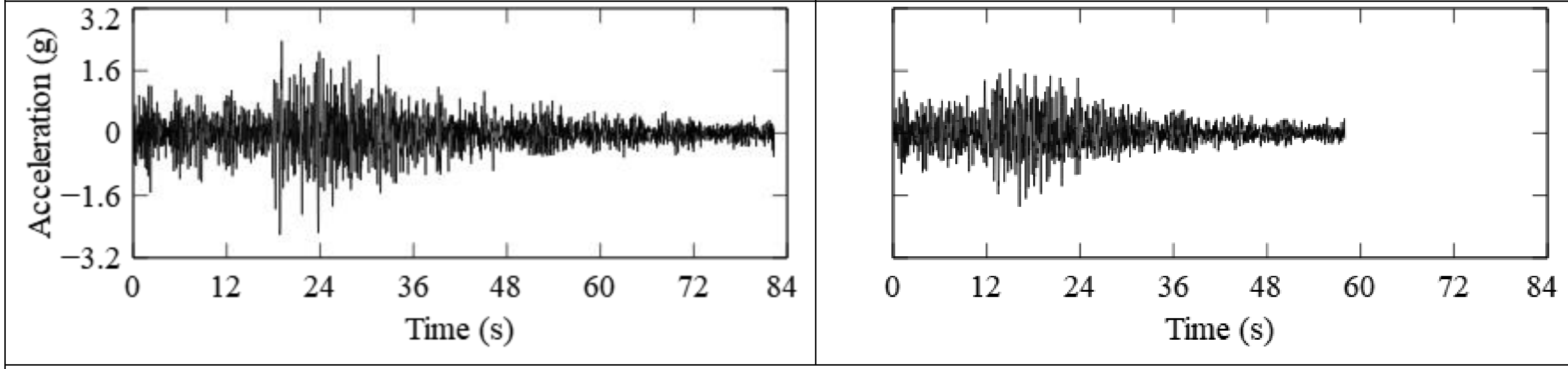

Fig. S55 Scaled Sequence Considered for Sl. No. 58 in Table A1

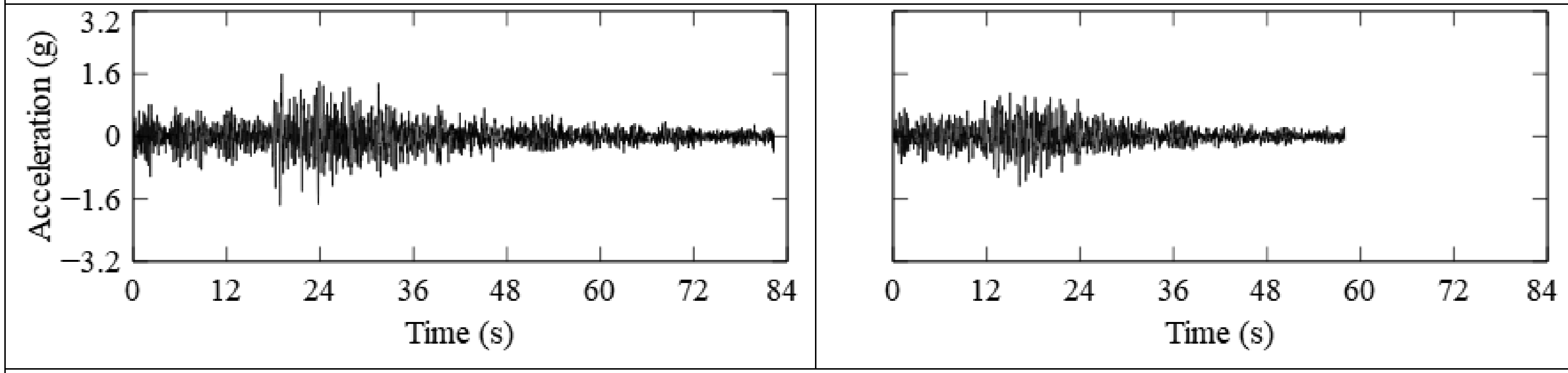

Fig. S56 Scaled Sequence Considered for Sl. No. 59 in Table A1

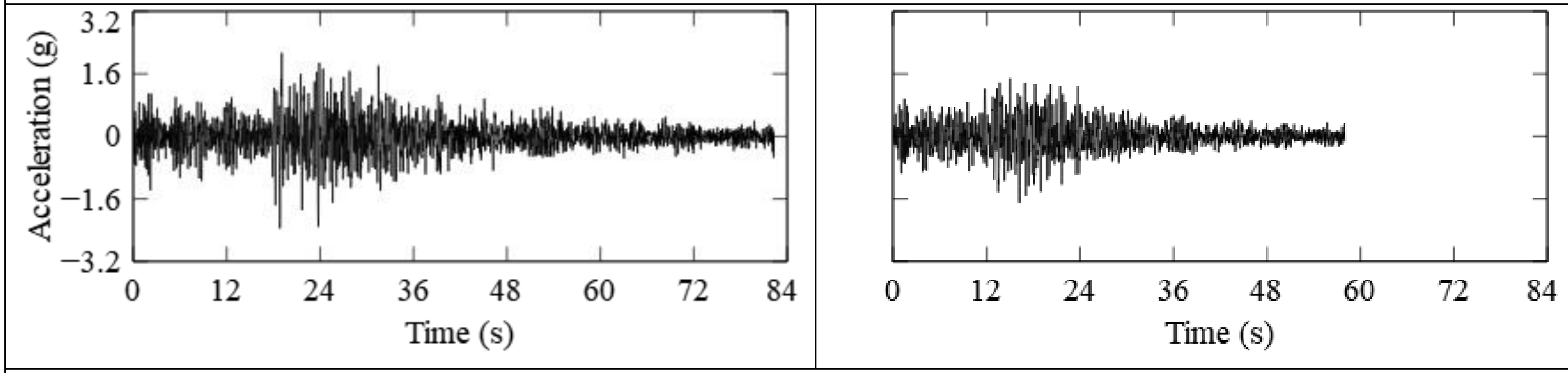

Fig. S57 Scaled Sequence Considered for Sl. No. 60 in Table A1

Main shock	Aftershock

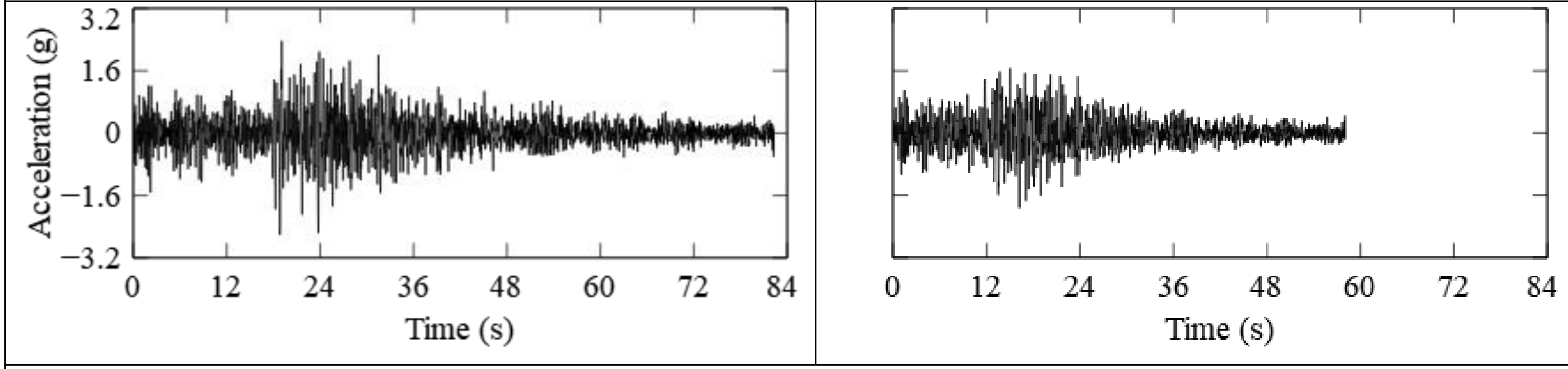

Fig. S58 Scaled Sequence Considered for Sl. No. 61 in Table A1

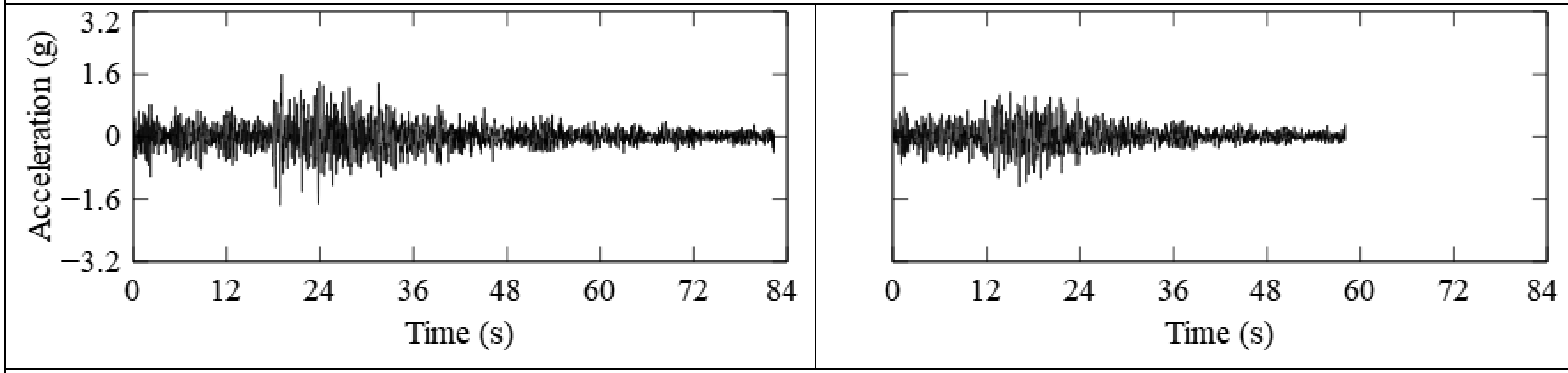

Fig. S59 Scaled Sequence Considered for Sl. No. 62 in Table A1

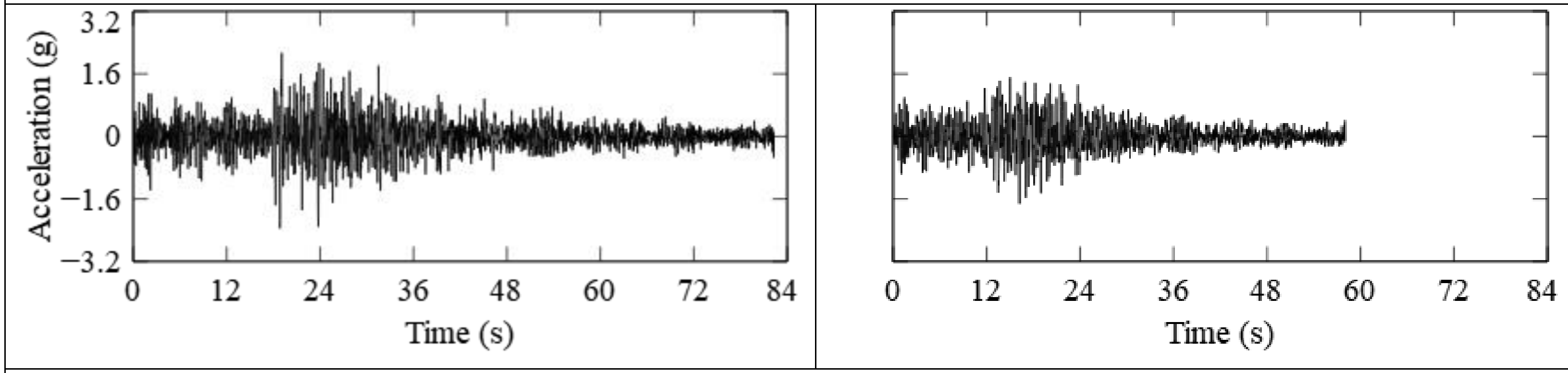

Fig. S60 Scaled Sequence Considered for Sl. No. 63 in Table A1

Main shock	Aftershock

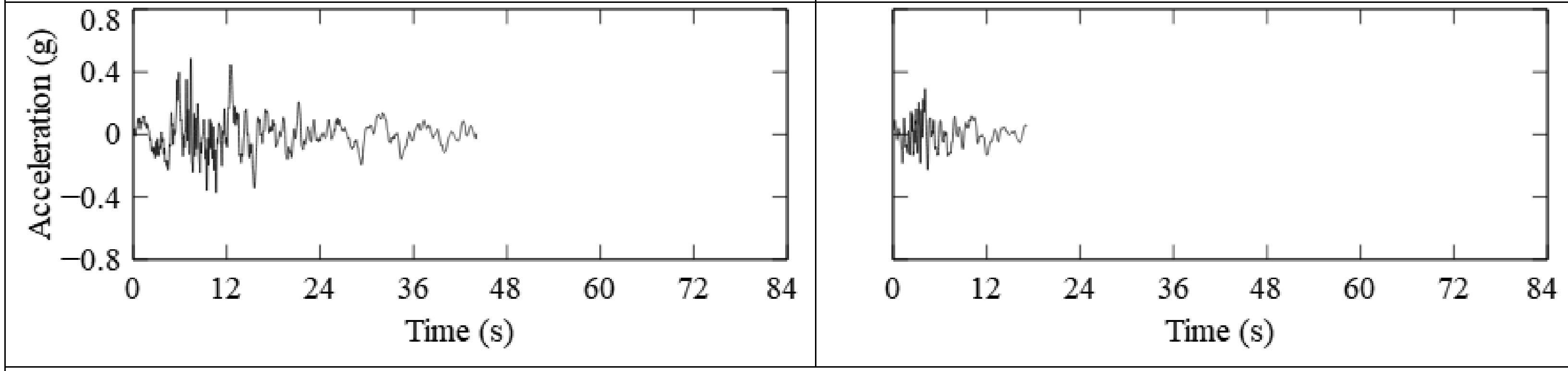

Fig. S61 Scaled Sequence Considered for Sl. No. 64 in Table A1

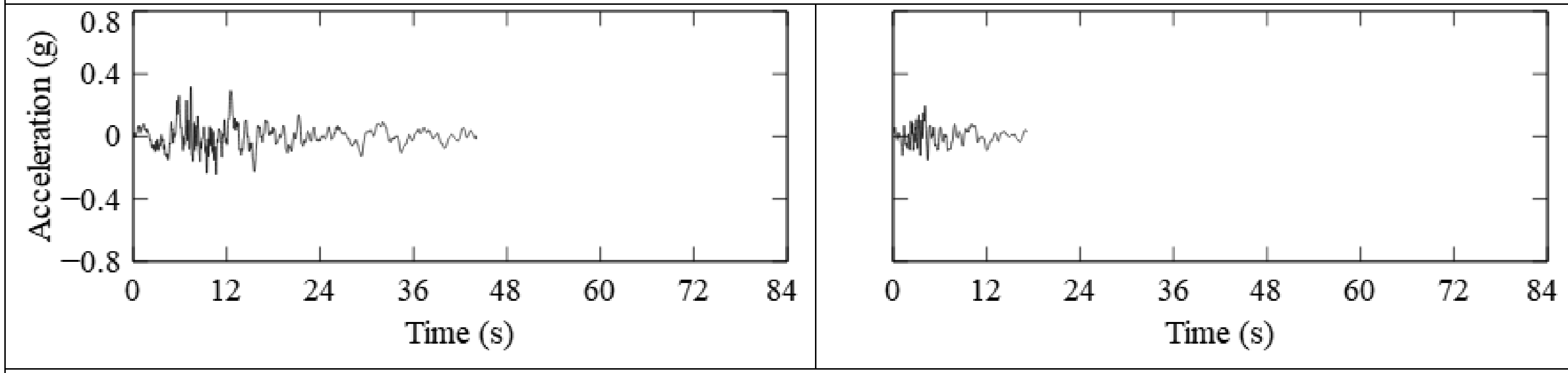

Fig. S62 Scaled Sequence Considered for Sl. No. 65 in Table A1

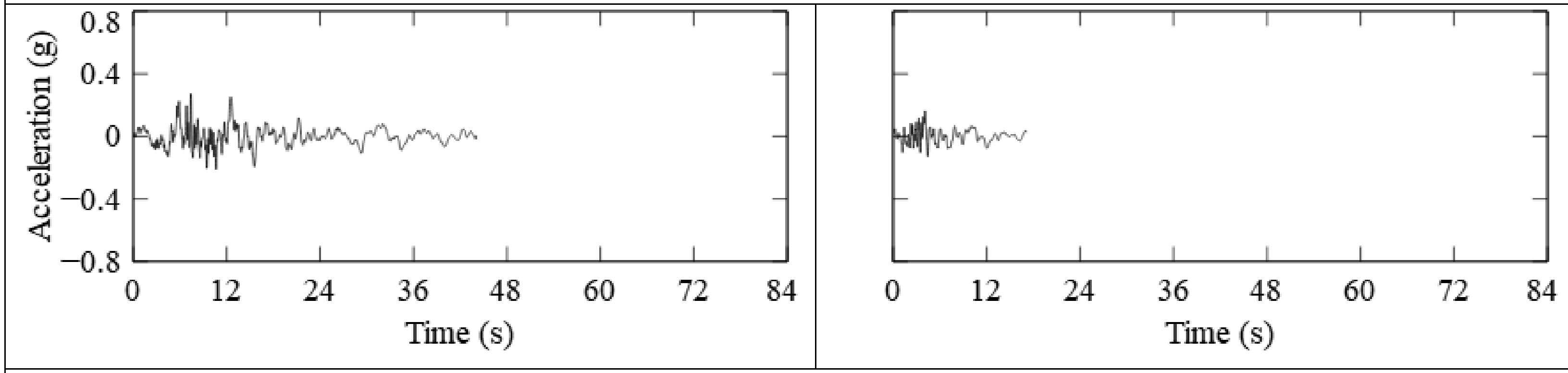

Fig. S63 Scaled Sequence Considered for Sl. No. 66 in Table A1

Main shock

Aftershock

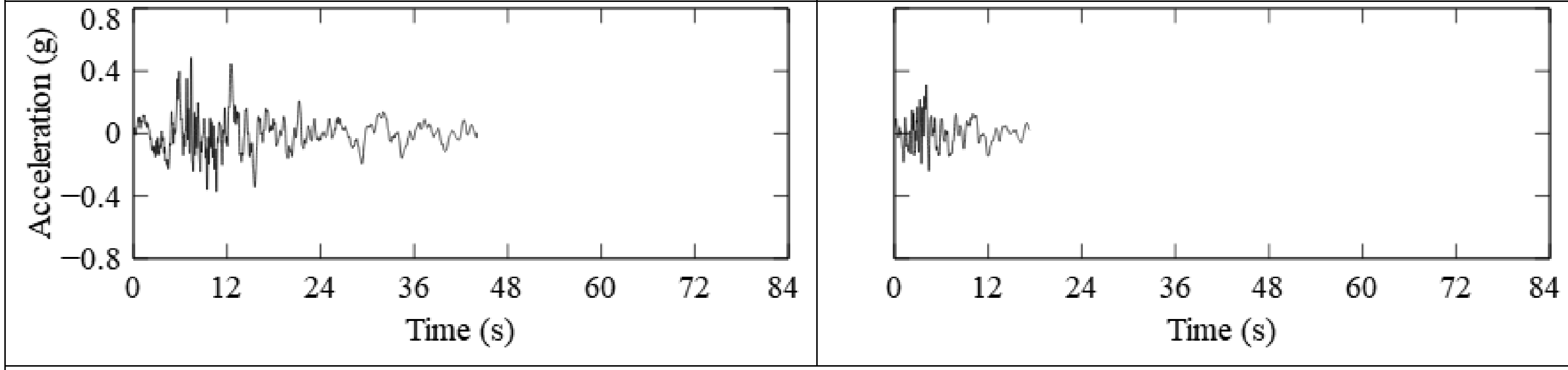

Fig. S64 Scaled Sequence Considered for Sl. No. 67 in Table A1

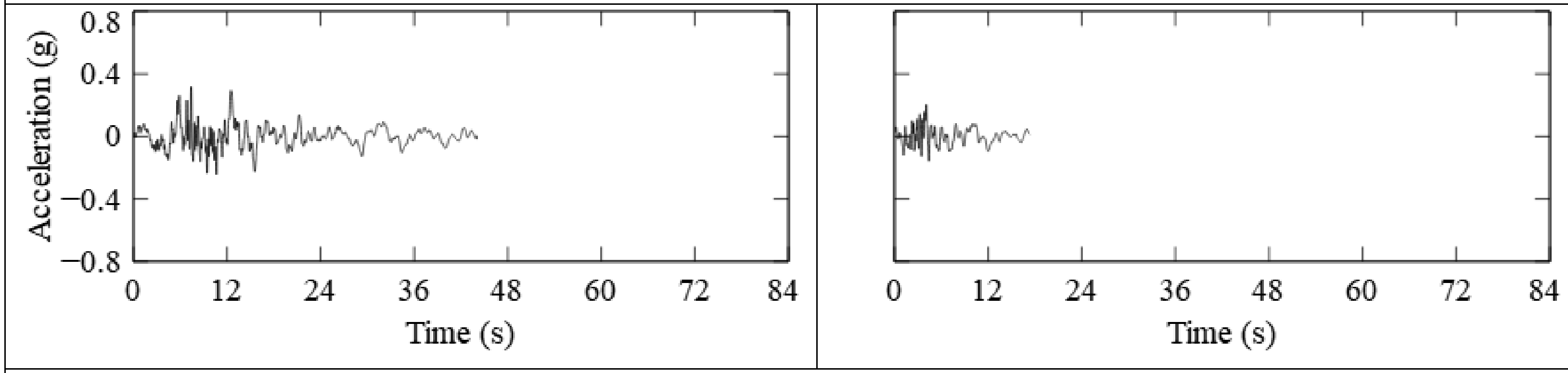

Fig. S65 Scaled Sequence Considered for Sl. No. 68 in Table A1

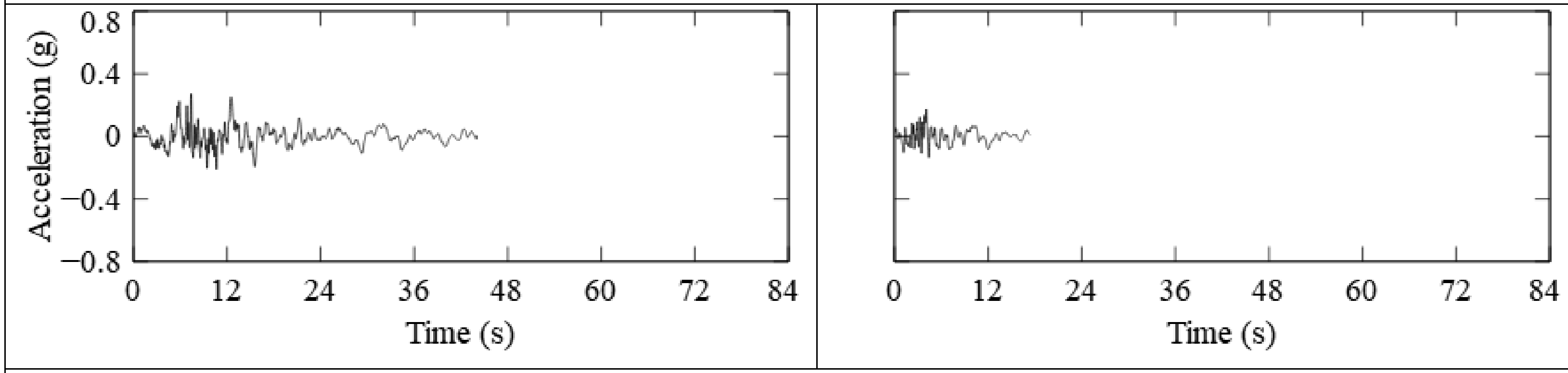

Fig. S66 Scaled Sequence Considered for Sl. No. 69 in Table A1

Main shock	Aftershock

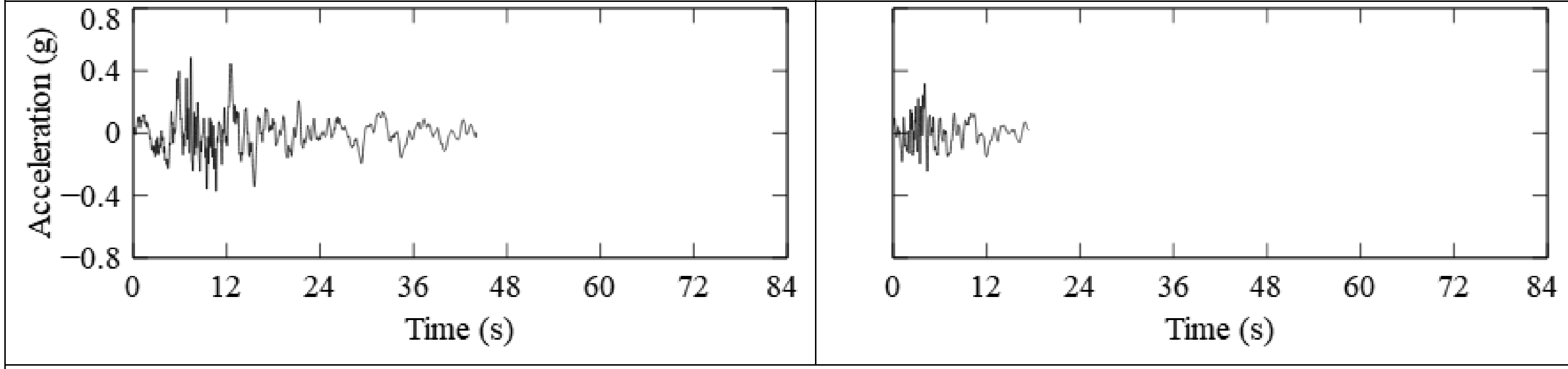

Fig. S67 Scaled Sequence Considered for Sl. No. 70 in Table A1

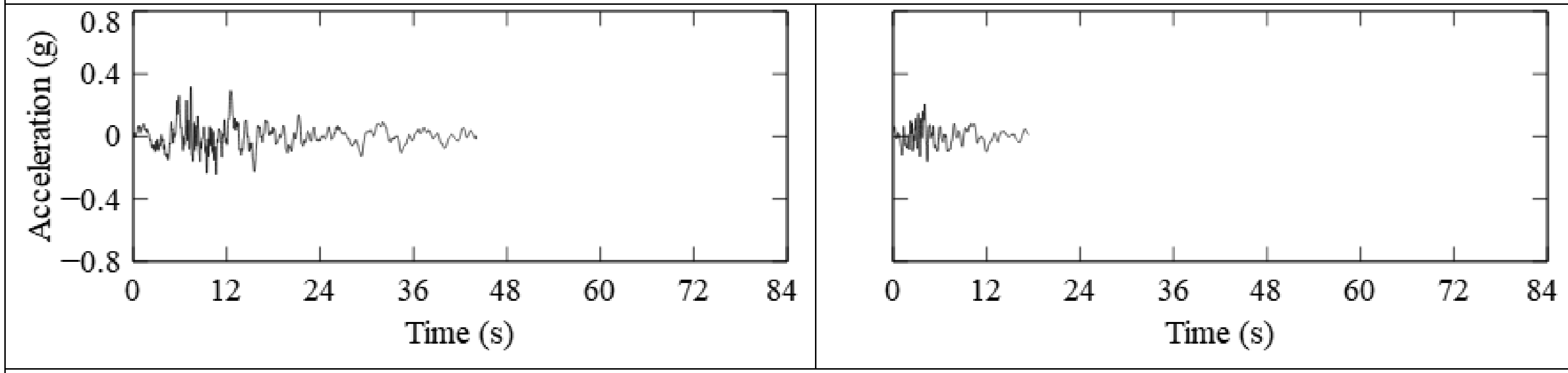

Fig. S68 Scaled Sequence Considered for Sl. No. 71 in Table A1

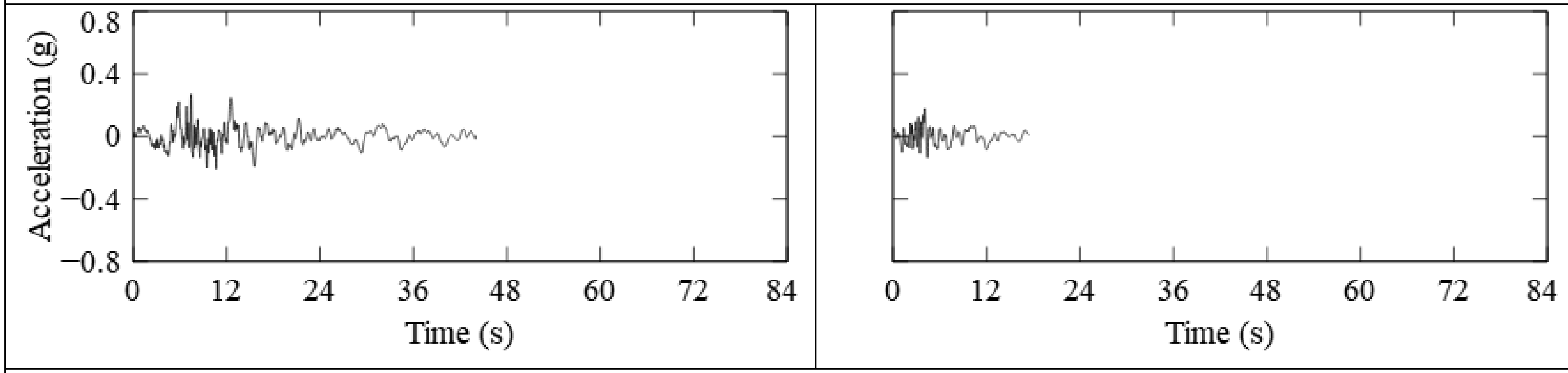

Fig. S69 Scaled Sequence Considered for Sl. No. 72 in Table A1

<table>
<tr><th>Main shock</th><th>Aftershock</th></tr>
<tr><td>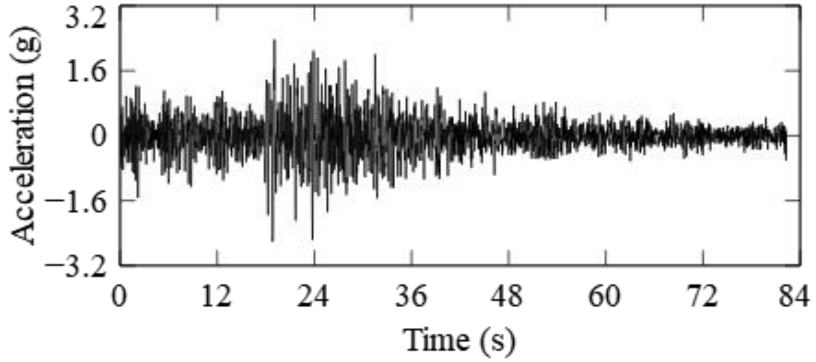
</td><td>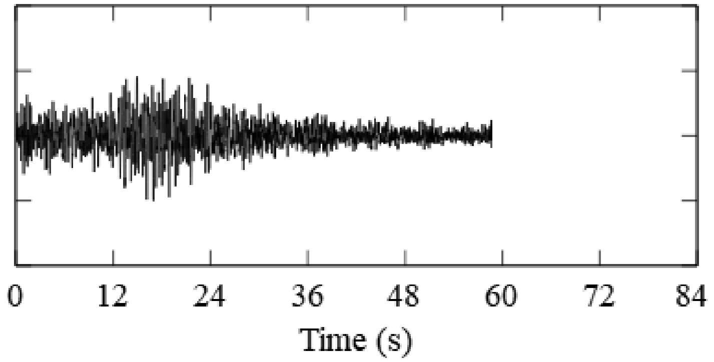
</td></tr>
<tr><td colspan="2">Fig. S70 Scaled Sequence Considered for Sl. No. 73 in Table A1</td></tr>
<tr><td>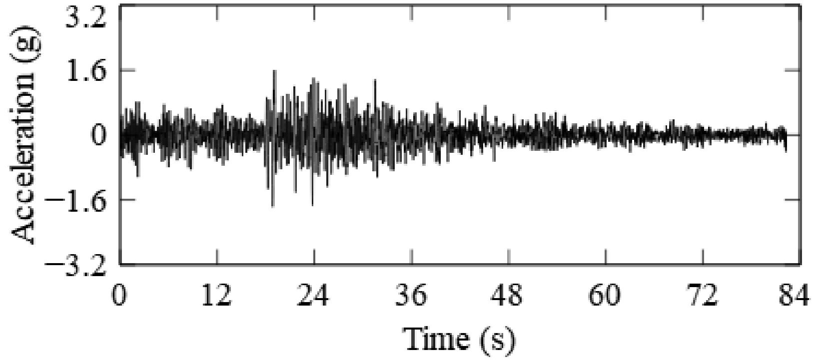
</td><td>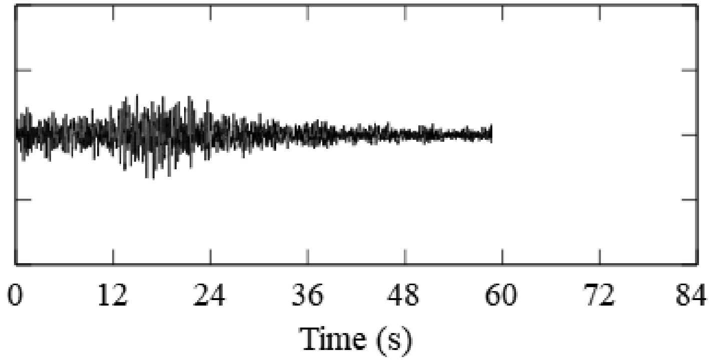
</td></tr>
<tr><td colspan="2">Fig. S71 Scaled Sequence Considered for Sl. No. 74 in Table A1</td></tr>
<tr><td>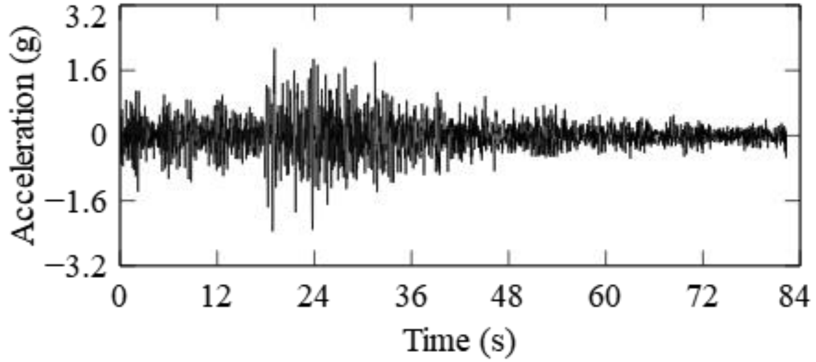
</td><td>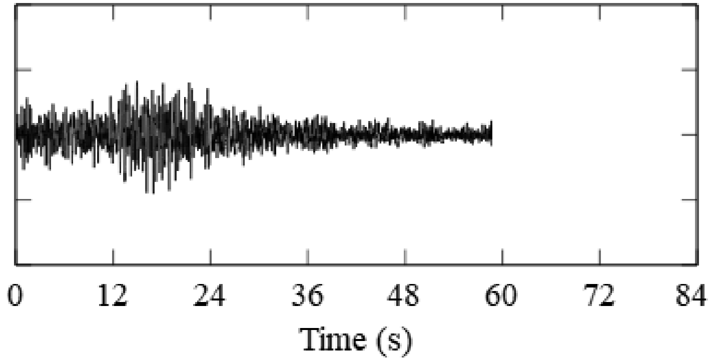
</td></tr>
<tr><td colspan="2">Fig. S72 Scaled Sequence Considered for Sl. No. 75 in Table A1</td></tr>
</table>

Main shock

Aftershock

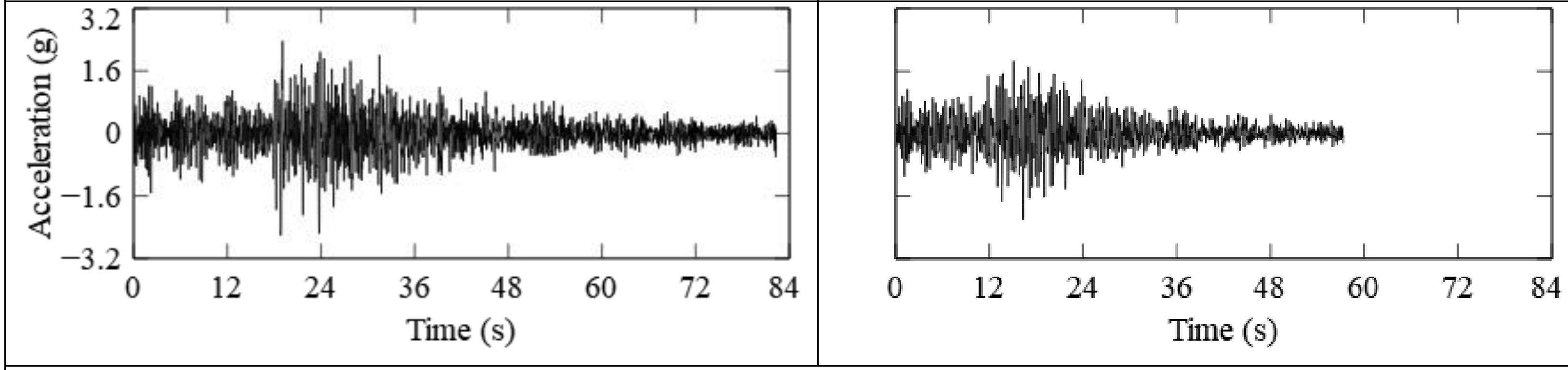

Fig. S73 Scaled Sequence Considered for Sl. No. 79 in Table A1

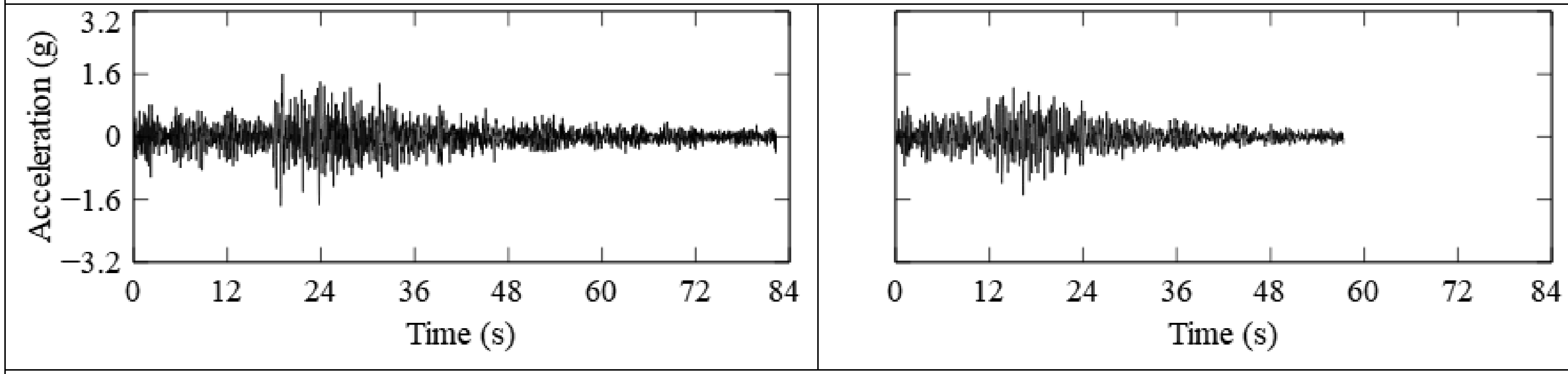

Fig. S74 Scaled Sequence Considered for Sl. No. 80 in Table A1

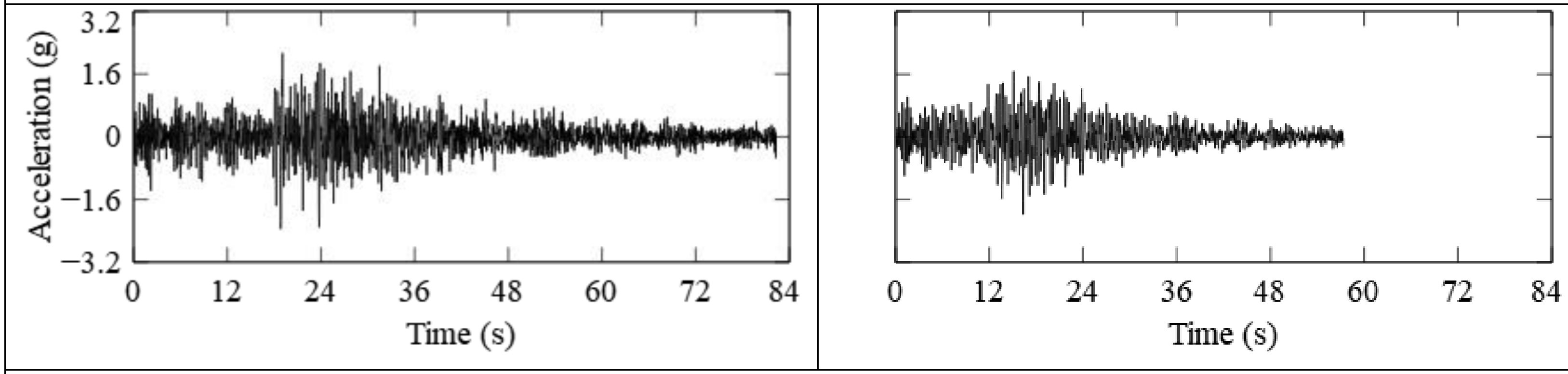

Fig. S75 Scaled Sequence Considered for Sl. No. 81 in Table A1

Main shock

Aftershock

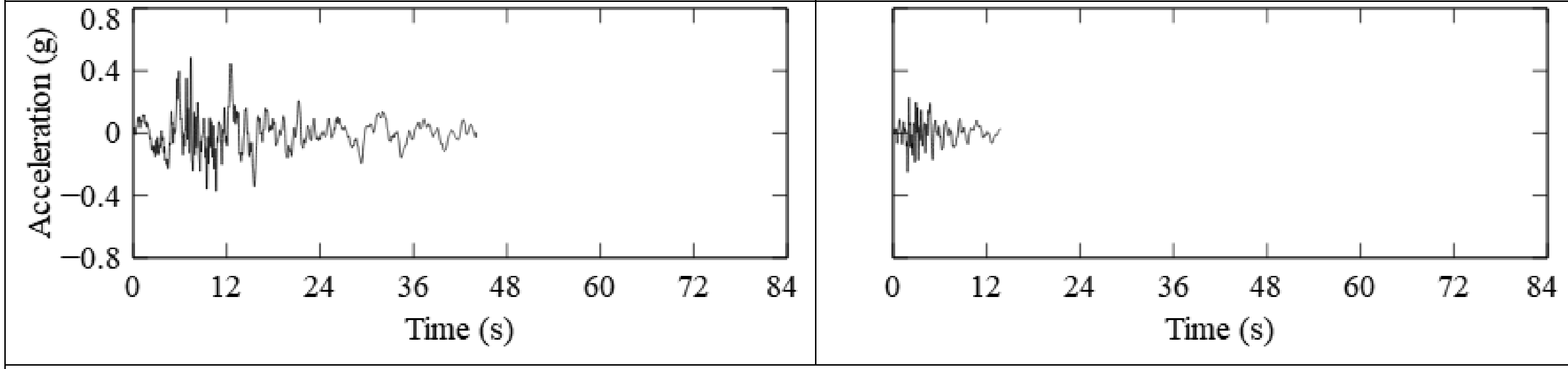

Fig. S76 Scaled Sequence Considered for Sl. No. 82 in Table A1

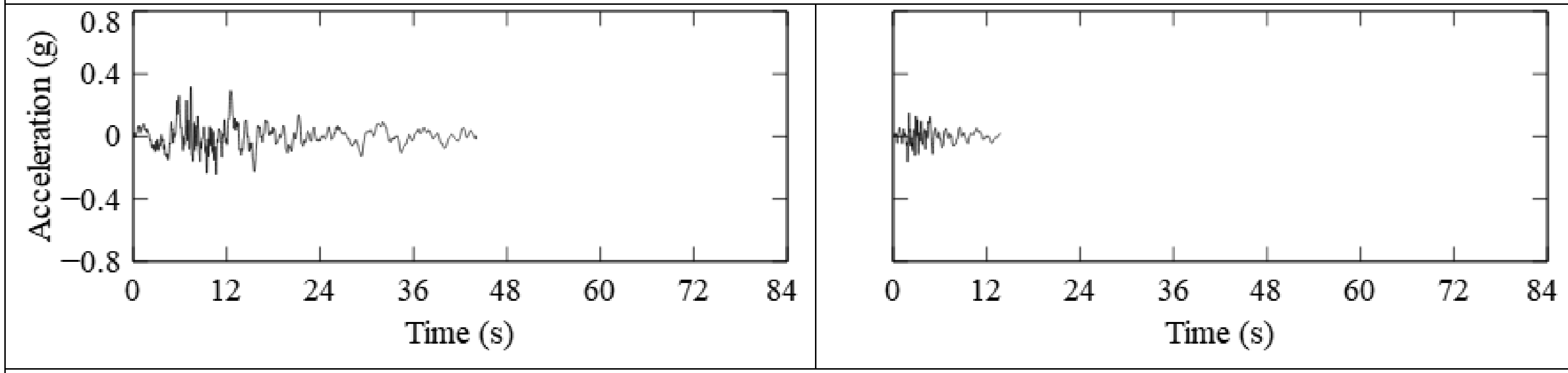

Fig. S77 Scaled Sequence Considered for Sl. No. 83 in Table A1

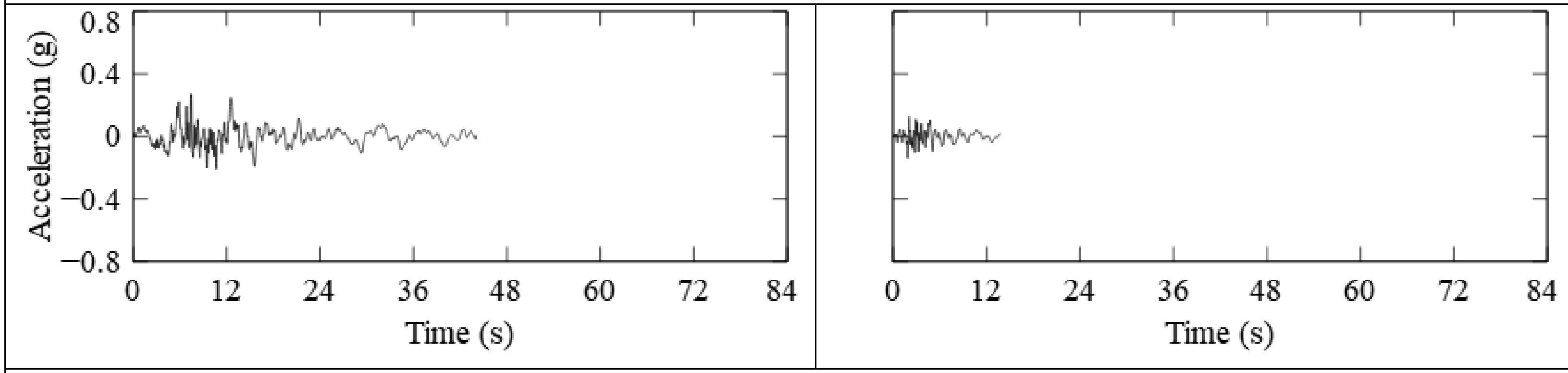

Fig. S78 Scaled Sequence Considered for Sl. No. 84 in Table A1

Main shock	Aftershock

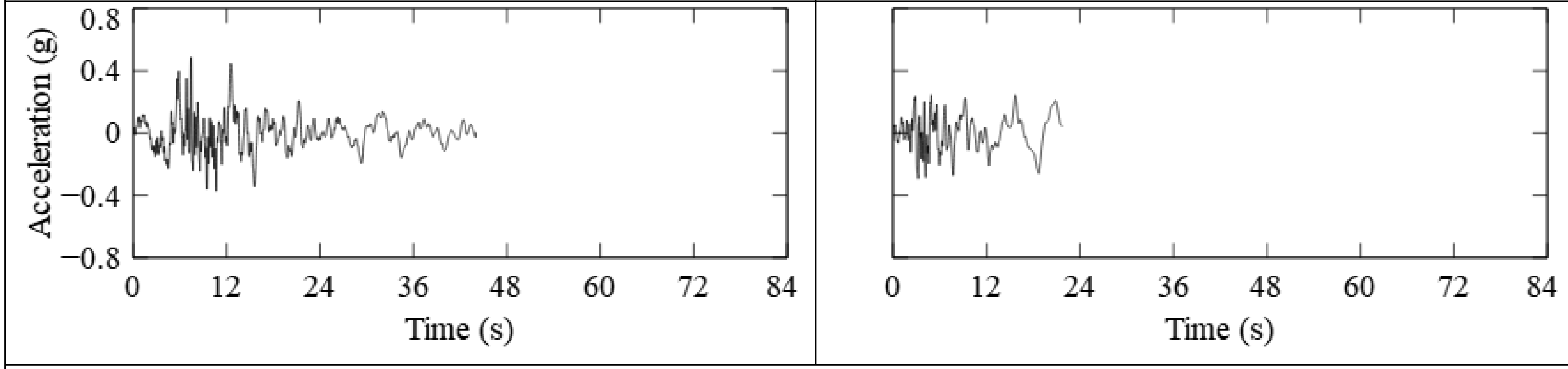

Fig. S79 Scaled Sequence Considered for Sl. No. 88 in Table A1

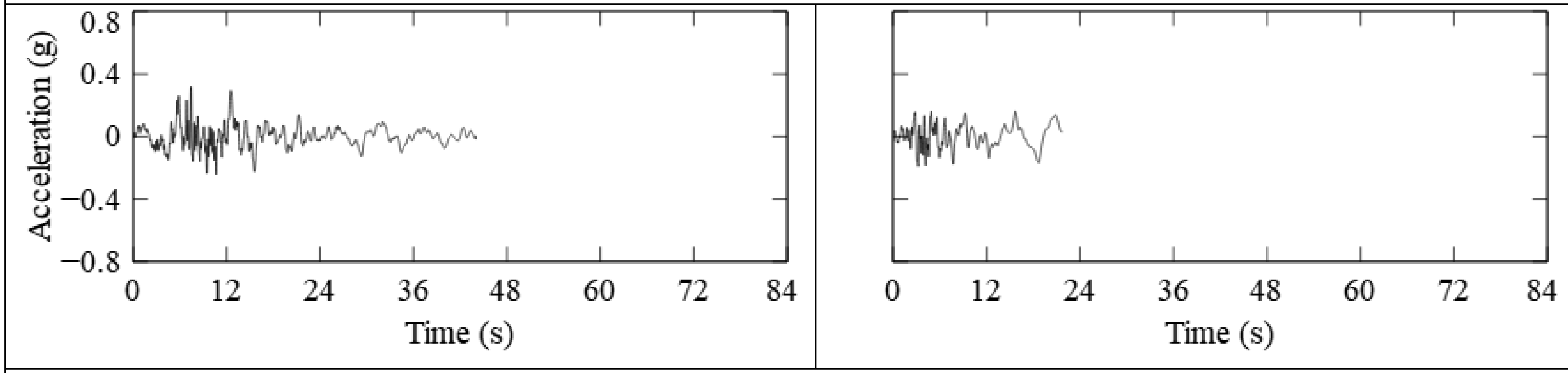

Fig. S80 Scaled Sequence Considered for Sl. No. 89 in Table A1

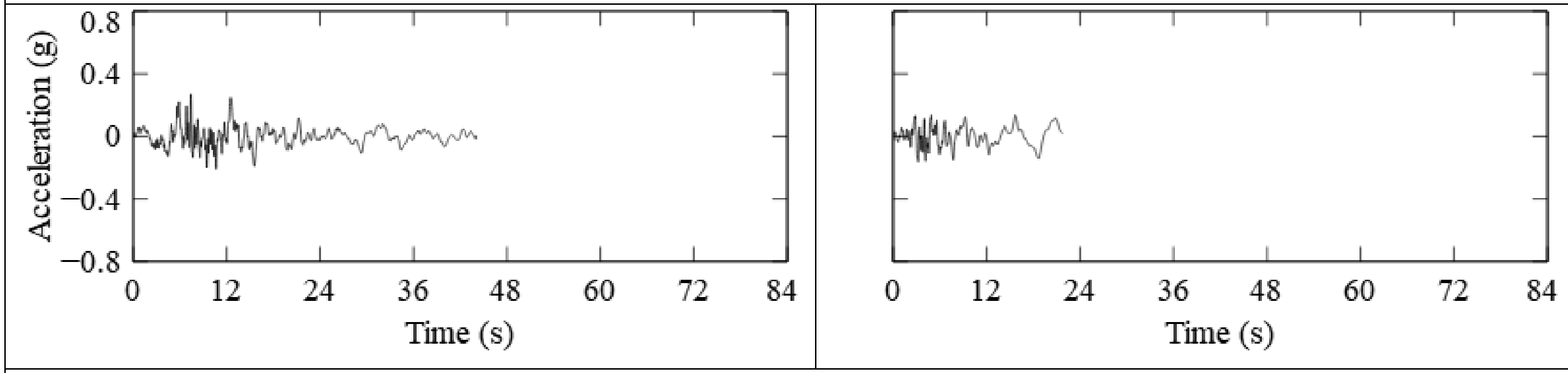

Fig. S81 Scaled Sequence Considered for Sl. No. 90 in Table A1

Main shock	Aftershock

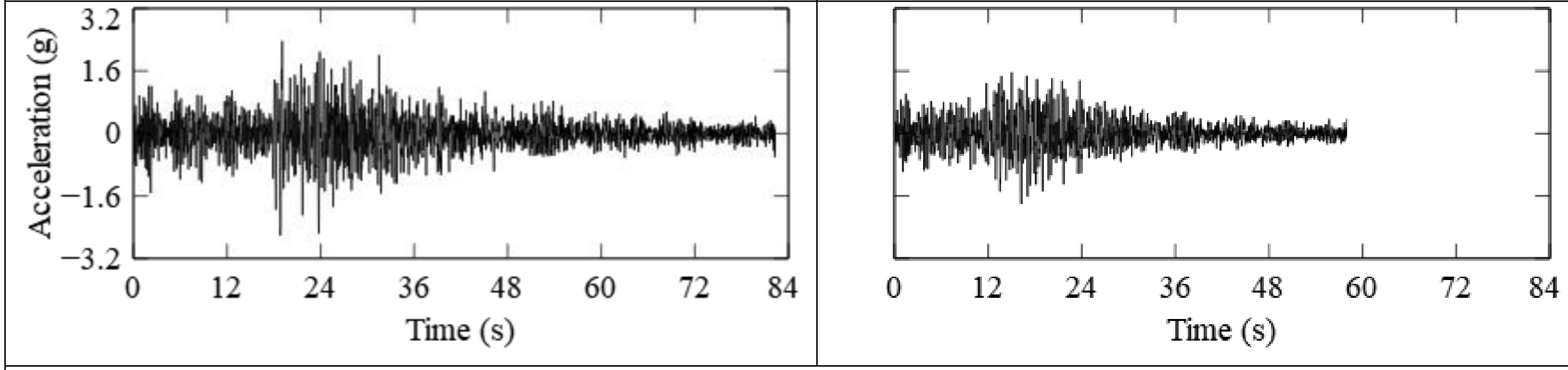

Fig. S82 Scaled Sequence Considered for Sl. No. 94 in Table A1

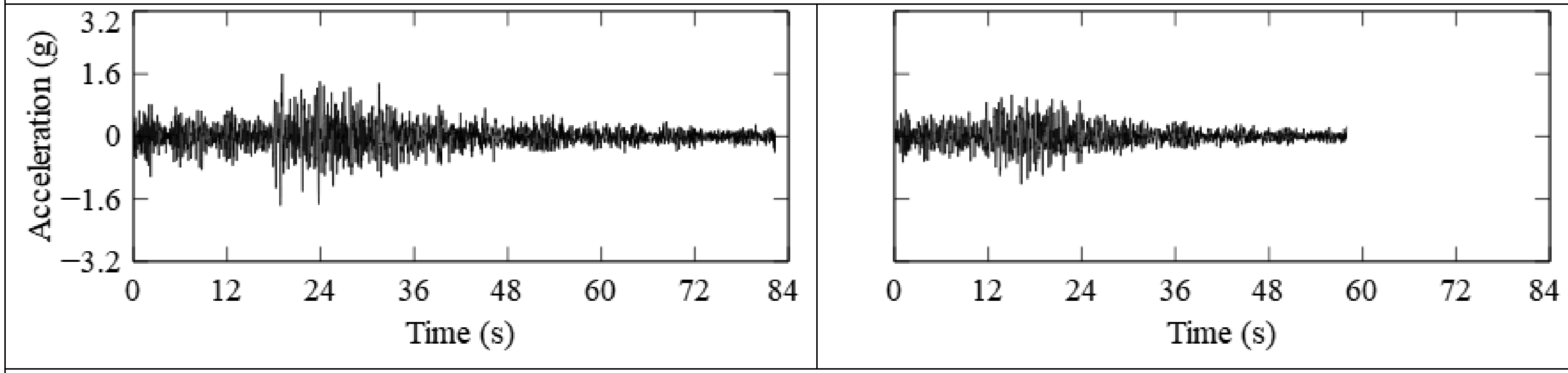

Fig. S83 Scaled Sequence Considered for Sl. No. 95 in Table A1

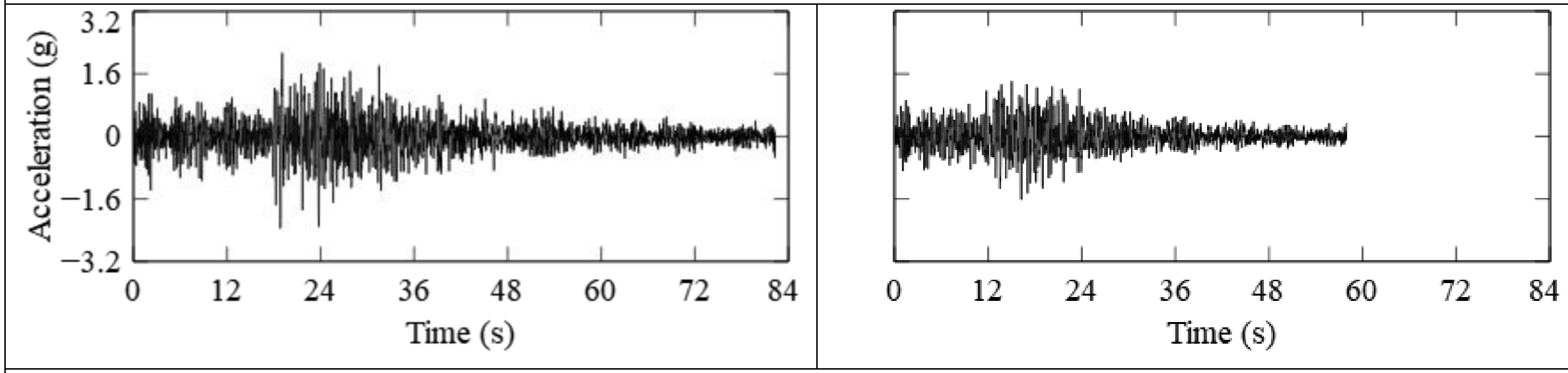

Fig. S84 Scaled Sequence Considered for Sl. No. 96 in Table A1

Main shock

Aftershock

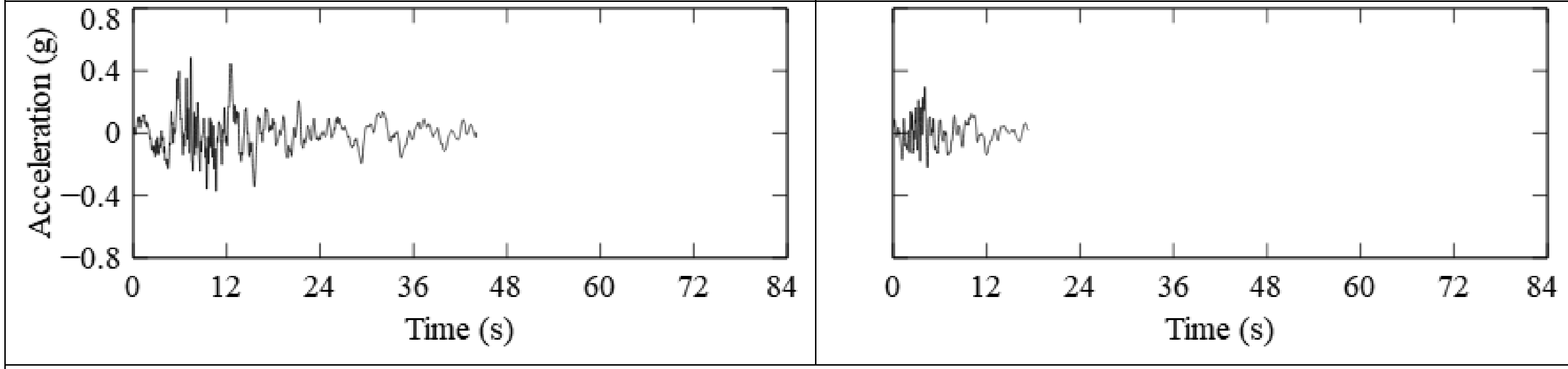

Fig. S85 Scaled Sequence Considered for Sl. No. 100 in Table A1

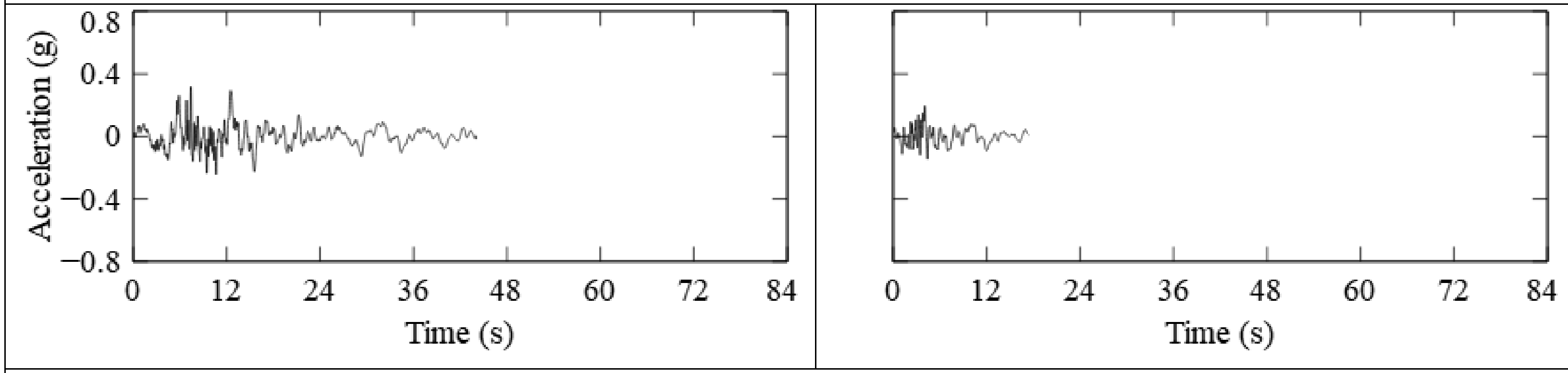

Fig. S86 Scaled Sequence Considered for Sl. No. 101 in Table A1

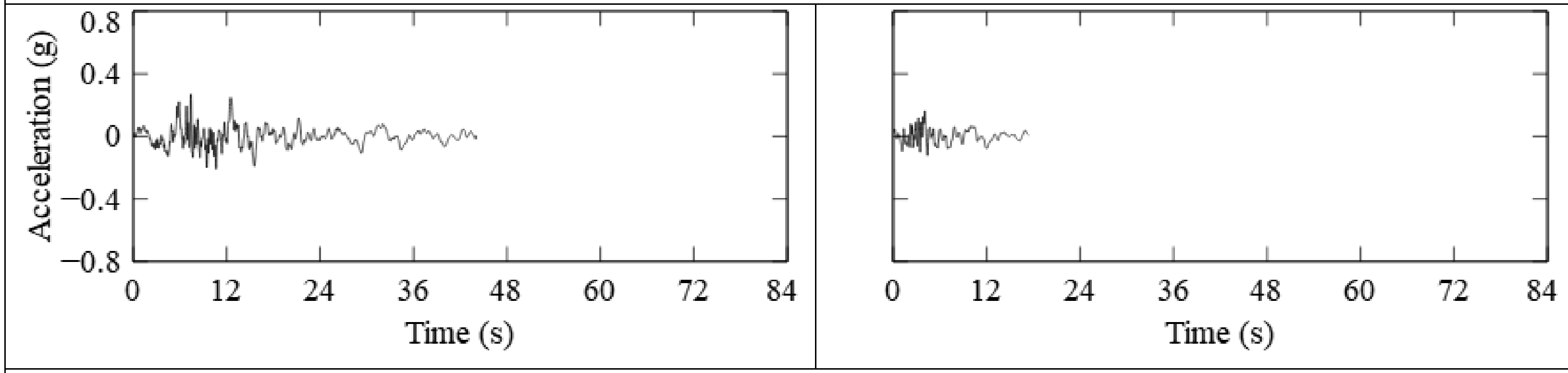

Fig. S87 Scaled Sequence Considered for Sl. No. 102 in Table A1

Main shock

Aftershock

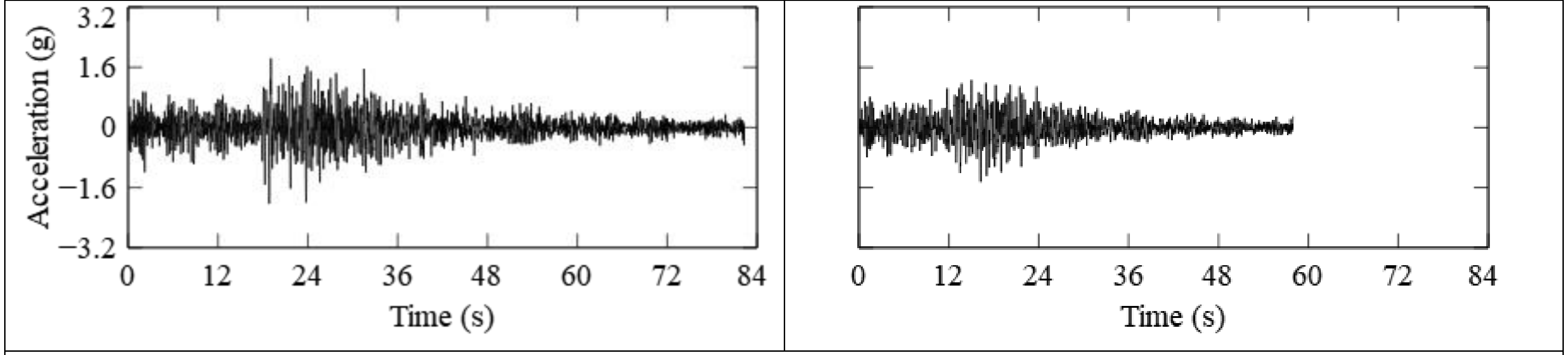

Fig. S88 Scaled Sequence Considered for Sl. No. 1 in Table A2

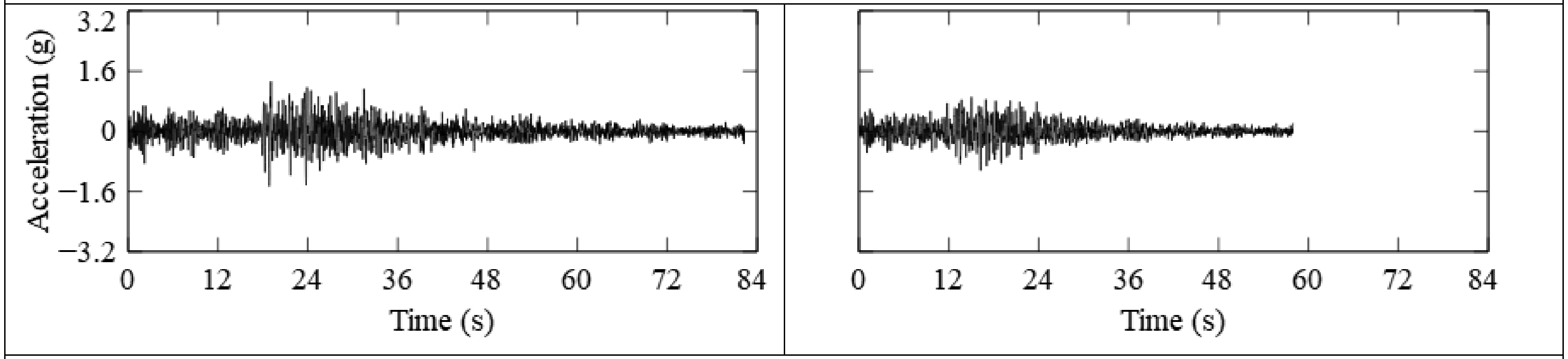

Fig. S89 Scaled Sequence Considered for Sl. No. 2 in Table A2

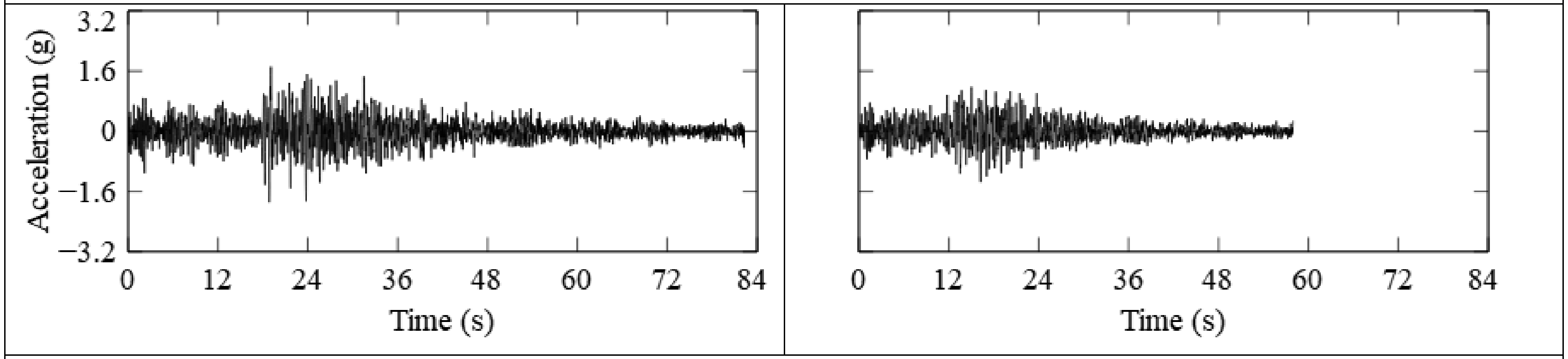

Fig. S90 Scaled Sequence Considered for Sl. No. 3 in Table A2

Main shock

Aftershock

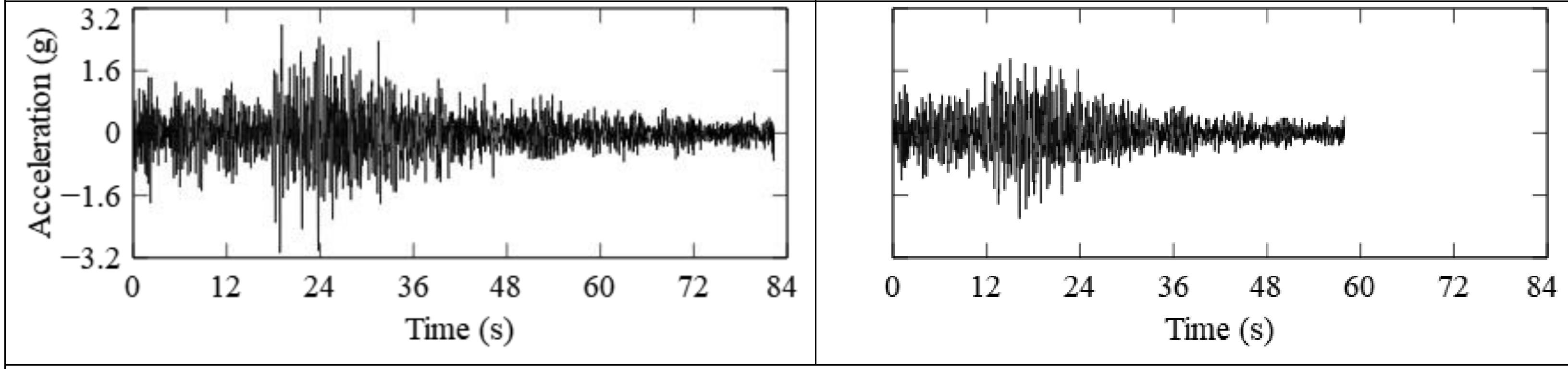

Fig. S91 Scaled Sequence Considered for Sl. No. 7 in Table A2

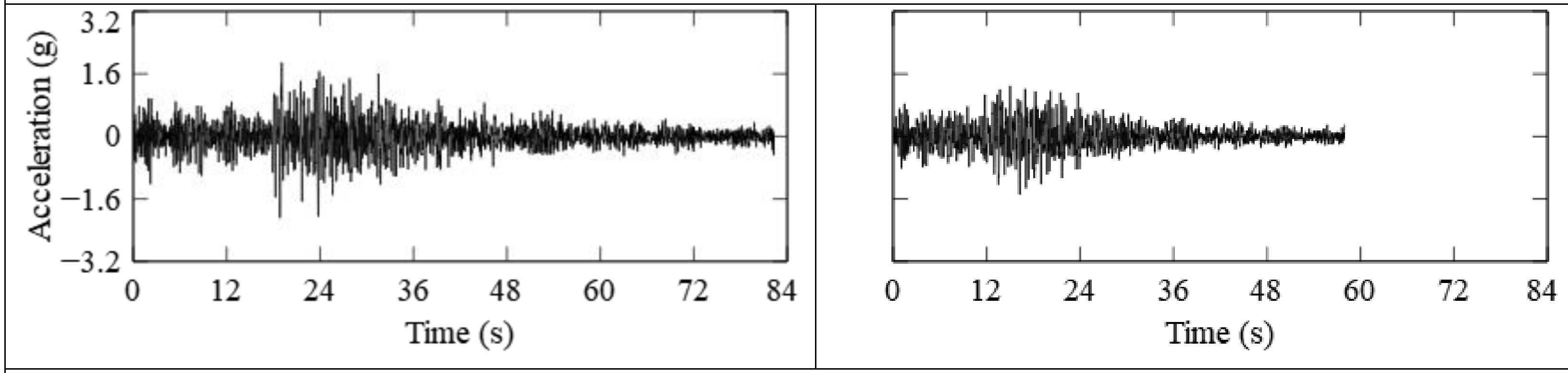

Fig. S92 Scaled Sequence Considered for Sl. No. 8 in Table A2

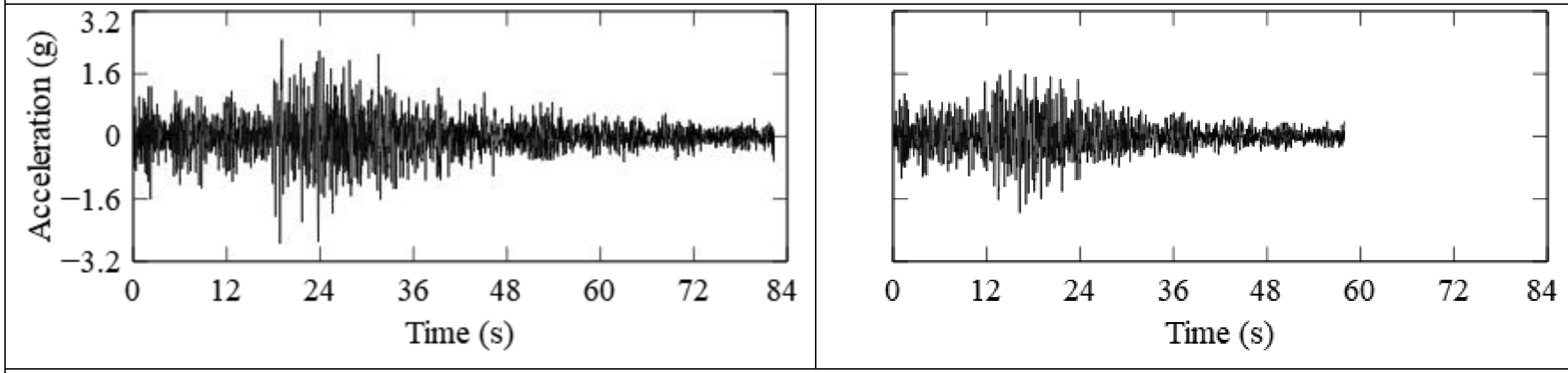

Fig. S93 Scaled Sequence Considered for Sl. No. 9 in Table A2

Main shock	Aftershock 1 and 2	Aftershock 3

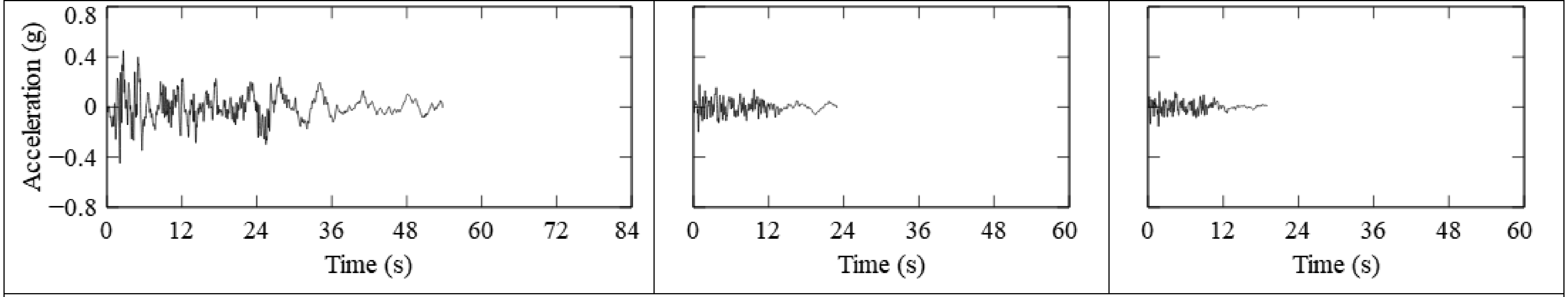

Fig. S94 Scaled Sequence Considered for Sl. No. 1 in Table A3

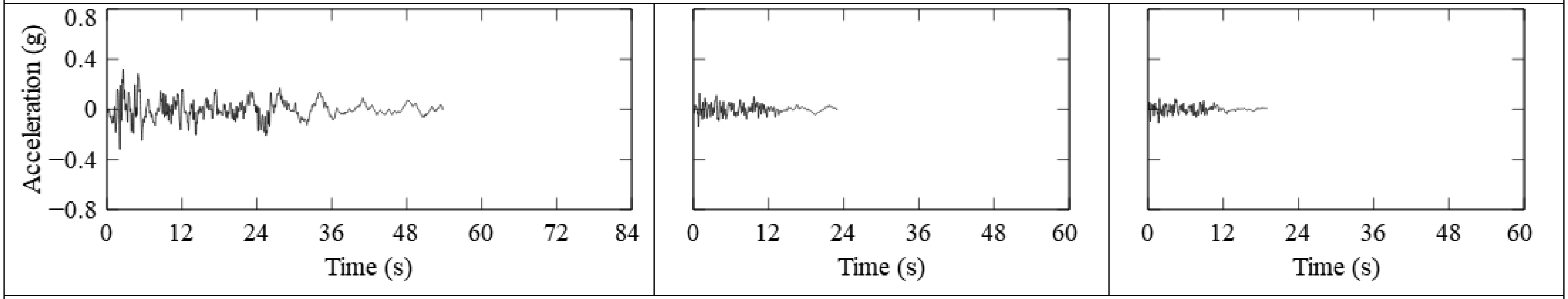

Fig. S95 Scaled Sequence Considered for Sl. No. 2 in Table A3

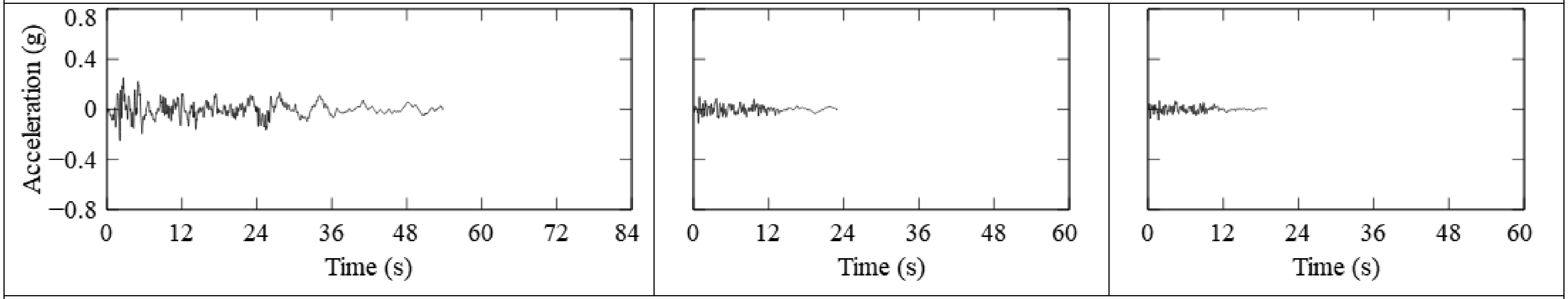

Fig. S96 Scaled Sequence Considered for Sl. No. 3 in Table A3

Main shock	Aftershock 1 and 2	Aftershock 3

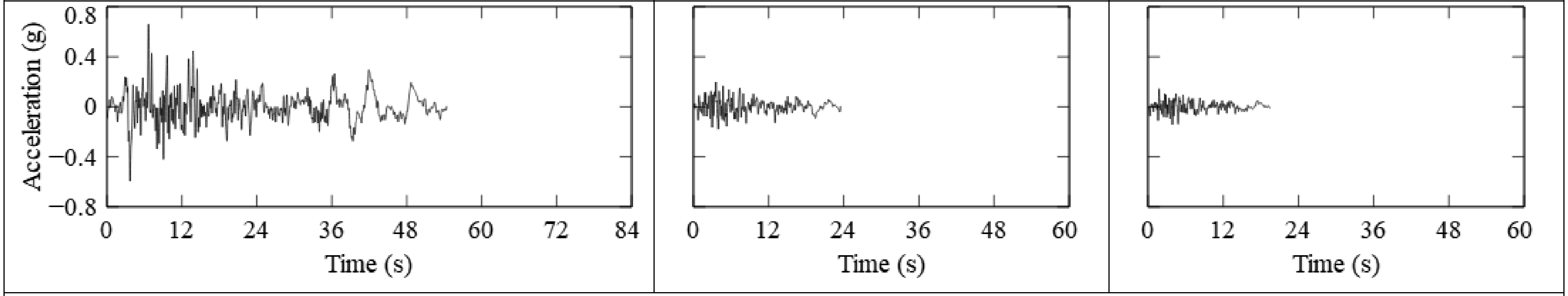

Fig. S97 Scaled Sequence Considered for Sl. No. 4 in Table A3

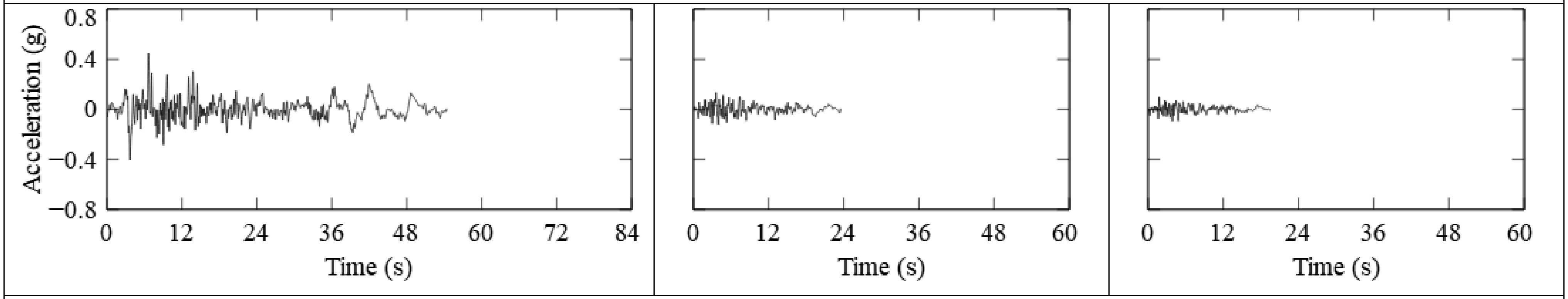

Fig. S98 Scaled Sequence Considered for Sl. No. 5 in Table A3

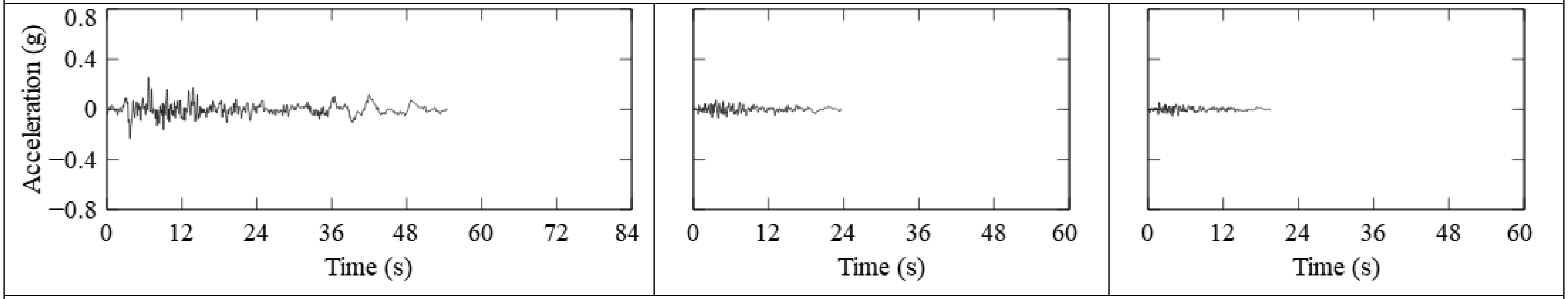

Fig. S99 Scaled Sequence Considered for Sl. No. 6 in Table A3

Main shock

Aftershock 1 and 2

Aftershock 3

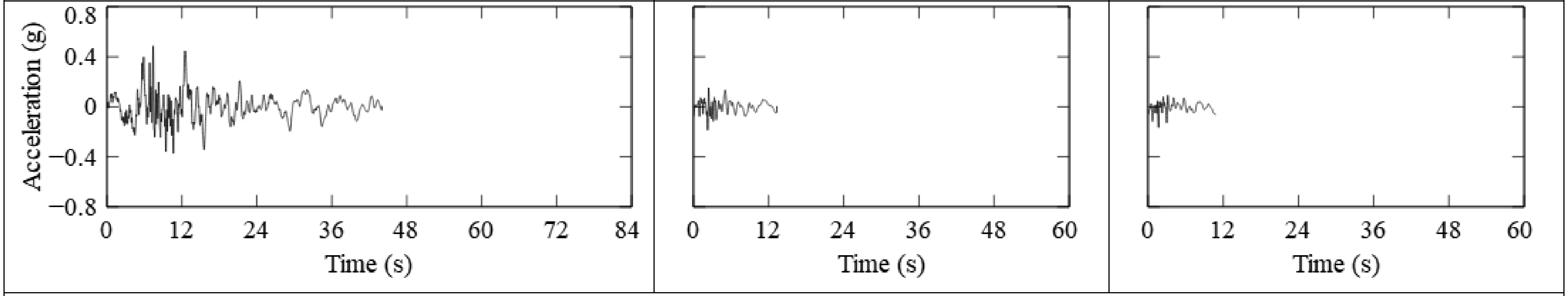

Fig. S100 Scaled Sequence Considered for Sl. No. 7 in Table A3

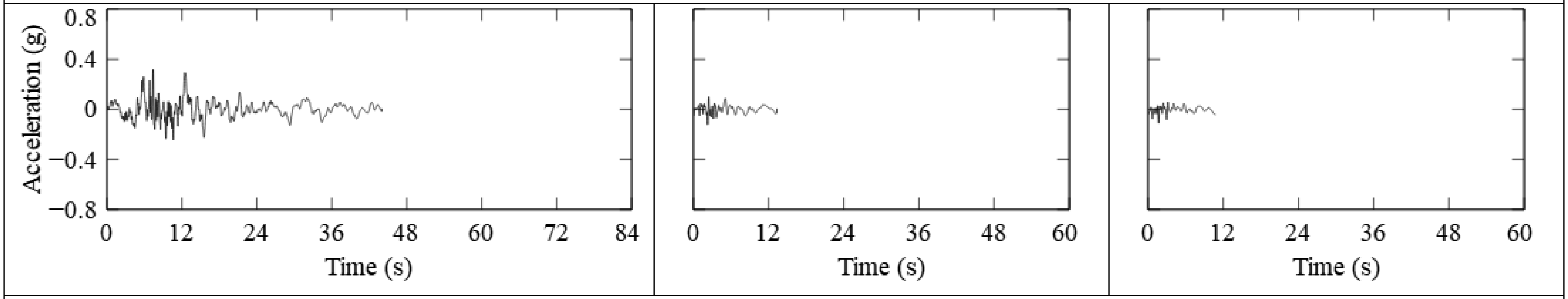

Fig. S101 Scaled Sequence Considered for Sl. No. 8 in Table A3

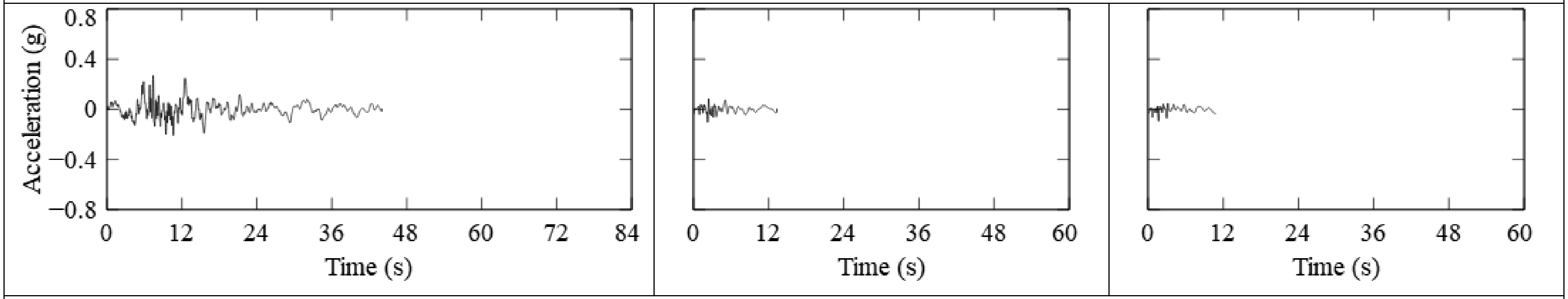

Fig. S102 Scaled Sequence Considered for Sl. No. 9 in Table A3

Main shock | Aftershock 1 and 2 | Aftershock 3

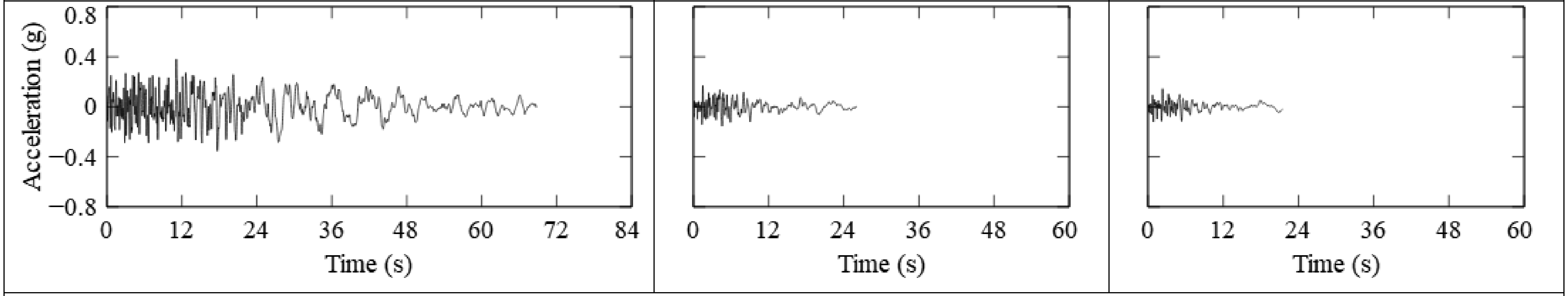

Fig. S103 Scaled Sequence Considered for Sl. No. 10 in Table A3

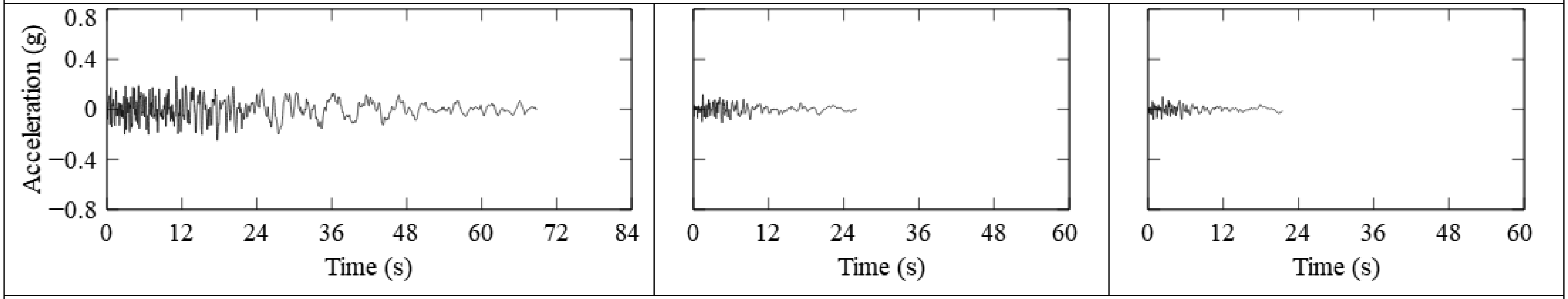

Fig. S104 Scaled Sequence Considered for Sl. No. 11 in Table A3

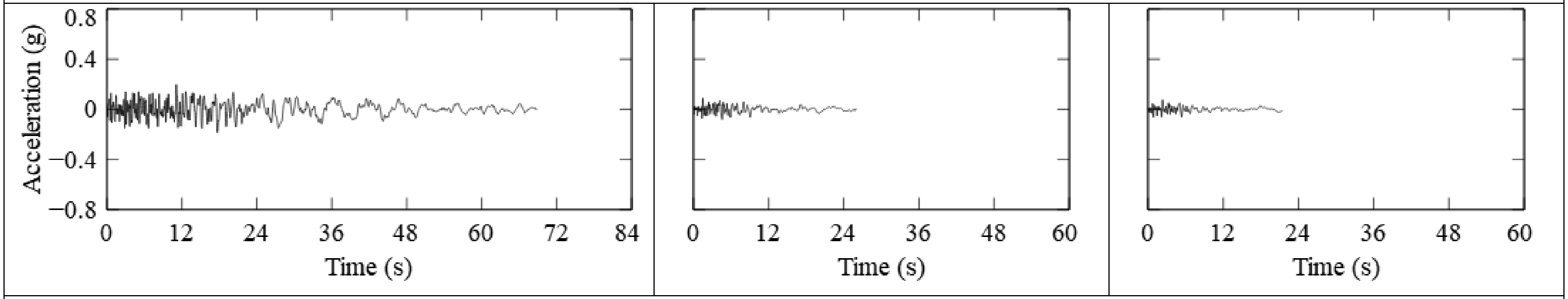

Fig. S105 Scaled Sequence Considered for Sl. No. 12 in Table A3

Main shock | Aftershock 1 and 2 | Aftershock 3

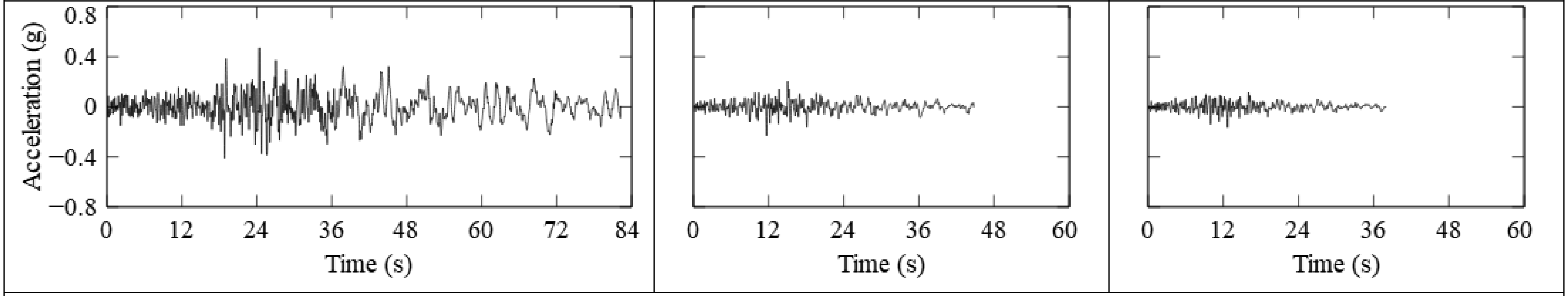

Fig. S106 Scaled Sequences Considered for Sl. Nos. 13 and 25 in Table A3

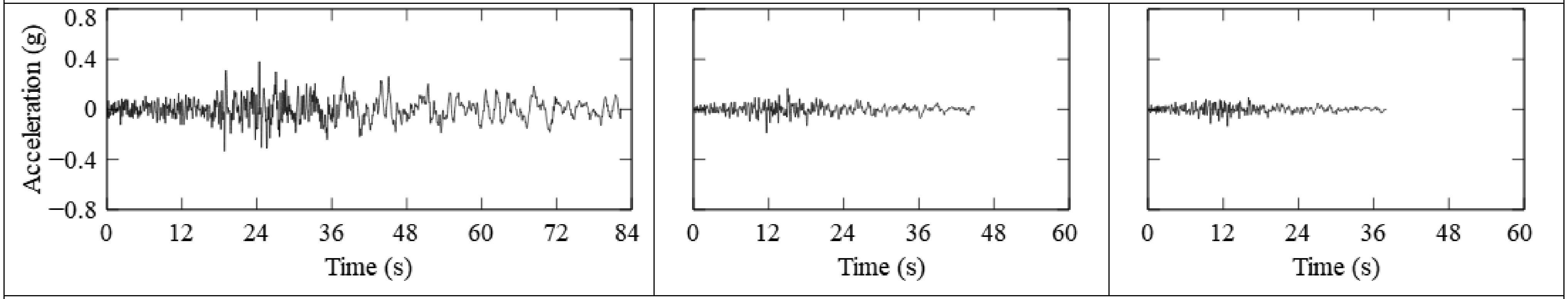

Fig. S107 Scaled Sequences Considered for Sl. Nos. 14 and 26 in Table A3

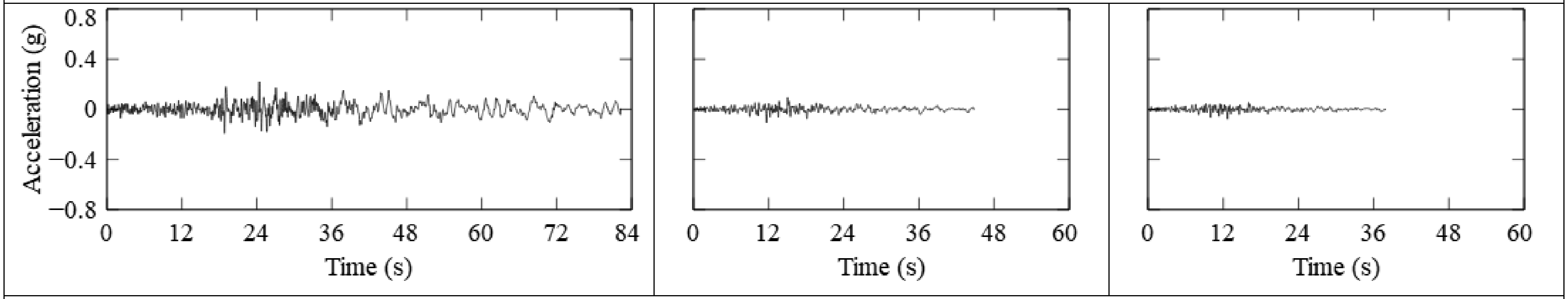

Fig. S108 Scaled Sequences Considered for Sl. Nos. 15 and 27 in Table A3

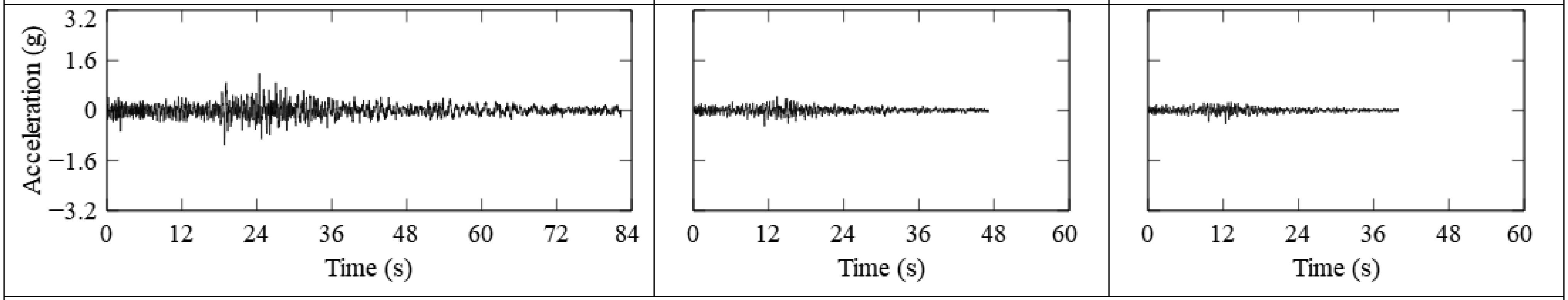

Fig. S109 Scaled Sequence Considered for Sl. No. 16 in Table A3

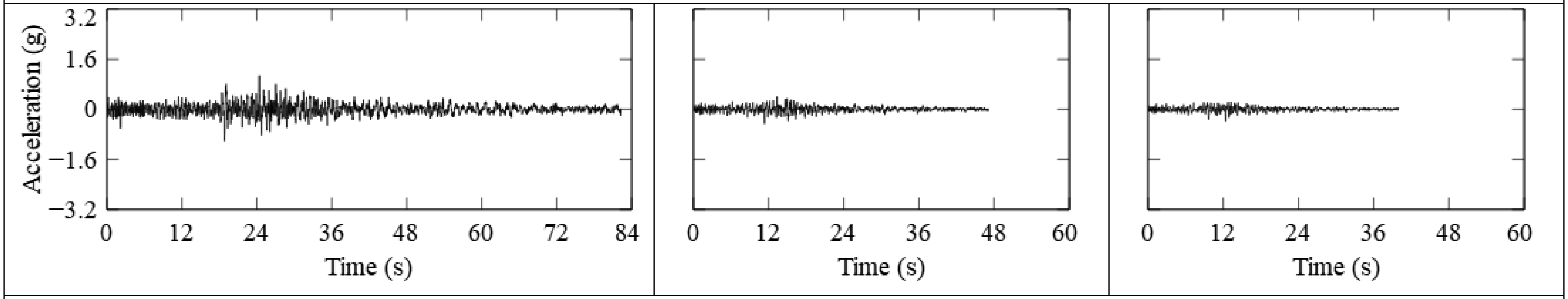

Fig. S110 Scaled Sequence Considered for Sl. No. 17 in Table A3

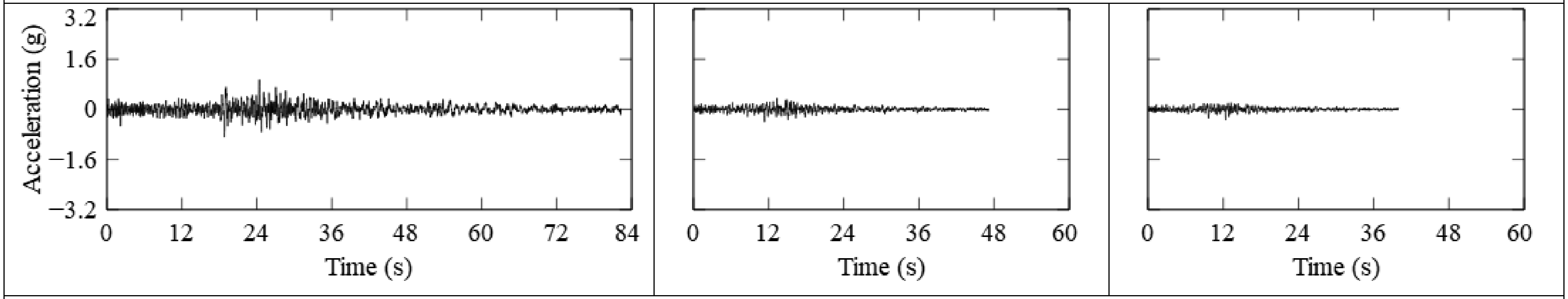

Fig. S111 Scaled Sequence Considered for Sl. No. 18 in Table A3

Main shock | Aftershock 1 and 2 | Aftershock 3

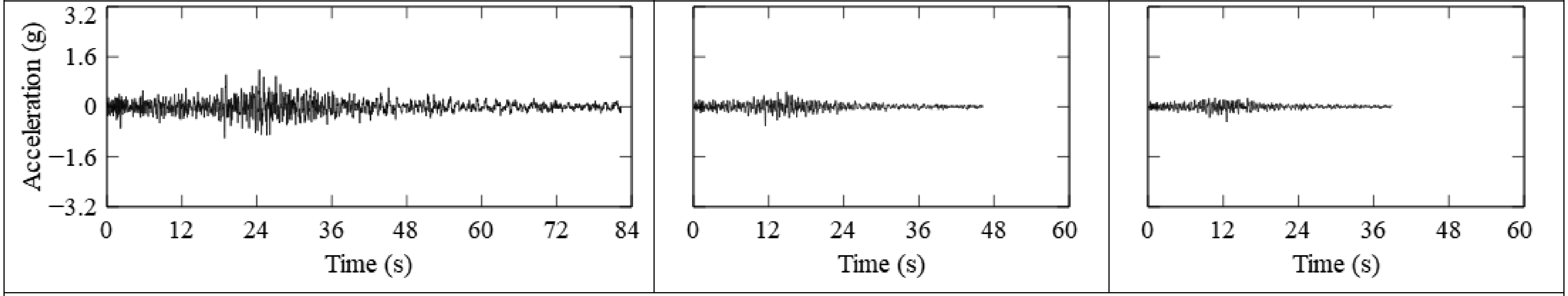

Fig. S112 Scaled Sequence Considered for Sl. No. 19 in Table A3

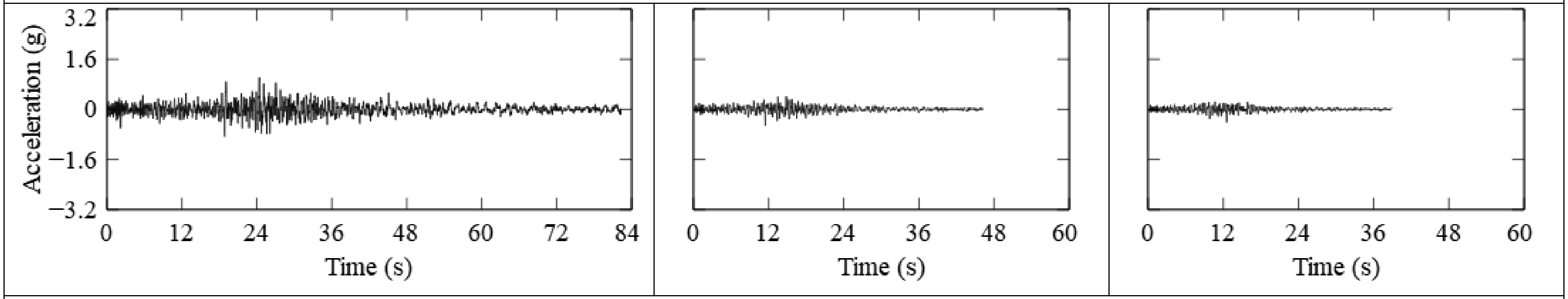

Fig. S113 Scaled Sequence Considered for Sl. No. 20 in Table A3

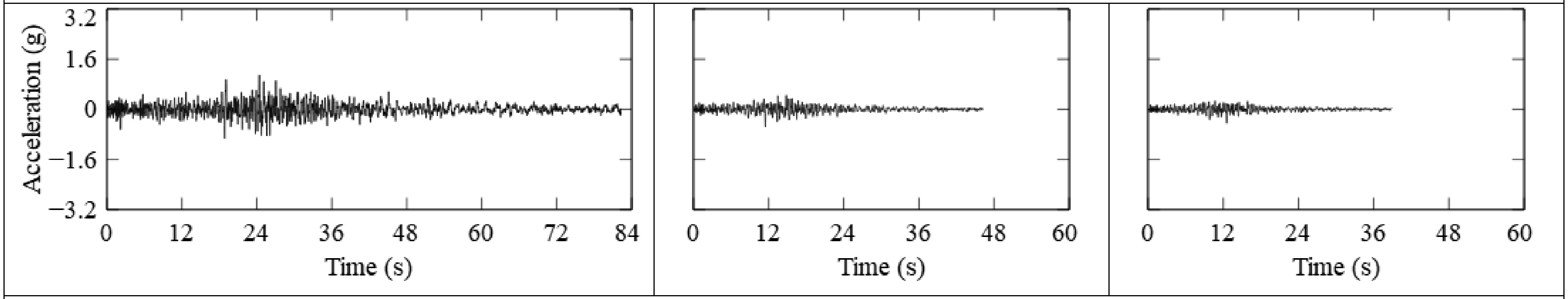

Fig. S114 Scaled Sequence Considered for Sl. No. 21 in Table A3

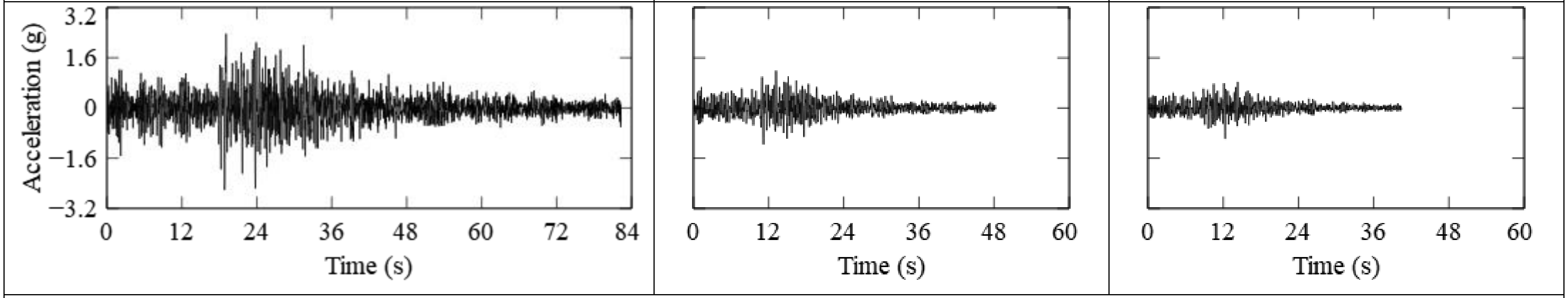

Fig. S115 Scaled Sequence Considered for Sl. No. 22 in Table A3

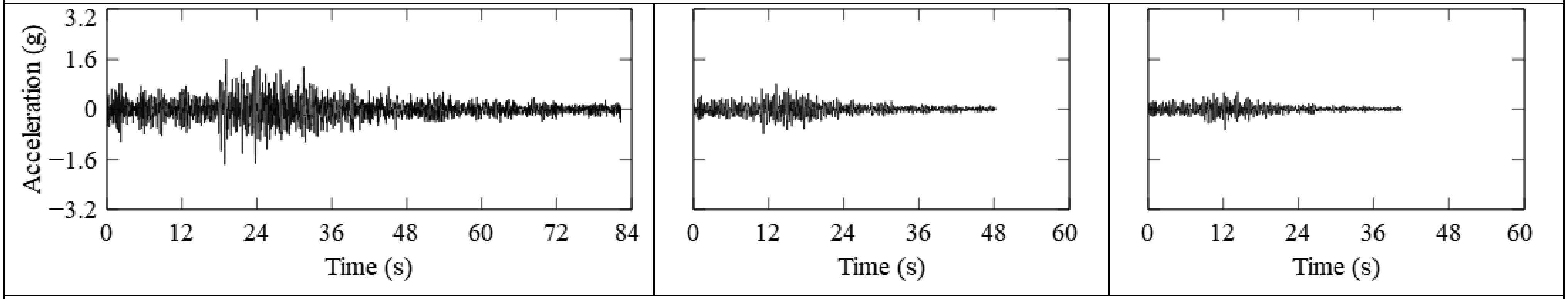

Fig. S116 Scaled Sequence Considered for Sl. No. 23 in Table A3

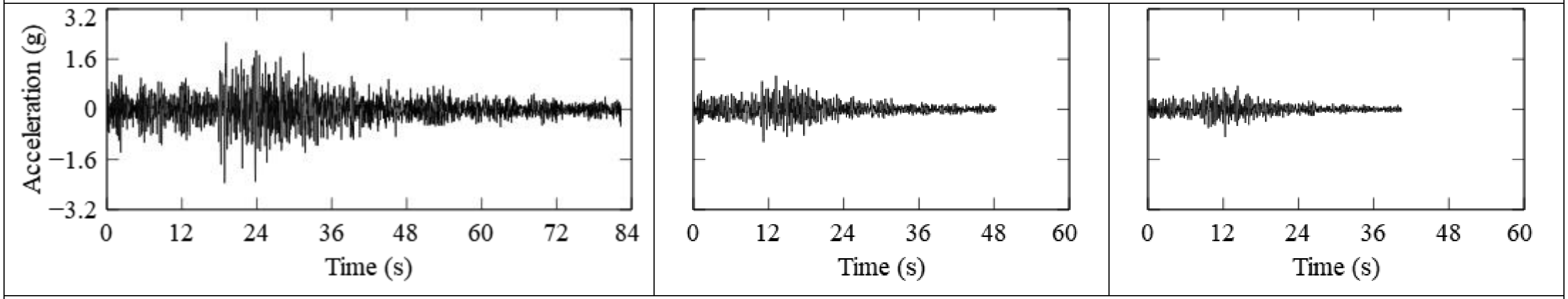

Fig. S117 Scaled Sequence Considered for Sl. No. 24 in Table A3

Main shock | Aftershock 1 and 2 | Aftershock 3

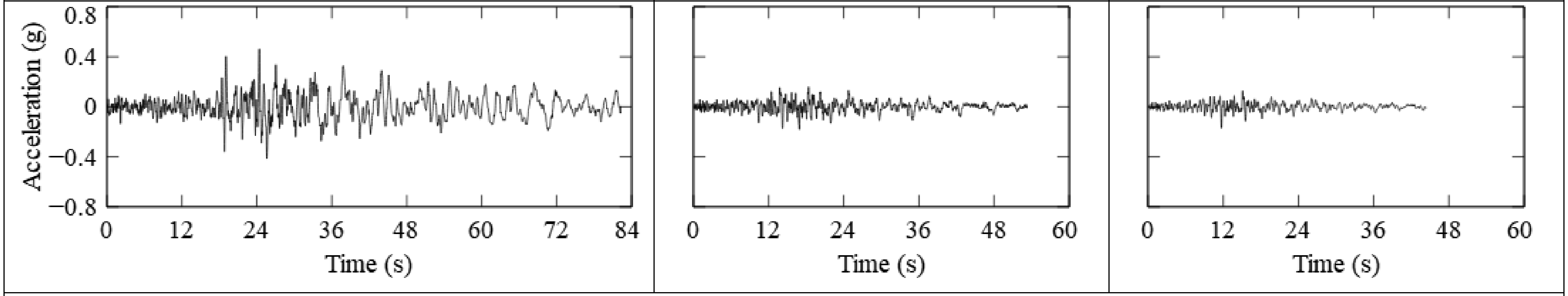

Fig. S118 Scaled Sequence Considered for Sl. No. 28 in Table A3

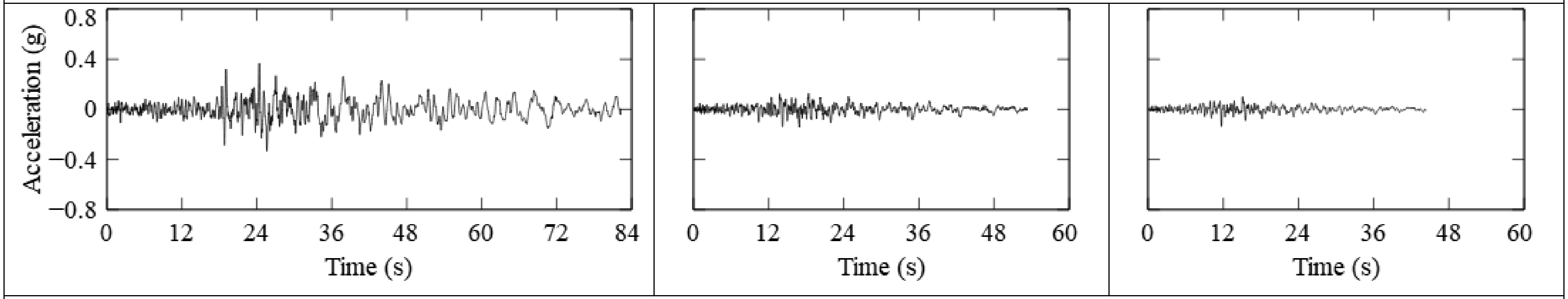

Fig. S119 Scaled Sequence Considered for Sl. No. 29 in Table A3

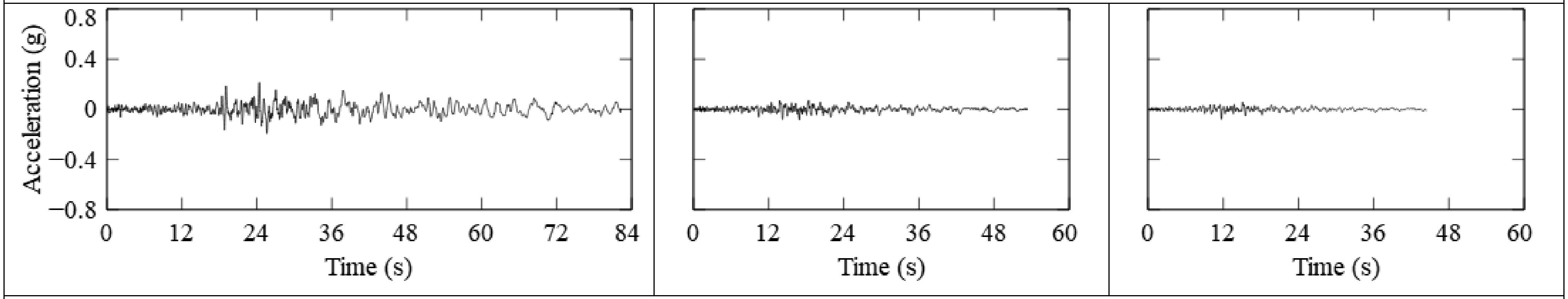

Fig. S120 Scaled Sequence Considered for Sl. No. 30 in Table A3